UNIVERSITY OF CATANIA
DIEEI, Faculty of Engineering

Gregorio Sciuto

HANDBOOK OF EXPERIMENTAL CHAOTIC CIRCUITS AND THEIR SYNCHRONIZATION

International Ph. D. course
in Electronics, Automation
and Complex Systems Engineering

Coordinator
Prof. Eng. Luigi Fortuna

Tutors
Prof. Eng. Luigi Fortuna
Prof. Eng. Mattia Frasca

INDEX

Abstract

Chaos is a remarkable phenomenon occurring in many nonlinear systems, where the deterministic nature of the system structure conjugates with the irregularity of the behviour.
Since the first findings on chaos in mathematical models, the idea of using electronic circuits as experimental testbeds for chaos aroses. The focus of this PhD thesis is indeed on an experimental approach to the study of chaos, to its characteristic features and to the synchronization properties mainly through chaotic circuit design implementation and experiments.
Starting from general guidelines on how to impl,ement from a mathematical model, an electronic circuit governed by the some equations, a gallery of circuits (Chua, Lorenz, Rössler, Hindmarsh-Rose, Duffing, Langford, Colpitts and a memristive circuit) designed and implemented with off-the-shelf components is presented in Chapter 1.
A general methodology for designing a new class of chaotic circuits based on time-delay is then discussed in Chapter 2. Chaos has unique properties even when two or more coupled chaotic systems are considered. The experimental approach to this topic of chaos theory pursued in this thesis led to several important results that otherwise had not been possible to reveal.
In fact, in Chapter 3 we discuss findings on the synchronization of chaotic circuits in the presence of either parametric or structural dissimetries, and present a very interesting observation of the circuits is minimized when the two circuits synchronously evolve.
Finally, Chapter 4 discusses a new form of synchronization occurring when more than two nonlinear circuits are coupled in networks with particular topologies.

Chapter 1
A GALLERY OF NONLINEAR CIRCUITS

1. Introduction

This thesis is the synthesis of the activities carried on during the three years of the Ph.D. course. Main subject of the thesis is the design, implementation and characterization of nonlinear circuits and of complex dynamical phenomena emerging from the coupling of two, or more, of them.
Before describing the results summarized in the following chapters, aim of this introductive chapter is to give the basic insights on the design techniques developed and adopted for the realization of all the experimental activities. Furthermore, in this chapter the design flow to obtain the circuital implementation of several nonlinear models is described.
As it will be clearly shown in the following sections, the design of the electrical analogue of a nonlinear model is based on the use of simple basic configurations, most of which essentially formed by operational amplifiers. In the next paragraph, such simple configurations will be outlined.

1.1. Operational Amplifier

The main building block for nonlinear circuits is the operational amplifier (OP-AMP). OP-AMPs are electronic devices important for a wide range of applications. They are characterized by two differential inputs V_+ and V_- and one output V_{out}. The circuital symbol used is shown in

Fig.1.1, in which the needed power supplies are indicated as V_{s+} and V_{s-}. The transfer characteristic of thre OPAM from input to the output is nonlinear and can be expressed as follows:

$$v_0 = f(v_d) = \begin{cases} -E_{sat} & IF \quad v_d \le -E_{sat} / A_v \\ A_v v_d & IF \quad |v_d| < E_{sat} / A_v \\ E_{sat} & IF \quad v_d \ge E_{sat} / A_v \end{cases} \qquad (1.1)$$

where is the voltage value at which the output of the operational amplifier saturates. It depends on the internal circuitry design of the device and on the voltage supply used.

The region in which is defined as the linear region.

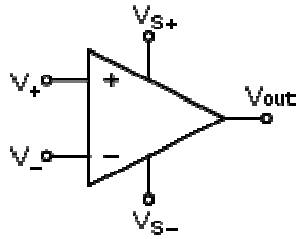

Fig.1.1 – Operational Amplifier

In the ideal case, the device has high input impedance, low output impedance and a high voltage gain A_v. As a consequence of the high input impedance, no current flows into or out of the input terminals.

An OP-AMP can be integrated in a single chip and used to implement several types of mathematical operations according to the specific configuration. The most used configurations are the follows:

1. Inverting
2. Non-inverting
3. Algebraic adder
4. RC integrator

1.2. Inverting configuration

In Fig.1.1 is shown the inverting configuration. An inverting amplifier uses negative feedback to invert (i.e., negate) and amplify a voltage. The input v_{in} is related to the output v_{out} through the following equation:

$$v_{out} = -\frac{R_2}{R_1} v_{in} \tag{1.2}$$

where the gain is fixed by the ratio between R_2 and R_1.

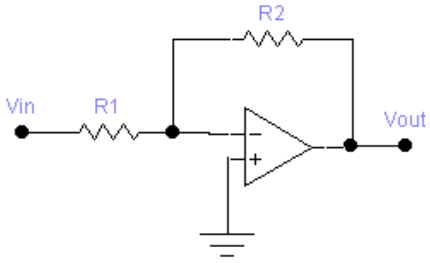

Fig.1.2 Inverting configuration.

This relationship can be derived by taking into account that the current i flowing into the resistor R_1 is given by:

$$i = \frac{v_{in} + v_d}{R_1} \tag{1.3}$$

Since no current flows in the negative input terminal, the current in R_2 is the same in R_1, and thus:

$$v_{out} = -R_2 i + v_d \tag{1.4}$$

It is possible to derive that:

$$v_{out} = -\frac{R_2}{R_1} v_{in} - \left(\frac{R_2}{R_1} + 1 \right) v_d \tag{1.5}$$

and considering that usually the device works in the linear region:

$$\frac{v_{out}}{v_{in}} = -\frac{\frac{R_2}{R_1} A_v}{A_v + \left(\frac{R_2}{R_1} + 1 \right)} \tag{1.5}$$

In the limit of large gain, $A_v \to \infty$, the relationship introduced at the beginning of this paragraph is obtained. An inverting adder is shown in Fig.1.2 in the limit of large gain the output is given by:

$$v_{out} = -\frac{R_2}{R_1} v_1 - \frac{R_2}{R_3} v_2 \tag{1.6}$$

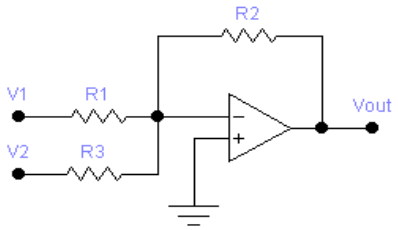

Fig.1.3 Inverting adder.

1.3. Non-inverting configuration

In Fig.1.3 the non-inverting configuration is shown. A non-inverting amplifier amplifies a voltage and it can be demonstrated that the output v_{out} is given by:

$$v_{out} = \left(\frac{R_2}{R_1} + 1 \right) v_{in} \tag{1.7}$$

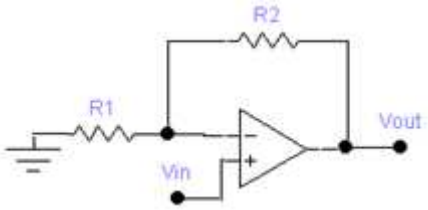

Fig.1.4 Non-Inverting configuration.

1.4. Algebraic adder configuration

If the mathematical operation to be implemented is an algebraic sum, the corresponding circuital configuration is the algebraic adder, reported in Fig 1.5

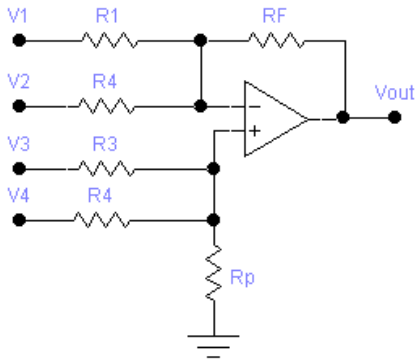

Fig.1.5 Algebaic adder.

The scheme of Fig.1.5 implements the following mathematical operation as in (1.8):

$$v_{out} = -\frac{R_F}{R_1} v_1 - \frac{R_F}{R_4} v_2 + \frac{R_F}{R_3} v_3 - \frac{R_F}{R_4} v_4 \tag{1.8}$$

To adopt this configuration it is important that the compensation resistance *Rp* is calculated to satisfies the *gain rule* as in (1.9):

$$R_p : \frac{1}{R_3} + \frac{1}{R_4} + \frac{1}{R_p} = \frac{1}{R_1} + \frac{1}{R_2} + \frac{1}{R_F} \tag{1.9}$$

then the output of the circuit is given by the following equation in:

$$v_{out} = \sum_i A_i v_i \tag{1.10}$$

with $A_i = R_f / R_i$.
The output depends on each single input by means of only the associated input resistor and not of the other resistors, which is very convenient from the designer perspective. We notice that, when satisfying the gain rule results in a negative value of R_p, R_f should be changed to avoid this.

1.5. RC integrator

Another important mathematical operation is integrator configuration that exploits the properties of the operational amplifier in the linear region. The configuration is shown in Fig.1.6.

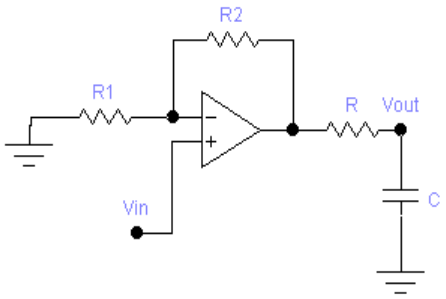

Fig.1.6 RC integrator.

In the limit of large voltage gain A_v, it can be assumed that the current flowing in the resistor R is $i = v_{in}/R$ and is equal to that in the capacitor.

$$CR\dot{v}_{out} = -v_{out} + Av_{in} \tag{1.11}$$

In the RC integrator the current flowing into the resistor R is:

$$i = \frac{v_0 - v}{R} \tag{1.12}$$

On the other hand, taking into account the relationship between current and voltage across a capacitor, since $i = C\frac{dv}{dt}$ one has:

$$\frac{dv}{dt} = \frac{v_0 - v}{CR} \tag{1.13}$$

and thus

$$CR\dot{v} = -v + v_0 \tag{1.14}$$

The relationship expressed by Eq. (2.4) will be used to design operational amplifier that implement base blocks of a first order generic differential equation of the type:

$$\dot{x} = -x + f(x,t) \tag{1.15}$$

1.6. The analog multiplier AD633

Chaotic circuits have polynomial nonlinearities or products of state variables. Electronic realization of the operation of multiplication is realized with AD633 analog component. This low cost multiplier has a functional block diagram as in Fig 1.7.

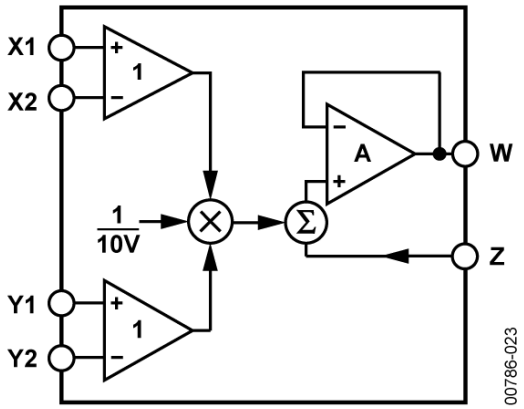

Fig.1.7 AD633 functional block diagram.

The transfer function of AD633 is the following:

$$W = \frac{(X1 - X2)(Y1 - Y2)}{10V} + Z \tag{1.16}$$

1.7. The operational amplifier TL084

Operational amplifiers used in the design of nonlinear circuits are of two models TL084 and TL082. They have respectively the two functional block diagrams as in Fig 1.8 and Fig 1.9.

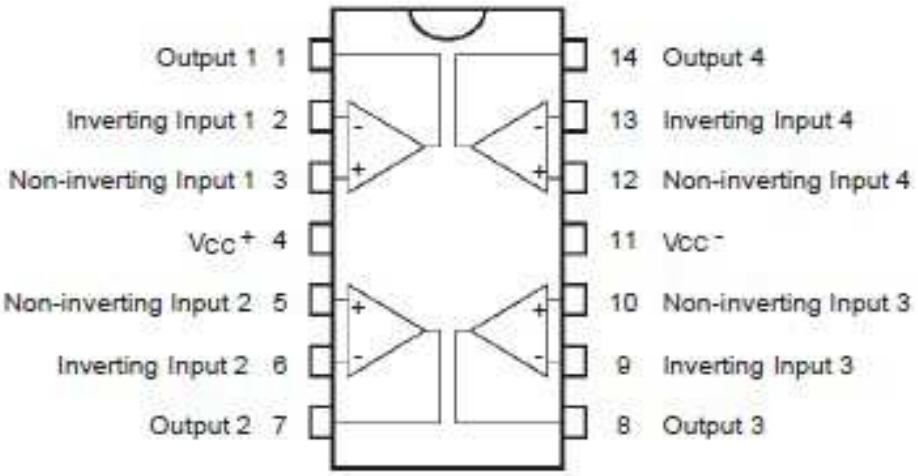

Fig.1.8 TL084 functional block diagram.

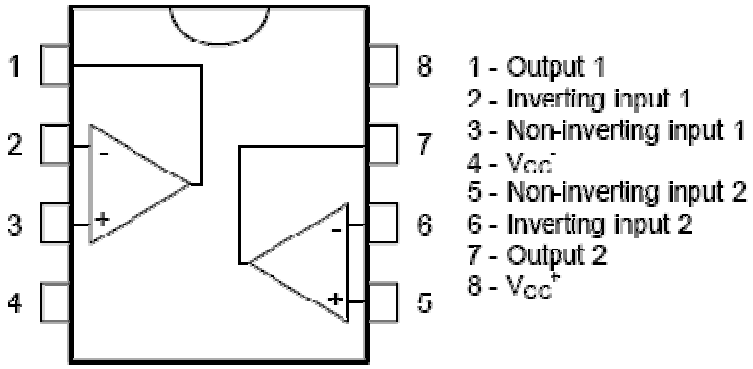

Fig.1.9 TL082 functional block diagram.

1.8. Implementing nonlinear circuits

A possible strategy for the design of nonlinear electronic circuits relies on the concept of Cellular Neural/Nonlinear Networks (CNNs). CNNs were introduced by L. O. Chua [Chua and Yang (1988b,a)] in 1988. His idea was to use an array of simple, identical, locally interconnected nonlinear dynamical circuits, called cells, to build large scale analog signal processing systems.
The cell was defined as the nonlinear first order circuit shown in Fig. 1.10 (a), u_{ij} , y_{ij} and x_{ij} being the input, the output and the state variable of the cell, respectively. The output is related to the state by the nonlinear equation:

$$y_{ij} = 0.5(|x_{ij} + 1| - |x_{ij} - 1| \qquad (1.17)$$

A CNN is defined as a two-dimensional array of MxN identical cells arranged in a rectangular grid, as depicted in Fig. 1.10 (b).

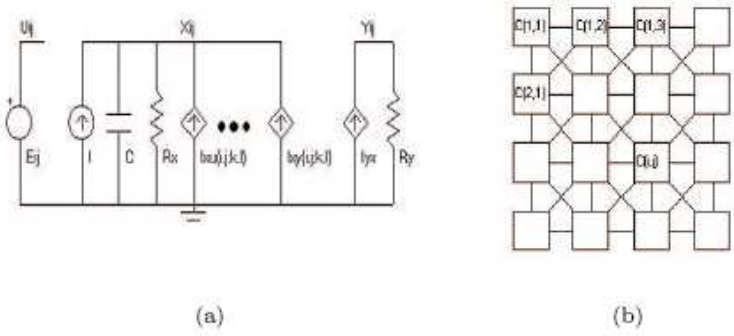

(a) (b)

Fig.1.10 – (a) Chua-Yang CNN cell, (b) schematic representation of a CNN (b)

Each cell mutually interacts with its nearest neighbors by means of the voltage controlled current sources $I_{xy}(i,j;\,k,l) = A(i,j;k,l)y_{kl}$ and $I_{xu}(i,j;\,k,l) = B(i,j;k,l)u_{kl}$ The constant coefficients $A(i,j;k,l)$ and $B(i,j;k,l)$ are known as the feedback and input cloning templates, respectively. If they are equal for each cell, they are called space-invariant. If $B(i,j;k,l) = 0$ the CNN is said autonomous.
A CNN is described by the state equations of all cells:

$$C\frac{dx_{ij}}{dt} = -\frac{x_{ij}}{R_x} + \sum_{C(k,l)\in N_r(i,j)}[A(i,j;k,l)y_{kl} + B(i,j;k,l)u_{kl}] + I \qquad (1.18)$$

where i=1,2,…,M and j=1,2,…,N and

$$N_r(i,j) = \{C(k,l) \mid \max(|k-i|,|l-j|) \le r\} \qquad (1.19)$$

with k=1,2,…,M and l=1,2,…,N is the r-neighborhood.
This model is known as the Chua-Yang model or linear CNN and refers to a single-layer CNN. This model can be extended to a multilayer CNN if each cell has more than one state variable.
The CNN behavior is basically dictated by the templates [Chua (1998); Chua and Roska (2005); Manganaro et al. (1999)]. However, the choice of templates that are suitable to achieve a desired processing task is hard to accomplish in a direct way.
This leads to the so-called learning and design problem [Nossek (1994); Nossek et al. (1993)]. The term design is used when the desired task can be translated into a set of local dynamic rules, while the term learning is used when the templates need to be obtained by learning techniques, so pairs of inputs and outputs must correspond. Some good results have been obtained with discrete-time CNNs in simple cases, but this is a really difficult problem for continuous-time models. Most of the templates currently available have been obtained by intuitive principles and refined by trial and error with the aid of simulators.
Many different spatial-temporal phenomena can be studied by using CNNs [Chua and Roska (2005); Manganaro et al. (1999)]. In fact, complex phenomena such as pattern generation, wave propagation, birth of spiral waves, visual processing can be investigated and reproduced with applications in different disciplines, many of them are today possible thanks to the recently developed VLSI realizations [Fortuna et al. (2001a)]. The emulation of these different phenomena is obtained by suitably programming the templates of the CNN, which makes it an universal paradigm for the study and the emulation of nonlinear complex dynamics.
The Chua-Yang model has been generalized in many different ways. These generalizations allow the inclusion in the model (1.18) of nonlinear interactions, direct dependence on the state variables of the neighborhood cells, different grids, and lead to a more general definition for CNNs [Chua and Roska (1993)].

As discussed above, in the standard CNN model the state variable of each cell directly depends on the outputs and inputs of the neighbouring cells. A possible generalization of the CNN model is the so-called State Controlled CNN (SC-CNN), in which the direct dependance on the state variable is introduced. Since, in the following, only mono-dimensional arrays will be used, the definition reported below is restricted to this case. In accordance with the CNN symbolism, the SC-CNN is defined as follows: a SC-CNN is an array of nonlinear circuits C(j) with the following state equation:

$$\frac{dx_j}{dt} = -x_j + \sum_{C(k)\in N(j)}\{A_{j;k}y_k + B_{j;k}u_k + C_{j;k}x_k\} + I \qquad (1.20)$$

$$y_j = f(x_j)$$

$$1 \le j \le N$$

where:

$$f(x) = 0.5(|x+1| - |x-1|) \qquad (1.21)$$

where x_j , y_j , u_j are the state variable, the output and the input of the cell C(j), respectively, N is the number of cells, N(j) is the neighbour set of the cell C(j), f is the output nonlinearity function and I is the bias. Furthermore, together with the classical A and B templates, a new template, named state template, is introduced.
Since each cell is a first-order system, a SC-CNN made of N cells is a N-order dynamical system. By choosing the templates of the SC-CNN, i.e., the connections between the cells, different dynamical systems may be reproduced.
In the next Chapter it will be shown how a SC-CNN made of n cells (which is, thus, a n-order system) may be used to implement a mathematical model.

1.9. A gallery of nonlinear circuits: preliminaries

The design of a nonlinear circuit follows three successive phases: the first consists in the simulation of the original mathematical model which we want to implement as a circuit; in the second phase, the circuit is designed and simulated according to the observation made during the model analysis; finally, the circuit is physically implemented and experimentally characterized.

Any mathematical model, which is the basis of a dynamical system, has a number of state variables that follow precise temporal trends. These trends are contained in a range which depends on the model.
In order to implement the model in hardware using circuital components (resistors, capacitors, operational amplifiers, etc.), it is important that the oscillations of state variables are confined within the limit imposed by the voltage supplies powering operational amplifiers. To establish the specific power supply voltage, it is necessary to examine the model using simulation tools, in order to overcome possible errors of feasibility.
The first simulation tool, which is based on the numerical integration of the mathematical model, is Matlab. In this first phase, the oscillations range and the operating frequencies are characterized. On the basis of these observations the power supply voltage is chosen. However, if the state variables oscillate outside physically realizable voltage limits, the system can be suitably scaled in amplitude through a mathematical transformation.
The range of operating frequencies of each state variable is an important parameter of the system for both the feasibility of the system and the ability to simultaneously acquire the trend of the state variables of the circuit. The acquisition of waveforms generated by the circuits, in fact, is a necessary practice that is performed in order to analyze in more detail the individual behavior of all the state variables and compare them with the theoretical trends that have been obtained in the simulation using Matlab. The time variable of the dynamical system can also be rescaled, and this choice determines the values of capacitors used to reproduce system dynamics.
The second phase consists in the design of the circuit by suitably connecting simple blocks based on operational amplifiers. In this phase, a second simulation tool is used, i.e. Spice, with which the behavior of the designed electronic circuit can be simulated and adjusted.
The realization of the circuit with off-the-shelf electronic components leads to the conclusive phase, i.e. the experimentation and the observation of the dynamical behavior of the electronic analogue.

2. Chua's circuit

The dimensionless equations of Chua's circuit [103,104] consist of the following three state equations:

$$\begin{aligned} \dot{x} &= \alpha[y - h(x)] \\ \dot{y} &= x - y + z \\ \dot{z} &= -\beta y \end{aligned} \tag{1.24}$$

where $h(x) = m_1 x + \frac{1}{2}(m_0 - m_1)(|x+1| - |x-1|), m_1 = \frac{2}{7}, m_0 = -\frac{1}{7}$ and $\alpha = 9, \beta = 14.286$.

As shown in the simulation trend of Fig 1.11, obtained with Matlab, the behavior of x, y and z variable exhibits a typical feature of a chaotic system with irregular trends.

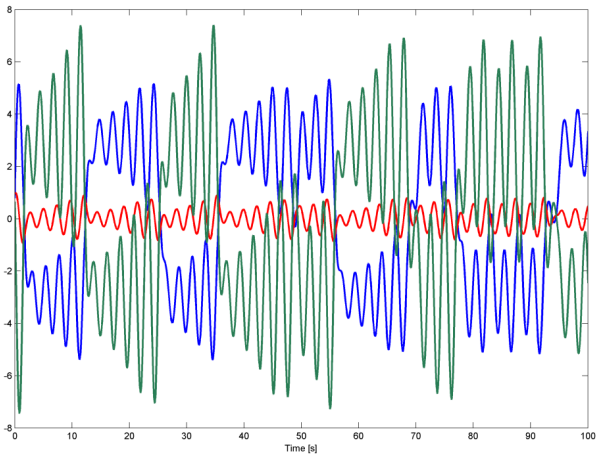

Fig.1.11 Theoretical temporal trend of each state variable x, y and z.

In Fig. 1.12, a typical chaotic attractor of the circuit, defined as "double–scroll", is shown. The graph is obtained using the following parameters:

$$m_1 = \frac{2}{7}, m_0 = -\frac{1}{7}, \alpha = 9, \beta = 14.286$$

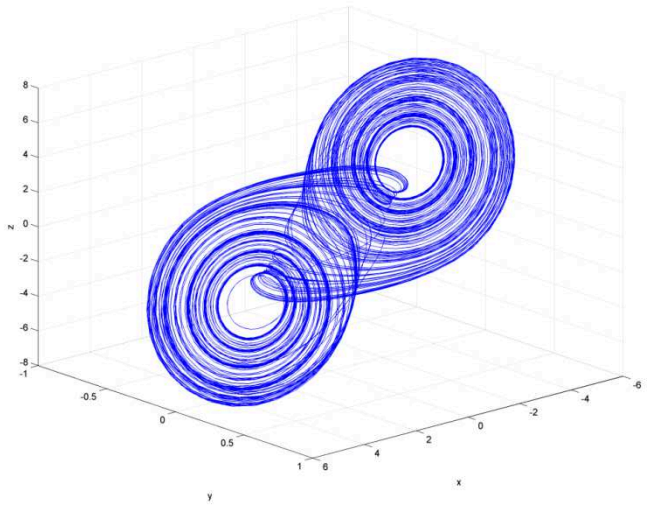

Fig.1.12 – 3D theoretical Chua's attractor.

Following the SC-CNN approach, in Fig. 1.13, an electronic circuit has been designed with Spice's tool and in Fig. 1.14 realized using resistors, capacitors and operational amplifiers.

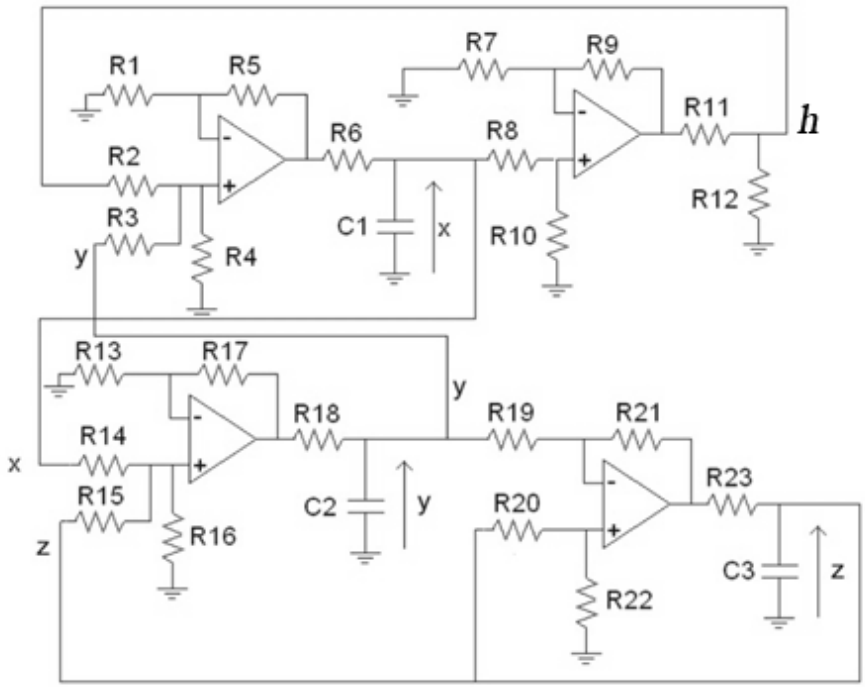

Fig.1.13 SC-CNN circuit diagram of Chua's model used in the experiment. Kit's components: R1 = 4kΩ, R2 = 13.3 kΩ, R3 = 5.6 kΩ, R4 = 20kΩ, R5 = 20kΩ, R6 = 380Ω (potentiometer), R7 = 112 kΩ, R8 = 112 kΩ, R9 = 1MΩ, R10 = 1MΩ, R11 = 12.1 kΩ, R12 = 1kΩ, R13 = 51.1 kΩ, R14 = 100 kΩ, R15 = 100 kΩ, R16 = 100 kΩ, R17 = 100 kΩ, R18 = 1kΩ, R19 = 8.2 kΩ, R20 = 100 kΩ, R21 = 100 kΩ, R22 = 7.8kΩ, R23 = 1kΩ, C1 = C2 = C3 = 100 nF, power supply = $\pm 9V$.

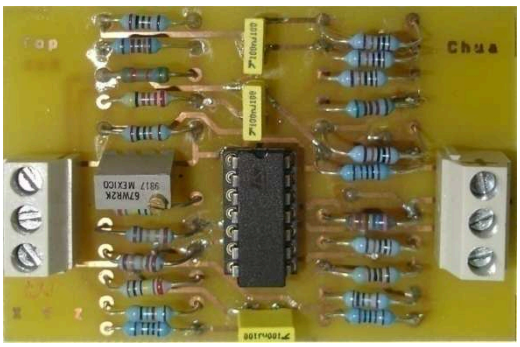

Fig.1.14 Hardware implementation of the Chua's circuit.

The circuital equations associated to the implementation of Chua's circuit are the following:

$$\begin{aligned} C_1 R_6 \dot{x} &= -x + \frac{R_5}{R_3} y + \frac{R_5}{R_2} h \\ C_2 R_{18} \dot{y} &= -y + \frac{R_{17}}{R_{14}} x + \frac{R_{17}}{R_{15}} z \\ C_3 R_{23} \dot{z} &= -z + \frac{R_{21}}{R_{20}} z + \frac{R_{21}}{R_{19}} y \end{aligned} \tag{1.25}$$

where

$$h = \frac{R_{12}}{R_{11} + R_{12}} \frac{R_9}{R_8} (|x+1| - |x-1|) \tag{1.26}$$

Matching equations (1.25) with the mathematical model in equations (1.24), it is possible to choose the values. The different behavior shown by the Chua's circuit by varying the single bifurcation parameter α can be observed in the circuit by varing resistor R6. In Fig.1.15 a typical chaotic behavior of the experimental circuit is shown.

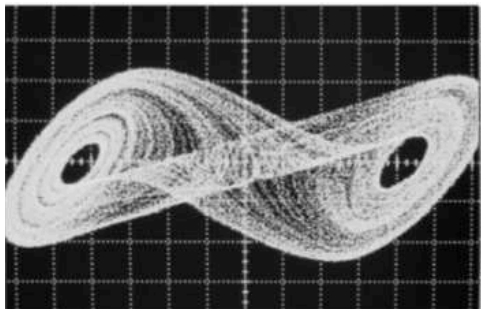

Fig.1.15 Experimental attractor of Chua's circuit. Phase plane: x |y, horizontal axis: 500mV=div, vertical axis 200mV=div.

3. The Lorenz circuit

The dimensionless equations of the Lorenz system [102] are:

$$\begin{aligned} \dot{x} &= \alpha(y - x) \\ \dot{y} &= \rho x - xz - y \\ \dot{z} &= xy - \beta z \end{aligned} \tag{1.27}$$

where $\alpha = 10, \rho = 28, \beta = \frac{8}{3}$

As shown in the simulation trend of Fig.1.16, obtained with Matlab tool, the behavior of x, y and z variable exhibit a typical feature of a chaotic system.

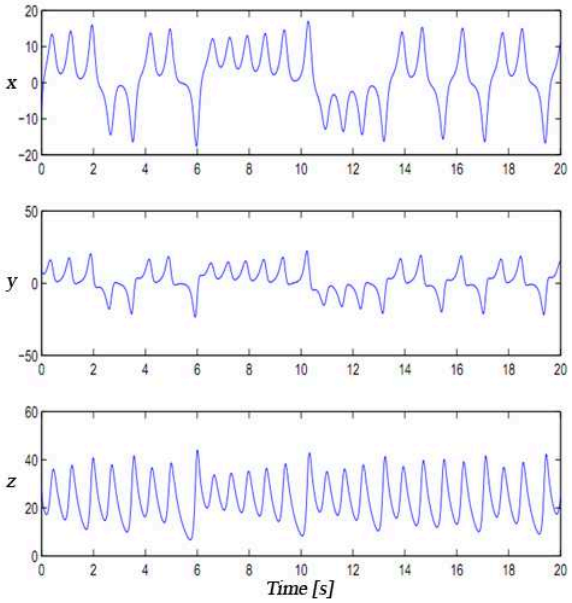

Fig.1.16 – Theoretical trend of x, y, and z variables.

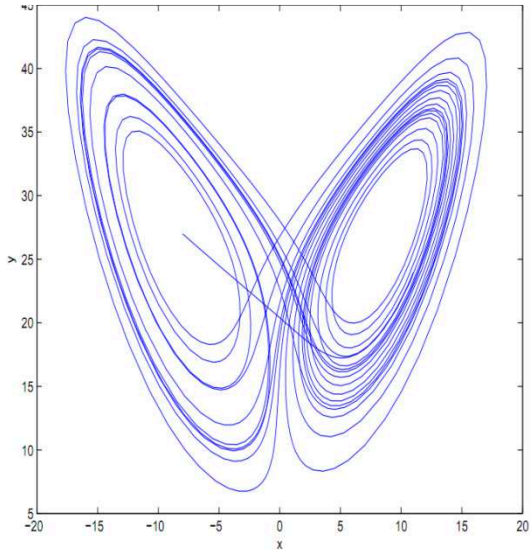

Fig.1.17– Theoretical Lorenz's attractor.

Choosing the power supply of operational amplifiers to be ± 9V, it is possible to notice that the amplitude of the state variables has a value above the 9V. In this regard it is necessary to apply a transformation to reduce any single variable. In particular, for the state variable x, y and z the transformations are the following:

$$\begin{aligned} x_{new} &= \frac{x_{old}}{10} \\ y_{new} &= \frac{y_{old}}{10} \\ z_{new} &= \frac{z_{old}}{100} \end{aligned} \tag{1.28}$$

the new rescaled system is shown in (1.29).

$$\begin{aligned} \dot{x} &= \alpha(y - x) \\ \dot{y} &= \rho x - 10xz - y \\ \dot{z} &= xy - \frac{\beta z}{10} \end{aligned} \tag{1.29}$$

So the system can be realized using resistors, capacitors and operational amplifiers as shown in Fig.1.18.

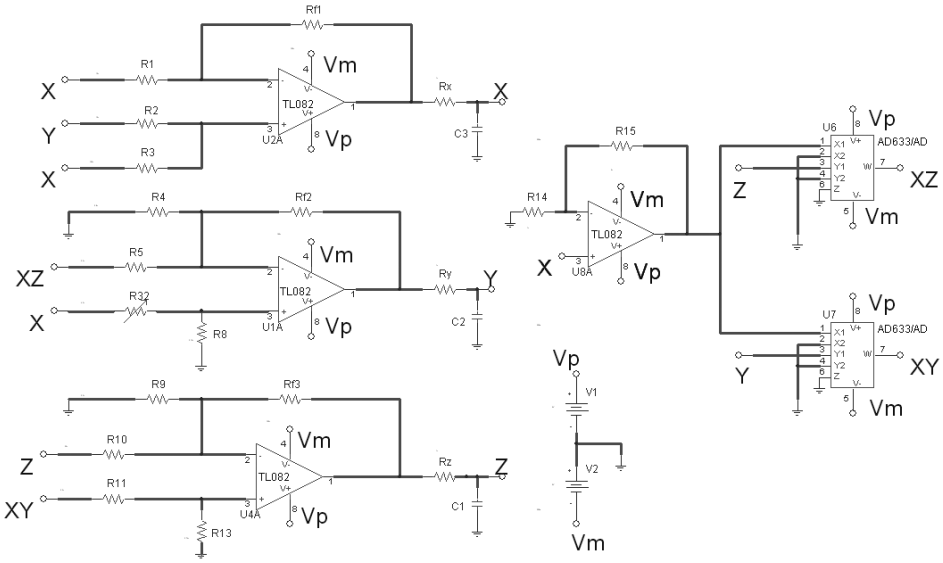

Fig.1.18 Circuit diagram of Lorenz model used in the experiment. Kit's components: C1=200nF, C2=200nF, C3=200nF, R3=100kΩ, Rf1=100kΩ, Rf2=100kΩ, R4 =5.6kΩ, R5=3.3kΩ, R9=3.3kΩ, R11=3.3kΩ, R8=3.19kΩ, R1=10kΩ, R2=10kΩ, R13=3.74kΩ, R14=1kΩ, Rx=1kΩ, Ry=1kΩ, Rz=1kΩ, R15=9kΩ, R10=39kΩ, R32=4.2kΩ, power supply $=\pm 9V$

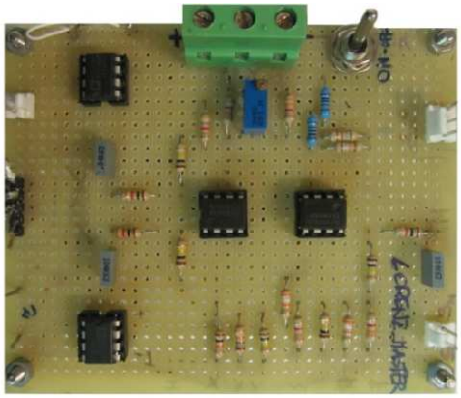

Fig.1.19 – Hardware implementation of the Lorenz's circuit.

The circuital equations associated to the implementation of Lorenz circuit are:

$$\begin{aligned} C_3 R_x \dot{x} &= -x - \frac{R_{f1}}{R_1} x + \frac{R_{f1}}{R_2} y + \frac{R_{f1}}{R_2} x \\ C_2 R_y \dot{y} &= -y - \frac{R_{f2}}{R_5} XZ + \frac{R_{f2}}{R_{32}} x \\ C_1 R_z \dot{z} &= -z + \frac{R_{f3}}{R_{10}} z + \frac{R_{f3}}{R_{11}} XY \end{aligned} \tag{1.30}$$

where we have taken into account that the output of AD633 is as in (1.16):

$$\begin{aligned} XZ &= xz \\ YZ &= yz \end{aligned} \tag{1.31}$$

Matching equations (1.30) with the mathematical model in (1.29), it is possible to choose the values of components. Using low cost components, the chaotic attractor can be obtained as shown in Fig.1.20. The different behavior shown by the Lorenz circuit by varying the single bifurcation parameter ρ can be observed in the circuit by varing resistor R32.

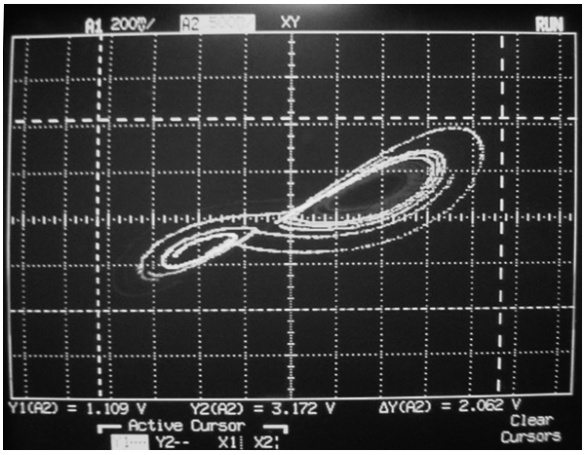

Fig.1.20 –Lorenz's attractor.

4. The Rossler's circuit

The dimensionless equations of Rössler's system [105] are:

$$\begin{aligned} \dot{x} &= -y - z \\ \dot{y} &= x + ay \\ \dot{z} &= b + xz - cz \end{aligned} \tag{1.32}$$

where $a = b = 0.2$ and $c = 14$.

As shown in the simulation trend of Fig.1.21 and Fig.1.22, obtained with Matlab, the behavior of x, y and z variable exhibits the typical features of a chaotic system.

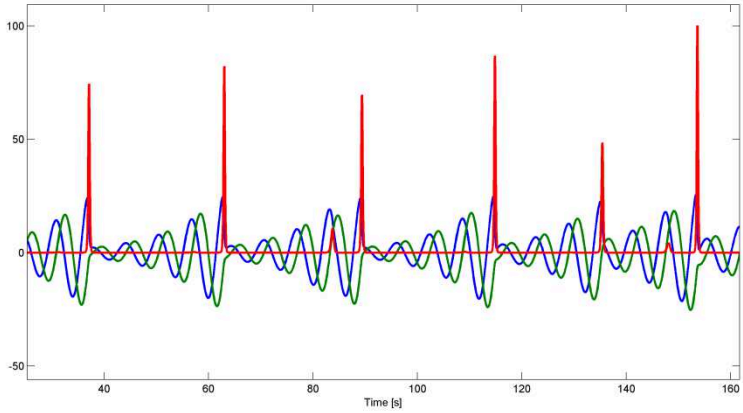

Fig.1.21 Theoretical trend of x (blue), y (green), and z (red) variables.

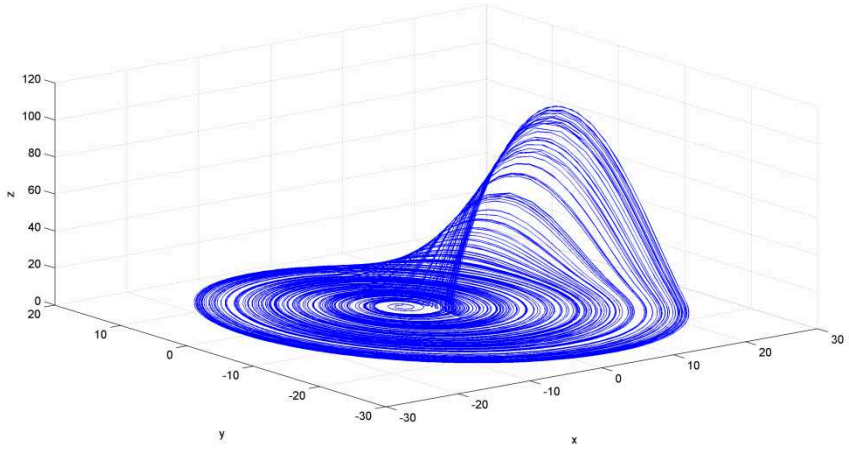

Fig.1.22 – Theoretical Rossler's attractor.

This system has a dynamic with amplitudes that exceed the required range, so it is necessary a mathematical trasformation to reduce the amplitude. The trasformations adepte are the following:

$$\begin{aligned} x_{new} &= \frac{x_{old}}{10} \\ y_{new} &= \frac{y_{old}}{10} \\ z_{new} &= \frac{z_{old}}{10} \end{aligned} \tag{1.33}$$

The rescaled system is as follows:

$$\begin{aligned} \dot{x} &= -y - z \\ \dot{y} &= x - ay \\ \dot{z} &= 0.1b + 10xz - cz \end{aligned} \tag{1.34}$$

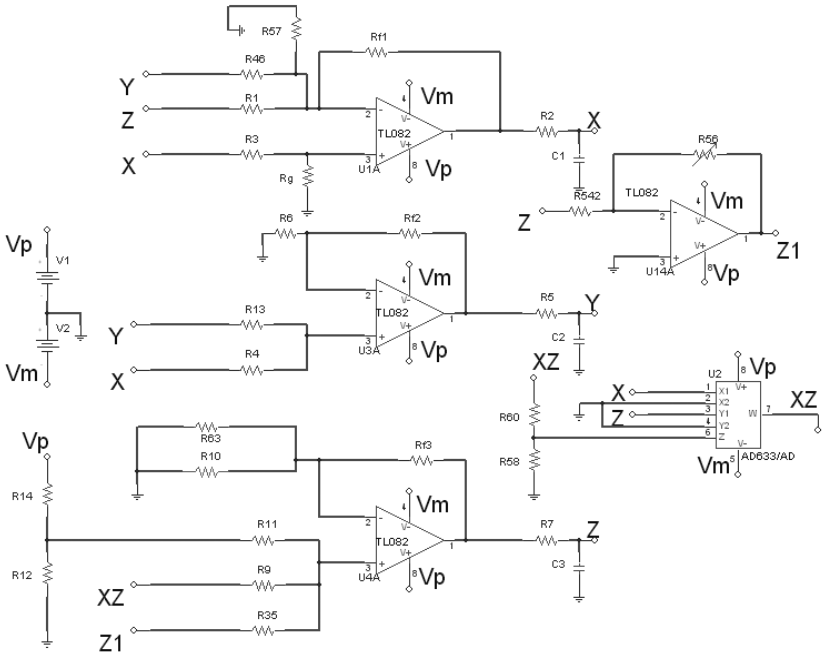

Fig.1.23 Circuit diagram of the Rossler model. Kit's components: C1=100nF, C2=100nF, C3=100nF, R2=1kΩ, R5=1kΩ, R7=1kΩ, R12=1kΩ, R60=1kΩ, R6=78kΩ, R13=78kΩ, R9=10kΩ, R10=10kΩ, R542=10kΩ, R1=100kΩ, R3=100kΩ, R4=100kΩ, R11=100kΩ, R35=100kΩ, R46=100kΩ, R57=100kΩ, R63=100kΩ, Rf1=100kΩ, Rf2=100kΩ, Rf3=100kΩ, R14=449kΩ, R58=9kΩ, Rg=33.3kΩ, R56=177kΩ. Power supply = $\pm 9V$

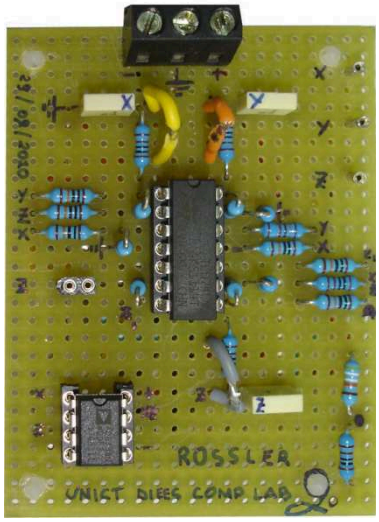

Fig.1.24 – Hardware implementation of the Rossler's circuit.

The circuital equations associated to the implementation of Rossler circuit are:

$$\begin{aligned} C_1 R_2 \dot{x} &= -x - \frac{R_{f1}}{R_{46}} y - \frac{R_{f1}}{R_1} z + \frac{R_{f1}}{R_3} x \\ C_2 R_5 \dot{y} &= -y + \frac{R_{f2}}{R_{13}} y + \frac{R_{f2}}{R_4} x \\ C_3 R_7 \dot{z} &= -z + \frac{R_{f3}}{R_{11}} \frac{R_{12}}{R_{12} + R_{14}} Vp + \frac{R_{f3}}{R_9} XZ + \frac{R_{f3}}{R_{35}} Z1 \end{aligned} \tag{1.35}$$

where, we have taken that into account the output of AD633 is as in (1.16):

$$\begin{aligned} Vp &= 9Volt \\ XZ &= \frac{xz}{10} \\ Z1 &= \frac{R_{56}}{R_{542}} z \end{aligned} \tag{1.36}$$

Matching equations (1.35) with the mathematical model in equations (1.34), it is possible to choose the values of the components. Using low cost components, it is possible to obtain the chaotic attractor shown in Fig.1.25. The different behavior shown by the Rossler circuit by varying the single bifurcation parameter c can be observed in the circuit by varing resistor R56.

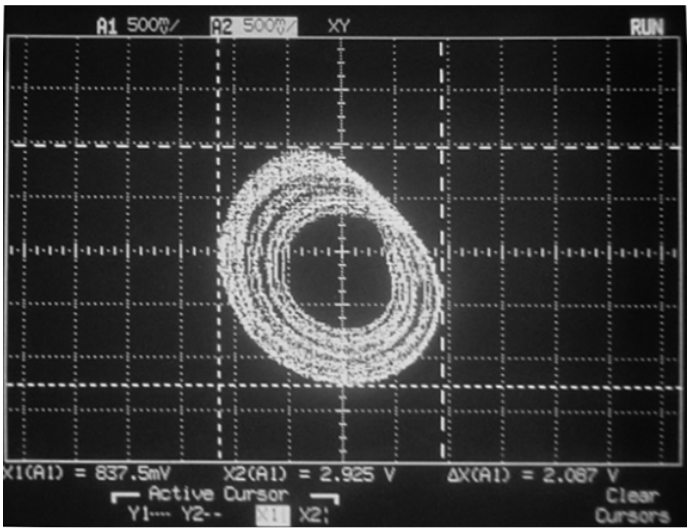

Fig.1.25 –Rossler's attractor.

5. The Hindmarsh-Rose's circuit

In traditional artificial neural networks, the neuron behavior is described only in terms of firing rate, while most real neurons, commonly known as spiking neurons, transmit information by pulses, also called action potentials or spikes. The Hindmarsh-Rose (HR) model [106] is computationally simple and capable of producing rich firing patterns

exhibited by real biological neurons. Nevertheless, the HR model is also able to mimic neuronal bursting. It consists of three coupled first order differential equations , it can generate a tonic spiking, phasic spiking, and so on, for different parameters in the model equations.
The dimensionless equations of Hindmarsh-Rose's circuit consist of the following three state equations:

$$\begin{aligned} \dot{x} &= y - ax^3 + bx^2 - z + I \\ \dot{y} &= c - dx^2 - y \\ \dot{z} &= r(s(x - \chi) - z \end{aligned} \tag{1.37}$$

where x represents the membrane potential y and z are associated with fast and slow currents, respectively.
I is an applied current, and a, α, μ, b and c are constant parameters and in particular $a = 1$, $b = 3$, $c = 1$, $d = 5$, $r = 0.002$, $s = 4$, $\chi = -1.6$
As shown in the simulation trend of Fig.1.26, obtained with Matlab, the behavior of x, y and z variable exhibits the typical features of a chaotic system.

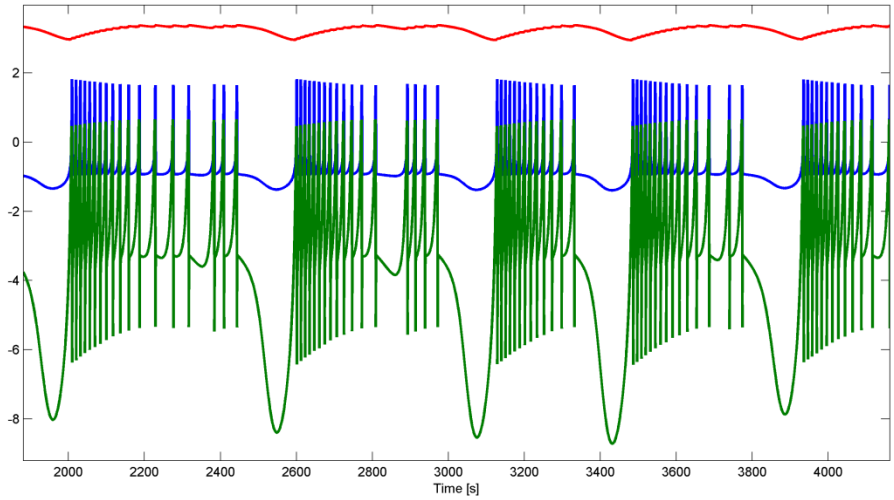

Fig.1.26 – Theoretical trend of x (blue), y (green), and z (red) variables.

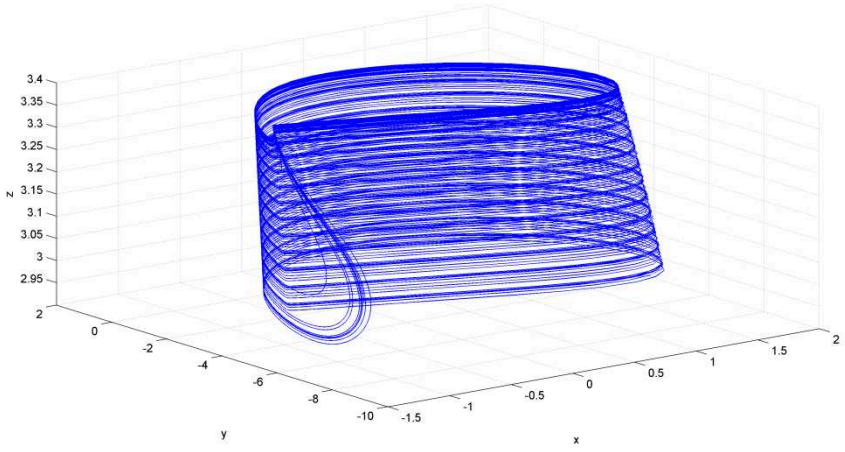

Fig.1.27 – Theoretical HR attractor

.

Following the SC-CNN approach, in Fig. 1.28 an electronic circuit has been designed with Spice's tool and in Fig. 1.31 realized using resistors, capacitors and operational amplifiers. To simplify the construction of the circuit, the circuit is built in two subparts, as shown in the diagram in Fig.1.29 and Fig.1.30, which implements the square sub-circuit and the cube sub-circuit.

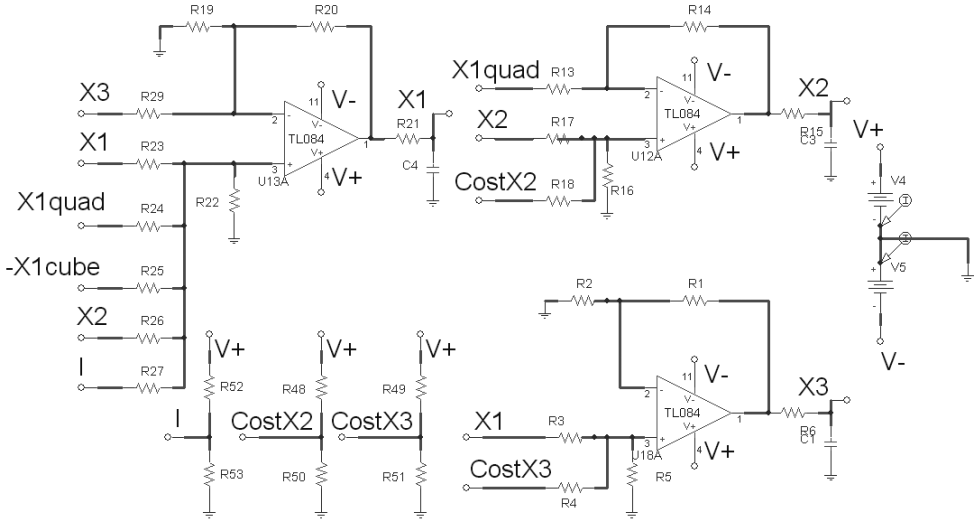

Fig.1.28 SC-CNN based implementation of HR's circuit. Kit's components: D1=D2,=D3=D4=D5=D6=D7=D8=D9=D10=D11=1N4148, C3=1uF, C4=1uF, C1=467uF, R1=200kΩ, R20=200kΩ, R23=200kΩ, R36=200kΩ, R40=200kΩ, R2=10kΩ, R19=10kΩ, R30=10kΩ, R31=10kΩ, R34=10kΩ, R35=10kΩ, R45=10kΩ, R46=10kΩ, R3=20kΩ, R4=100kΩ, R14=100kΩ, R18=100kΩ, R37=100kΩ, R39=100kΩ, R5=22kΩ, R6=1kΩ, R21=1kΩ, R50=1kΩ, R51=1kΩ, R53=1kΩ, R13=32kΩ, R25=32kΩ, R15=200Ω, R16=43kΩ, R17=125kΩ, R22=36kΩ, R24=26.6kΩ, R26=250kΩ, R27=500kΩ, R29=500kΩ, R32=4kΩ, R33=30kΩ, R42=12kΩ, R43=15k, R44=2kΩ, R47=70kΩ, R48=89kΩ, R49=1.81kΩ, R52=2.17kΩ. Power supply = $\pm 15V$.

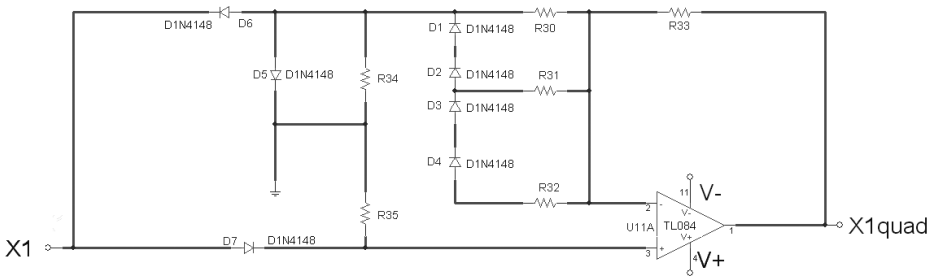

Fig. 1.29 Sub-circuit that realizes the square, X1quad=X1².

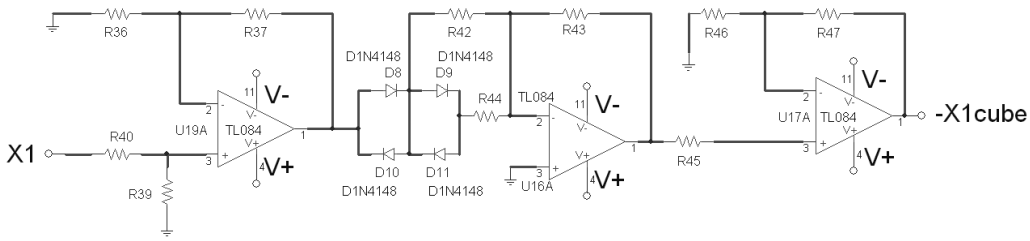

Fig. 1.30 Sub-circuit that realizes inverted cube, X1quad=-X1^3.

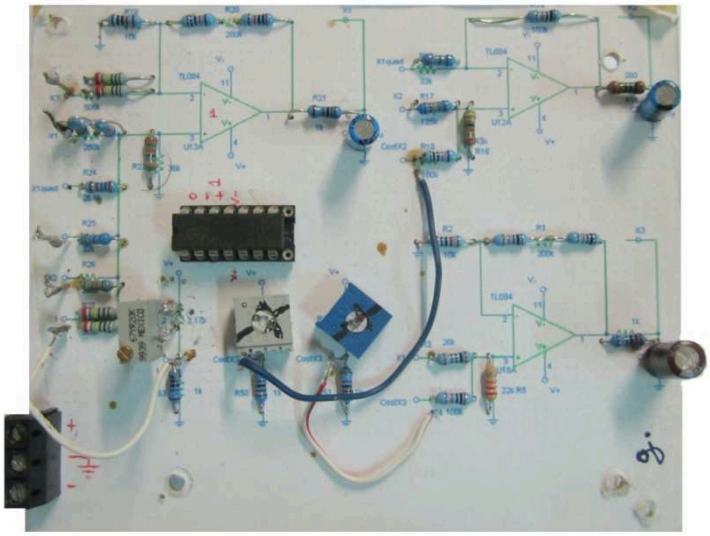

Fig.1.31 Hardware implementation of HR model.

The circuital equations associated to the implementation of HR circuit are:

$$
\begin{aligned}
C_4 R_{21}\dot{x} &= -x - \frac{R_{20}}{R_{29}} z + \frac{R_{20}}{R_{23}} x + \frac{R_{20}}{R_{24}} X1quad + \frac{R_{20}}{R_{25}}(-X1cube) + \frac{R_{20}}{R_{26}} y + \frac{R_{20}}{R_{27}} I \\
C_3 R_{15}\dot{y} &= -y - \frac{R_{14}}{R_{13}} X1quad + \frac{R_{14}}{R_{17}} y + \frac{R_{14}}{R_{18}} CostX2 \\
C_1 R_6 \dot{z} &= -z + \frac{R_1}{R_3} x + \frac{R_1}{R_4} CostX3
\end{aligned}
\tag{1.38}
$$

$$
\begin{aligned}
&X1quad = x^2 \\
&-X1cube = -x^3 \\
&I = \frac{R_{53}}{R_{52}+R_{53}}V_+ \\
&CostX2 = \frac{R_{50}}{R_{50}+R_{48}}V_+ \\
&CostX3 = \frac{R_{51}}{R_{49}+R_{51}}V_+
\end{aligned}
\tag{1.39}
$$

Matching equations (1.38) with the mathematical model in (1.37), it is possible to choose the valuesof the values of components. Using low cost components it is possible to obtain the chaotic behavior shown in Fig.1.32. R52 can be varid to control the system bifurcations.

Fig.1.32 – Experimental trend of x variable, obtained for I=1.89 more precisely for $R_{52} = 2.17k\Omega$.

6. The Duffing's circuit

The dimensionless equations of the Duffing's circuit consist of the following three state equations:

$$\begin{aligned} \dot{x} &= y \\ \dot{y} &= x - x^3 - dy + g\sin(wt) \end{aligned} \tag{1.40}$$

where $d = 0.25$, $g = 0.3$ and $w = 1$.
Fig.1.33 shows the trend of the state variables obtained with Matlab.

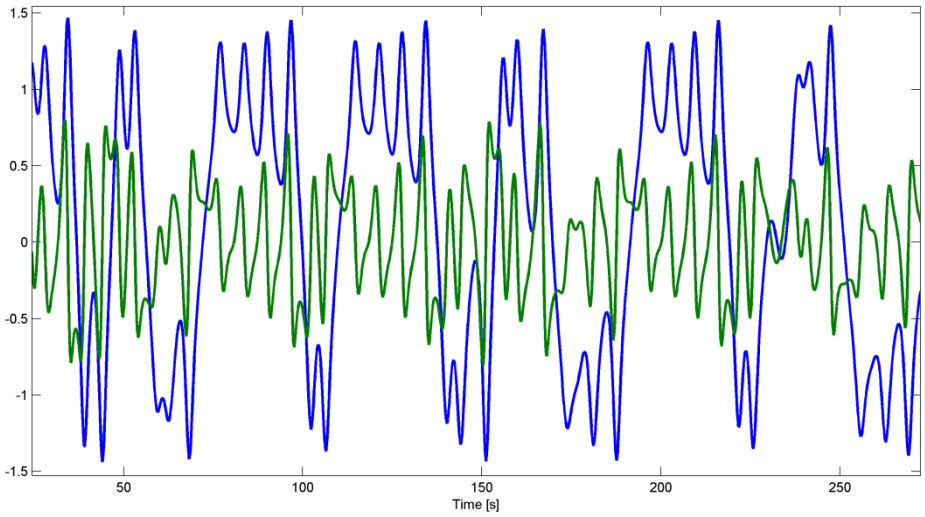

Fig.1.33 Theoretical trend of x (blue) and y (green) variables.

In Fig.1.34 , the typical chaotic attractor shown.

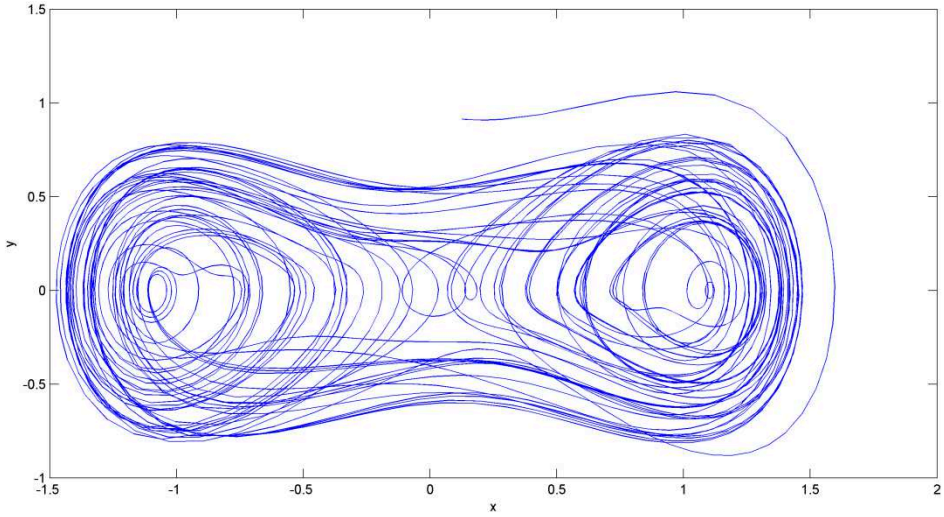

Fig.1.34 Theoretical Duffing's attractor.

In the implementation of the model (1.40), the Miller integrator configuration was chosen as can be seen in the circuit diagram in Fig.1.35.

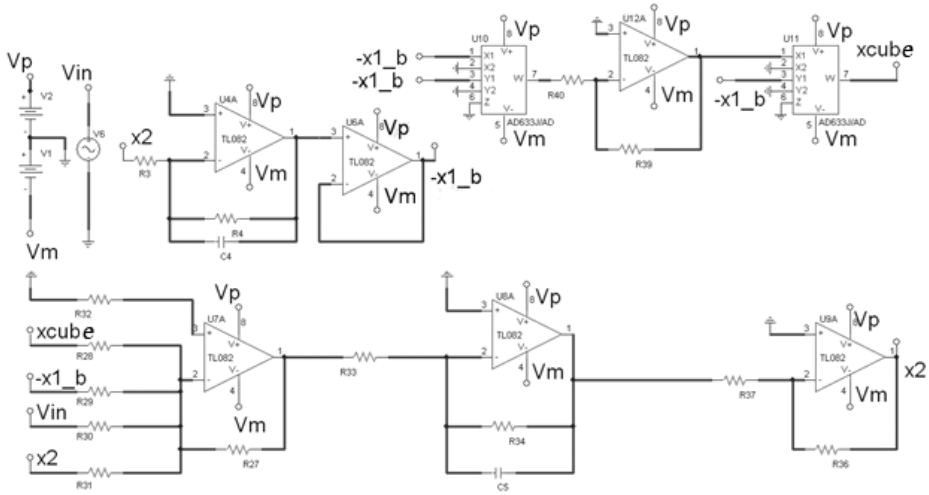

Fig.1.35 Hardware implementation of Duffing circuit. Kit's components: C4=100nF, C5=100nF, R31 =4kΩ, R32=75Ω, R39=10kΩ, R4=1kΩ, R27=1kΩ, R29=1kΩ, R30=1kΩ,

R34=1kΩ, R36=1kΩ, R37=1kΩ, R40=1kΩ, R3=100Ω, R28=100Ω, R33=100Ω. The parameter of Vin signal are: f=15.9kHz, Vamplitude=0.3V, Voffset=0, Power supply = $\pm 9V$.

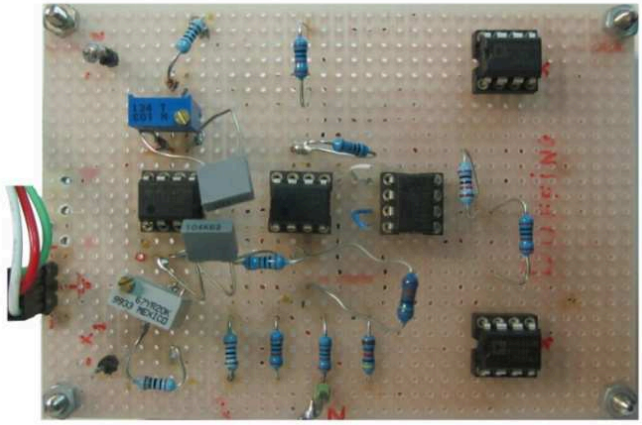

Fig.1.36 Hardware implementation of Duffing's circuit.

The circuital equations associated to the implementation of the Duffing circuit as shown in (1.36) is reported in (1.41).

$$\begin{aligned} C_4 R_4 \dot{x} &= -x + \frac{R_4}{R_3} y \\ C_5 R_{34} \dot{y} &= -y - \frac{R_{34}}{R_{33}} \left(\frac{R_{27}}{R_{28}} xcube + \frac{R_{27}}{R_{29}} (-x1\_b) - \frac{R_{27}}{R_{30}} Vin + \frac{R_{27}}{R_{31}} y \right) \end{aligned} \tag{1.41}$$

with

$$\begin{aligned} xcube &= x^3 \\ -x1\_b &= -x \end{aligned} \tag{1.42}$$

Vin corresponds to an external sinusoidal wave with amplitude=0.3V and frequency = 15.9kHz.
Matching equations (1.41) with the mathematical model (1.40), it is possible to choose the values of the components. Varying the amplitude

g of the external sinusoidal wave, different chaotic attractors can be observed.

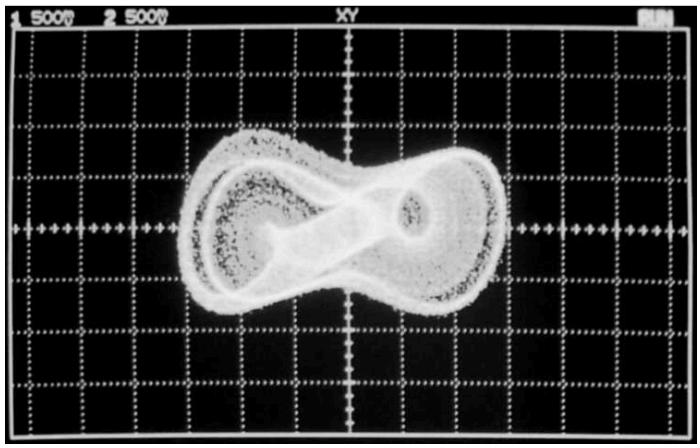

Fig.1.37 Experimental Duffing's attractor for g=0.8V.

7. Memristive circuit

Memristors are gaining an increasing interest in the scientific community for their possible applications, e.g. high–speed low–power processors or new biological models for associative memories. Due to the intrinsic nonlinear characteristic of memristive devices, it is possible to use them in the design of new dynamical circuits able to show complex behavior, like chaos. In this paragraph, a new memristive chaotic circuit is presented discussing, in particular, an approach based on Cellular Nonlinear Networks for the implementation of the memristive device. The approach investigated in this work allows to obtain memristor with common off-the-shelf components and to observe the onset of new chaotic attractors in nonlinear circuits with memristors. The circuits presented here, being the first example of memristive chaotic circuits based on CNNs, can be considered as the link between the three inventions by Leon O. Chua, i.e. the memristor [107], the first chaotic electronic circuit and the Cellular Nonlinear Networks.
The dimensionless equations [78] of the memristive circuit consist of the following four state equations:

$$\begin{aligned}\dot{x} &= 0.8y - 4xW(w)\\ \dot{y} &= z - 5x\\ \dot{z} &= -\beta y + \gamma z\\ \dot{w} &= 10x\end{aligned} \tag{1.43}$$

where

$$W(w) = \begin{cases} 4, & |w| < 1 \\ 10, & |w| > 1 \end{cases} \tag{1.44}$$

and $\beta = 1$, $\gamma = 0.65$.

As shown in the simulation trend of Fig.1.38, obtained with Matlab, the behavior of x, y,z and w variable exhibits the typical features of a chaotic system.

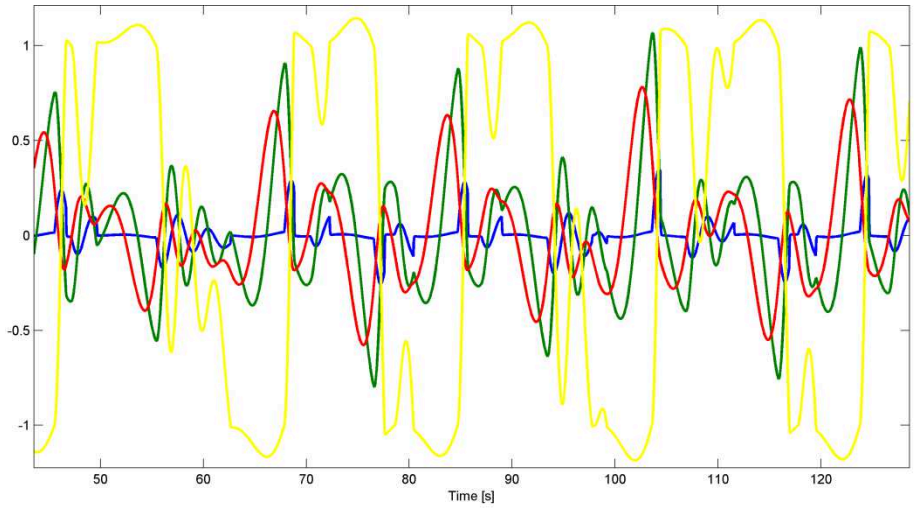

Fig.1.38 Theoretical trend of x (blue), y (green), z (red) and w (yellow) variables of the memristive model.

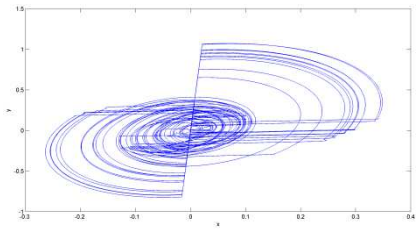

xy

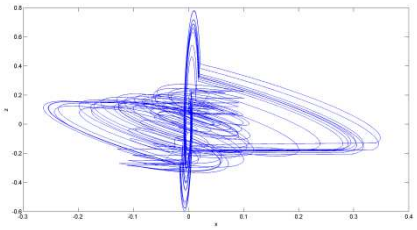

xz

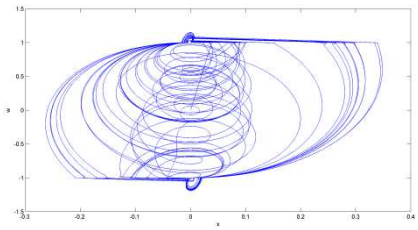

xw

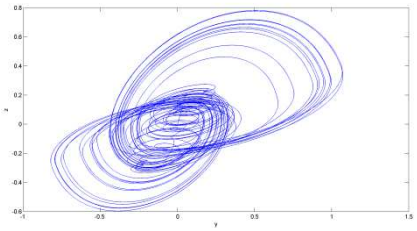

yz

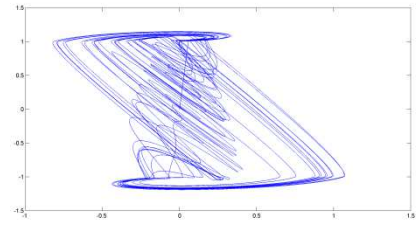

yw

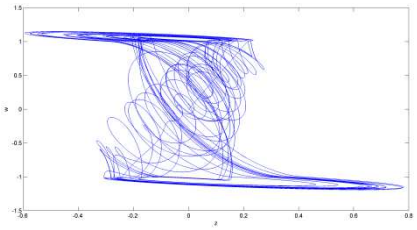

zw

Fig.1.39 Theoretical attractors of memresistive circuit.

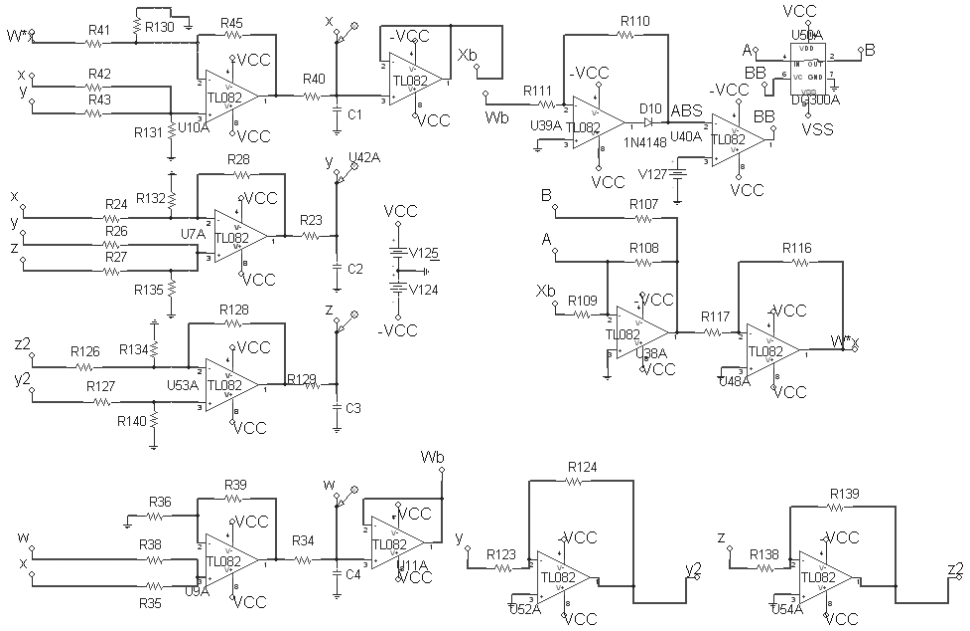

Fig.1.40 Memristive circuit. Kit's components: D10=1N4148, C1=100nF, C2=100nF, C3=100nF, C4=100nF, R24=200kΩ, R135=40kΩ, R26=200kΩ, R27=200kΩ, R28=200kΩ, R38=200kΩ, R39=200kΩ, R123=200kΩ, R126=200kΩ, R127=200kΩ, R128=200kΩ, R132=200kΩ, R134=200kΩ, R139=200kΩ, R35=20kΩ, R36=20kΩ, R41=50kΩ, R42=198kΩ, R43=241kΩ, R130=241kΩ, R23=10kΩ, R34=10kΩ, R40=10kΩ, R108=10kΩ, R110=10kΩ, R111=10kΩ, R129=10kΩ, R107=196Ω, R109=1kΩ, R116=1kΩ, R117=1kΩ, R124=165kΩ, R131=25kΩ, R138=121.2kΩ, R140=100kΩ, R45=198kΩ, DG300A=switch.

The circuital equations associated to the implementation of the memresistive circuit (1.43) are:

$$
\begin{aligned}
C_1 R_{40}\dot{x} &= -\frac{R_{45}}{R_{29}}(W * x) + \frac{R_{45}}{R_{23}}x + \frac{R_{45}}{R_{24}}y \\
C_2 R_{23}\dot{y} &= -\frac{R_{28}}{R_{13}}x + \frac{R_{28}}{R_{17}}y + \frac{R_{28}}{R_{18}}z \\
C_3 R_{129}\dot{z} &= -\frac{R_{128}}{R_3}Z2 + \frac{R_{128}}{R_4}Y2 \\
C_4 R_{34}\dot{z} &= \frac{R_{39}}{R_{38}}w + \frac{R_{39}}{R_{35}}x
\end{aligned}
\tag{1.45}
$$

where we have used some particular configurations to realize the function presented in equation (1.44).
In particular it has been used the rectifier configuration in Fig.1.41, combined with the comparator shown in Fig.1.42 with V127=1V, and the fast switch in Fig.1.43 that uses, the output of the comparator as control signal.

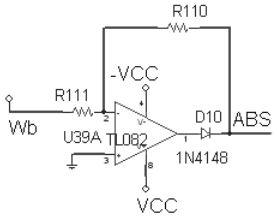

Fig.1.40 Rectifier configuration.

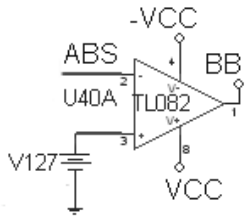

Fig.1.42 Comparator.

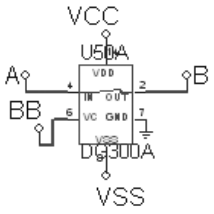

Fig.1.43 AD300A fast switch.

Matching equations (1.45) with the mathematical model (1.43), it is possible to choose the values of the components. In the Fig.1.44, the Lissajous figures are reported.

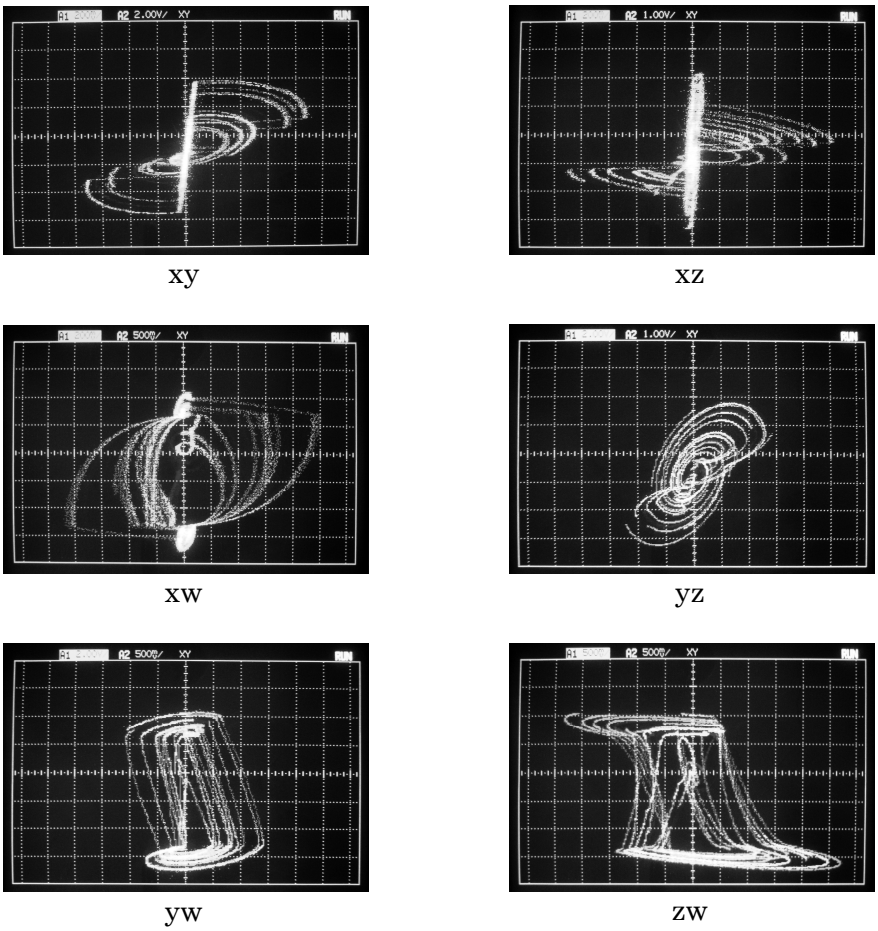

Fig.1.44 Lissajous figures of the memristive circuit.

8. The Langford's circuit

The dimensionless equations of Langford's circuit consist of the following three state equations:

$$\begin{aligned}\dot{x} &= xz - wy \\ \dot{y} &= wx + yx \\ \dot{z} &= p + z - \frac{1}{3}z^3 - (x^2 + y^2)(1 + qx + \varepsilon x)\end{aligned} \tag{1.46}$$

where $p = 0.7 \div 1.2,\ q = 0.7,\ w = 10,\ \varepsilon = 0.5.$

As shown in the simulation trend of Fig.1.45, obtained with Matlab, the behavior of x, y and z variable exhibits a typical features of a chaotic system.

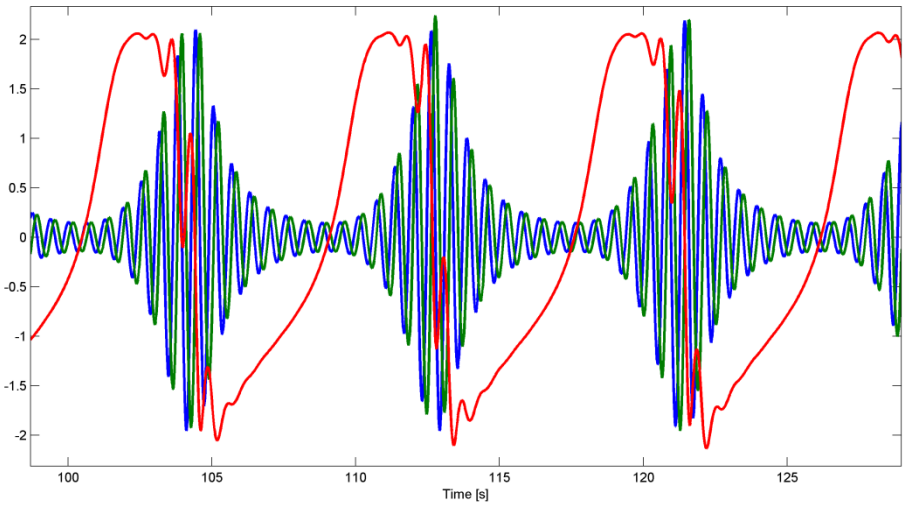

Fig.1.45 Theoretical trend of x(blue), y(green) and z(red) variables of the Langford model.

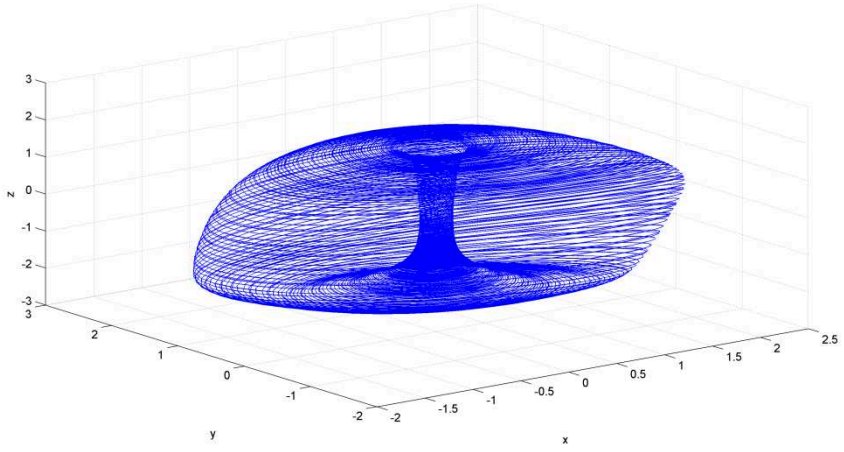

Fig.1.46 Theoretical Langford attractor

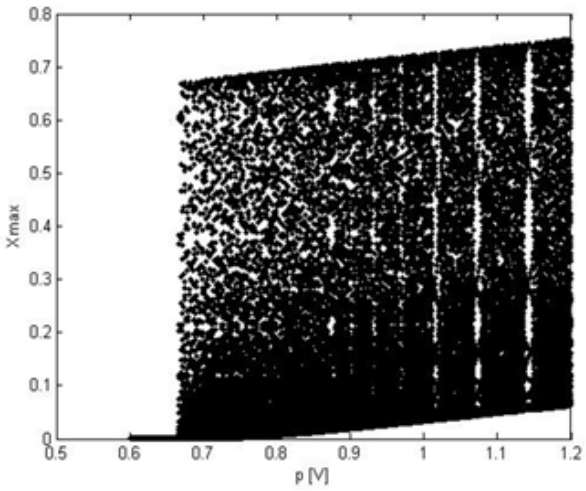

Fig.1.47 Theoretical bifurcation of Langford circuit.

For this model, to rescale the system it has been necessary to apply a transformation as follow:

$$
\begin{aligned}
x_{new} &= \frac{x_{old}}{3} \\
y_{new} &= \frac{x_{old}}{3} \\
z_{new} &= \frac{x_{old}}{2}
\end{aligned}
\tag{1.47}
$$

The rescaled system is as follows:

$$
\begin{aligned}
\dot{x} &= 2xz - wy \\
\dot{y} &= wx + 3yx \\
\dot{z} &= \frac{p}{2} + z - \frac{4}{3}z^3 - \frac{9}{2}(x^2 + y^2)(1 + 3qx + 3\varepsilon x)
\end{aligned}
\tag{1.48}
$$

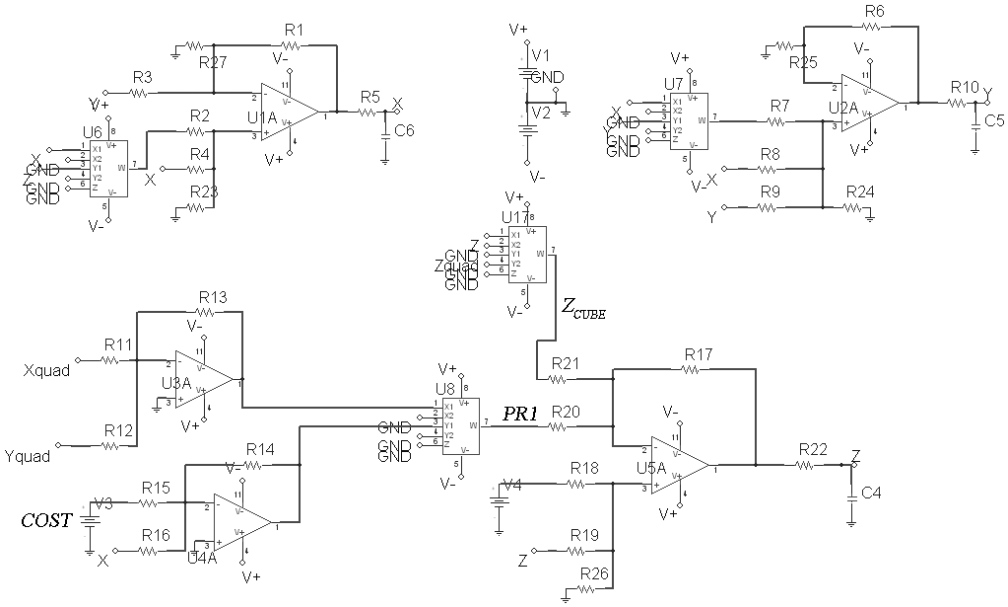

Fig.1.48 Circuit diagram of Langford model.

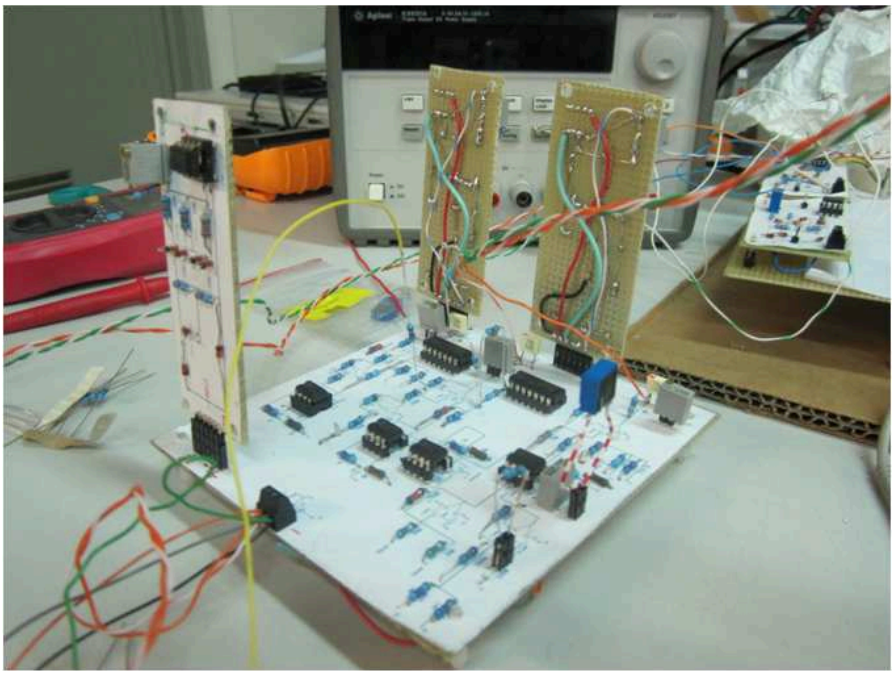

Fig.1.49 Hardware implementation of the Langford's circuit.

The circuital equations associated to the implementation of the Langford circuit are:

$$\begin{aligned} C_6 R_5 \dot{x} &= -x - \frac{R_1}{R_3} y + \frac{R_1}{R_2} xz + \frac{R_1}{R_4} x \\ C_5 R_{10} \dot{y} &= -y + \frac{R_6}{R_7} xy + \frac{R_6}{R_8} x + \frac{R_6}{R_9} y \\ C_4 R_{22} \dot{z} &= -z - \frac{R_{17}}{R_{21}} Z_{CUBE} - \frac{R_{17}}{R_{20}} PR1 + \frac{R_{17}}{R_{18}} COST + \frac{R_{17}}{R_{19}} z \end{aligned} \tag{1.49}$$

where, taking into account that the output of AD633 is as in (1.16) and using the square sub-circuit in Fig.1.29 and the cube sub-circuit in Fig.1.30, it is possible to match equations (1.49) with the mathematical model (1.48) and consequently to choose the values of the components. The different behaviors shown by the Langford circuit by varying the

single bifurcation parameter p can be observed in the circuit by varyng resistor R15.

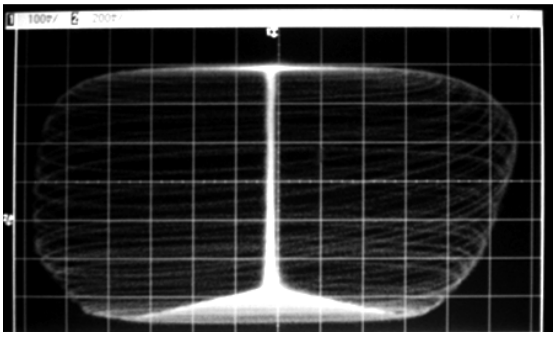

Fig.1.50 Experimental attractors of theLangford's circuit.

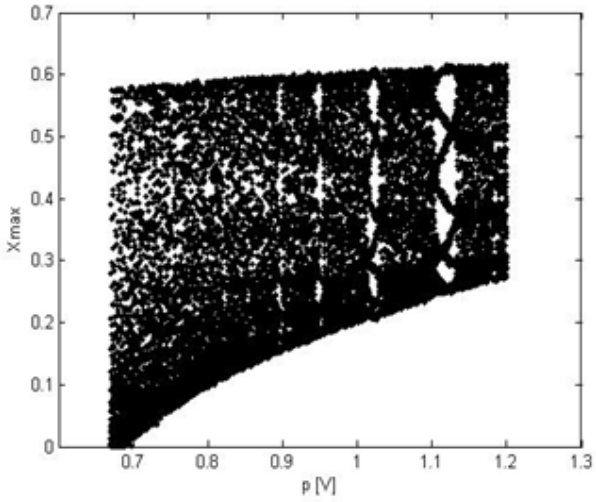

Fig.1.51 Experimental bifurcation of the Langford's circuit.

9. The Colpitts circuit

The Colpitts oscillator [108] is one of the simplest examples of an electronic oscillator. The term refers to several possible configurations in which the combination of an inductance, two capacitors, some resistances and a nonlinear element (in general, a transistor) is used to gen-

erate periodic waveforms. Peculiarities of this type of oscillators are simplicity and robustness. Recently, it has been demonstrated that for some parameters a chaotic behavior can also be obtained, thus showing that it is possible to design Colpitts oscillators able to generate high-frequency chaotic signals. The circuital equations of chaotic Colpitts circuit are represented by the following state equations:

$$\begin{aligned}\dot{x} &= \frac{1}{C_1}(I_L - \beta I_B)\\ \dot{y} &= \frac{1}{C_2}(\frac{V_{ee} - V_2}{R_2} + I_L + I_B)\\ \dot{z} &= \frac{1}{L}(V_{CC} - V_1 - V_2 - I_L R_1)\end{aligned} \tag{1.50}$$

where $I_B = 0$ if $V_{BE} \le V_{th}$ and $I_B = \frac{V_{BE} - V_{th}}{R_{ON}}$ if $V_{BE} > V_{th}$ and β and R_{ON} are the forward current gain and the small-signal on-resistance of the base-emitter junction of the transistor, respectively.

In the experimental setup these parameters are estimated as $\beta = 200$ and $R_{ON} = 100\Omega$.

In Fig.1.5 the electronic circuit is shown, while tool and in the Fig.1.53 reports the ciruit realized using off-the-shelves resistors, capacitors and inductors.

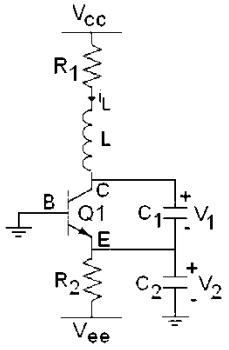

Fig.1.52 Chaotic Colpitts oscillator. Components: R_1 = 35Ω, R_2 = 500Ω, C_1 = 54nF, C_2 = 54nF, L = $98.5\mu H$, Lc = $23\mu H$, Q_1 = BJT2N2222, Vcc = 5V , Vee = -5V .

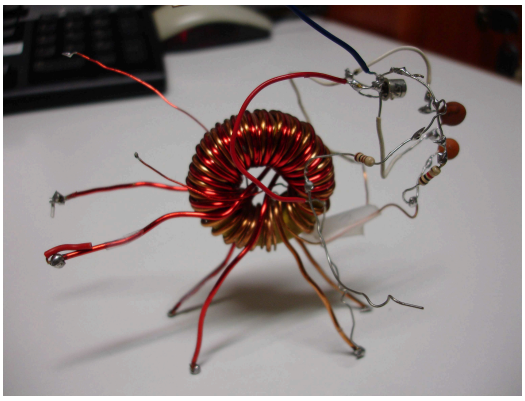

Fig.1.53 Colpitts oscillator realized with recycled components.

In Fig.1.54, the Lissajous figure obtained with the Colpitts oscillator is reported.

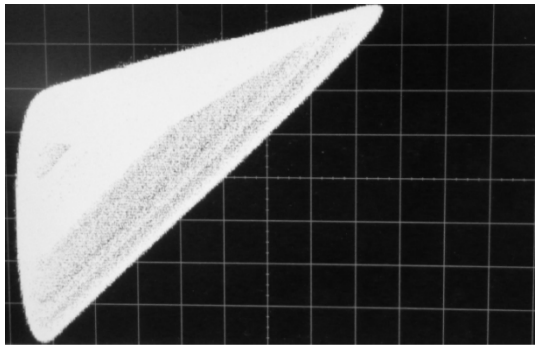

Fig.1.54 Projection on the plane V_{C2}-V_{C1} of the Colpitts attractor. Horizontal axis: 200mV/div; vertical axis 500mV/div.

Chapter 2

DESIGN OF TIME-DELAY CHAOTIC ELECTRONIC CIRCUITS

This chapter deals with the problem of the design and the implementation of time-delay chaotic circuits. A simple feedback scheme consisting of a nonlinearity, a first-order *RC* circuit and a delay block has been fixed and a procedure to design the characteristics of these blocks in order to obtain chaotic dynamics has been introduced. A series of Bessel filters in cascade is used to implement the time-delay. The suitability of the approach is demonstrated introducing two new chaotic circuits implemented with off-the-shelf discrete components. The approach allows us to design and implement a new class of time-delay chaotic circuits with simple components, like resistors, capacitors, and operational amplifiers.

2.2. Time-delayed nonlinear systems

The presence of time-delay in dynamical systems is particularly significant, since it may represent a source of instability or, in general, may induce undesired oscillations and, thus, poor performance [1]. However, the existence of time-delay in nonlinear dynamical systems, by making the system infinite-dimensional, may be beneficial, allowing the occurrence of complex dynamics and, in particular, chaos.

Mathematical models which include time-delays and exhibit chaos can be found in various fields. In particular, high-dimensional chaos induced by time-delay in feedback systems has been reported in [2], while in [3] the use of chaos generated by systems with time-delays for the transmission of encrypted information has been discussed. Several other examples of chaotic behavior in time-delayed systems have been observed in purely mathematical models [4], [6], in biological systems [7], [8] and, in particular, in neural systems, where time-delays may enhance the synchronization properties of the spiking activity of coupled neural models [9]. Furthermore, delay plays an important role in controlling the behavior of dynamical systems. Delayed signals, in fact, are used for chaos control according to a technique, proposed in [10], based on the OGY method [11]. According to this method [10], one of the unstable periodic orbits contained in the chaotic attractor is stabilized through the feedback of a small time-dependent perturbation, realized by comparing a measurable state variable to a signal obtained delaying the state variable itself.

Despite the abundance of examples of mathematical models of time-delayed systems with chaotic behavior, few chaotic electronic circuits with time-delay are reported in literature, for example [12]–[16]. In fact, the main issue in designing time-delayed circuits is a suitable choice of the circuitry devoted to the implementation of low frequency delays.

The use of delay lines is a common solution for the distribution of clock signals among logic gates. Flat spiral lines or serpentine lines provide maximum delay times in the order of micro-seconds [17]. These solutions can be adopted for the design of high-frequency chaos generators, while if larger delays are needed, other possibilities should be explored. Low frequency chaotic circuits, on the other hand, are useful for different potential applications: chaos-based noise generators [18], improvement of sensors [19] and of motion capabilities in robotics [20]. A different implementation consists in a network of T-type LCL filters and has been adopted in [13], [14] to obtain a chaotic circuit based on the Mackey-Glass model [7]. This latter solution allows to obtain delays up to a maximum of 3ms. However, the implementation based on T-type LCL filters has the drawback of parasitic resistive effects of inductances

whichcan not be neglected since they produce a strong attenuation of the delayed signal.
Aim of this work is to introduce a new class of time-delayed chaotic circuits. First, a general feedback scheme based on three simple blocks (a nonlinearity, an integrator and a time-delay block implemented through n Bessel filters in cascade) is introduced, and, then, the conditions for the existence of chaos in such scheme are discussed. In order to generate different dynamics with the same conceptual scheme introduced, only the nonlinearity and the parameters of the circuit have to be changed. Moreover, a strategy to fix such parameters, to approximatethe delay and to evaluate the approximation error has been introduced, and, then, applied to the design of a time-delay chaotic circuit. The circuit has been then implemented with off-the-shelf discrete components and experimentally investigated, showing the suitability of the approach for designing chaotic circuits with large (in the order of milliseconds) time-delays.

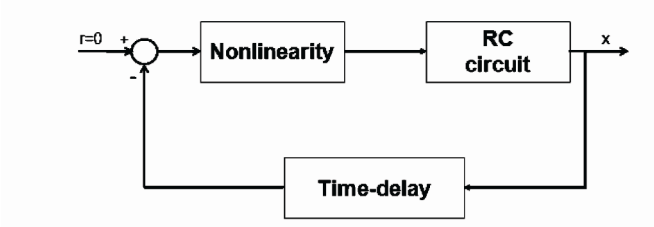

Fig. 2.1. Feedback scheme of the time-delay chaotic circuit.

2.3. Design procedure for time-delay chaotic systems

In this paragraph the feedback scheme shown in Fig. 2.1 is investigated. It represents a simple feedback scheme of a nonlinear system containing all the elements strictly needed to have the possibility that chaotic behavior emerges. It consists of three blocks: a nonlinearity, a *RC* circuit, and a time-delay block. It represents a minimal configuration to observe chaotic dynamics in autonomous time-delay circuits. The nonlinearity is needed since chaos is a prerogative of nonlinear circuits; the *RC* circuit implements the dynamics of the single state variable; and the

presence of the delay makes the system infinite-dimensional, allowing chaos to be observed in a system with a single state variable.
In terms of dimensionless equations, the dynamics of the system shown in Fig. 2.1 can be expressed as follows:

$$\dot{x}(t) = k(-ax(t) - bh(x(t-\tau))) \tag{2.1}$$

where $x(t) \in \Re$ is the circuit state variable, $h(x) : \Re \to \Re$ is the nonlinear function, $\tau \in \Re^+$ is the time-delay, k is a scaling factor, and a and b are system parameters. b represents the gain multiplying the nonlinearity, while ka is the pole of the RC circuit. System (2.1) represents a nonlinear system in Lur'e form with dynamical linear part given by $L(s) = (ke^{-s\tau})/(s+ka)$ and feedback nonlinear part given by $N = bh(x).$

For systems in Lur'e form, it is possible to analytically derive approximate conditions for the existence of chaotic behavior. They are summarized in the following criterion [23]:

Criterion 2.1 (For the Existence of Chaos in Lur'e Systems):
The conditions required for the existence of chaos in a Lur'e system are:
1) existence of a stable predicted limit cycle;
2) existence of a separate unstable equilibrium point;
3) interaction between the unstable equilibrium point and the stable predicted limit cycle.
Additionally, it is required that the linear part has filtering properties, which in our case is always satisfied, since $L(s) = (ke^{-s\tau})/(s+ka)$
The existence of a stable predicted limit cycle is derived by applying the harmonic balance method [23]. A limit cycle solution of the type exists if the amplitude and the bias of satisfy the following equations:

$$\begin{aligned} 1 + L(0)N_0(A,B) &= 0 \\ 1 + L(jw)N_1(A,B) &= 0 \end{aligned} \tag{2.2}$$

where N_0 and N_1 are static and dynamic describing functions [25] approximations of the nonlinearity N. Solving (2.2) means to express as A function of B, i.e., A(B) from the static equation, and, then, to consider the intersections between the curve $L(jw)$ and the curve $-1/N_1(A(B),B)$ in the complex plane. Each intersection corresponds to a limit cycle with a given frequency and amplitude. The stability properties of the predicted limit cycle y_0 are inferred by applying the limit cycle criterion [26].

Criterion 2.2 (Limit Cycle Criterion):
Each intersection point of the curve $L(jw)$ and the curve $-1/N_1(A(B),B)$ corresponds to a limit cycle. If the points near the intersection, corresponding to the considered limit cycle, along the curve $-1/N_1(A(B),B)$ for increasing values of B are not encircled by the curve $L(jw)$, then the limit cycle is stable. Otherwise the limit cycle is unstable.
Let us now focus on the second condition of criterion 2.1. The equilibrium points of the system can be calculated by solving

$$a\bar{x} + bh(\bar{x}) = 0 \tag{2.3}$$

The criterion for the existence of chaos in Lur'e systems requires the existence of an equilibrium point which has to be separate from the limit cycle and unstable. We now briefly discuss how the stability properties of the equilibrium points can be checked. Since in the following piecewise linear (PWL) nonlinearities will be used, the stability of the generic equilibrium point can be analyzed taking into account the following system:

$$\dot{x}(t) = k(-ax(t) - b'h(x(t-\tau)+u)) \tag{2.4}$$

which represents the dynamics of the system (2.1) in the PWL region to which the equilibrium point under examination belongs, i.e., $b' = bm_i$ where m_i is the slope of the PWL nonlinearity in the region of the equi-

librium point E_i. u is a generic constant input. Alternatively, if h(x) is not a PWL function, linearization around E_i could be considered.
For system (2.4) two different types of asymptotic stability can be defined [24]: delay-independent (if the system (2.4) is stable for all the values of $\tau \in \Re^+$) and delay-dependent (if the system (2.4) is stable for some values of and unstable for other values of τ) stability. To check them, the following criteria [24] can be applied.

Criterion 2.3 (Delay-Independent Stability): The equilibrium point E*i* is delay-independent stable if and only if $a + b > 0$ and $a \geq |b|$.

Criterion 2.4 (Delay-Dependent Stability): The equilibrium point E*i* is delay-dependent stable if and only if $b > |a|$. The equilibrium point E*i* is stable for $\tau \leq \tau^* = (\cos^{-1}(-a/b))/(k\sqrt{(b^2 - a^2)})$.

Finally, the third condition of criterion 2.1, i.e., the interaction between the stable predicted limit cycle and the unstable equilibrium point , can be expressed as follows:

$$A \geq |E - B| \tag{2.5}$$

The system represented in Fig. 2.1 thus exhibits chaotic behavior if conditions (2.1)–(2.3) of criterion 2.1 are satisfied, i.e., if (2.2) and (2.5) admit a solution and a separate equilibrium point satisfying neither criterion 2.3 nor criterion 2.4 exists. These conditions can be satisfied by a proper choice of the nonlinearity $h(x)$ and of the parameters *a, b* and τ of system (2.1).
The time-delay τ plays an important role in conditions (2.1)–(2.3) of the criterion 2.1. τ may change the stability properties of equilibrium points (if they are delay-dependent stable) and may also affect the Nyquist diagram of $L(s)$ (and thus the conditions on the existence of the limit cycle and on its interaction with the equilibrium point). In general, when criterion 2.1 admits a solution, for a given nonlinearity and for fixed values of and , one obtains a range of values of τ, i.e.,

$\tau_{\min} \leq \tau \leq \tau_{\max}$ for which the system exhibits a chaotic behavior. Once fixed τ in this range, i.e., $\tau = \bar{\tau}$, the problem of the implementation of a circuitry introducing this delay arises. Taking into account the typical scaling factor k in discrete-components circuit implementations, this delay is in the order of magnitude of milliseconds and thus its implementation requires the definition of an appropriate strategy.
The idea underlying our approach is to implement the timedelay block with a cascade of n Bessel filters which are low-pass filters with a maximally flat magnitude and a maximally linear phase response [27]. Since a Bessel filter with transfer function H(s) introduces a time-delay up to the 3 dB frequency equal to $\tau_i = -(d\Phi(w))/(dw)$, a given delay $\bar{\tau}$ can be obtained with blocks in cascade according to

$$\bar{\tau} \cong n\tau_i \tag{2.6}$$

In this way, the time-delay can be easily tuned by changing the number n of filters in cascade. The Bessel filter implemented is an uncertain Bessel filter, since its implementation is based on off-the-shelf components with standard values, which additionally are subjected to tolerance. For this reason, it is important to evaluate the error between the model and the circuit implemented with a given n, and, if necessary, use a different number of filters in cascade. Since the implemented system is chaotic and thus sensitive to parameters, the introduced approach relies on the definition of an error measure taking into account this property. Let us consider two chaotic circuits coupled through a master slave configuration [29]. If the two circuits are identical, in general, it is possible to synchronize them, obtaining state variables which asymptotically follow the same trajectory. In the case of non-identical circuits, complete synchronization cannot be obtained, but the synchronization error is kept small if the circuits have similar parameters. Therefore, the synchronization error can be used to evaluate the accuracy of the approximation based on Bessel filters.
More in detail, let us consider

$$\begin{aligned}\dot{x}(t) &= k(-ax(t) - bh(x(t-\tau))) \\ \dot{x}_n(t) &= k(-ax_n(t) - bh(\hat{x}(t)) + k(x(t) - x_n(t)))\end{aligned} \tag{2.7}$$

where $x(t)$ is the state variable of the ideal model (2.1), i.e., with $L(s) = (ke^{-s\tau})/(s+ka)$, $x_n(t)$ is the corresponding state variable of the approximated model, i.e., with $\tilde{L}(s) = (k/s+ka)H^n(s)$, k is the coupling strength, and $\hat{x}(t)$ is the output of the n Bessel filters in cascade, which ideally is $\hat{x}(t) = x_n(t-\tau)$. Let us then define the synchronization error between the ideal model (with time-delay τ) and the approximated model (with a time-delay given by filters in cascade) as follows

$$\delta(n) = \left\langle | x(t) - x_n(t) | \right\rangle \tag{2.8}$$

where $\langle \cdot \rangle$ represents the average with respect to time. The synchronization error (2.8) is used to evaluate the accuracy of the approximated model. Moreover, n is selected to minimize this error. On the basis of the considerations discussed in this section, a procedure for the design of a time-delay chaotic circuit with the feedback scheme of Fig. 2.1 can be thus defined. The procedure is summarized in the following with the indication of the condition required and the equations and criteria that can be used to verify it.

Procedure 1: In order to design a time-delay chaotic circuit with the feedback scheme of Fig. 2.1 the nonlinearity h(x) and the circuit parameters should be selected so that the following occurs.

1) The circuit should admit a stable predicted limit cycle. Satisfy (2.2) and criterion 2.2.

2) The circuit should have an unstable separate equilibrium point. Use (3) and criteria 2.3 and 2.4.

3) The stable predicted limit cycle should interact with the unstable equilibrium point E-Use (2.5).

4) Once fixed the parameters (and in particular $\bar{\tau}$), the number of filters n for implementing the time-delay has to be chosen.—Use (2.6).
5) The accuracy of the approximation has to be evaluated with respect to different n.—Use (2.8) and choose n so that $\delta(n)$ is minimum.

This procedure defines a class of circuits with the feedback scheme of Fig. 2.1 and chaotic behavior. In the next Section, we illustrate an example of such circuits.

2.4. First circuit implementation

The feedback scheme illustrated in Fig. 2.1 is based on three blocks. We briefly discuss some general aspects on the implementation of these three blocks and, then, discuss in detail an example designed following Procedure 1.
The circuit implementation is based on operational amplifier blocks.
A first block implements the RC circuit. The time constant of the block as been chosen equal to RC=1ms, which scales the dynamics of system (2.1) by a factor equal to $k = 10^3$.

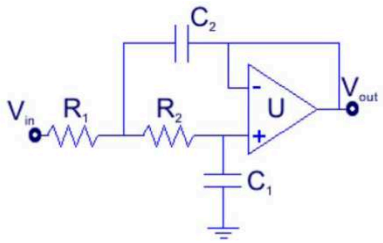

Fig. 2.2. Schematics of the Sallen-Key low-pass active filter implementing a lowpass Bessel filter.

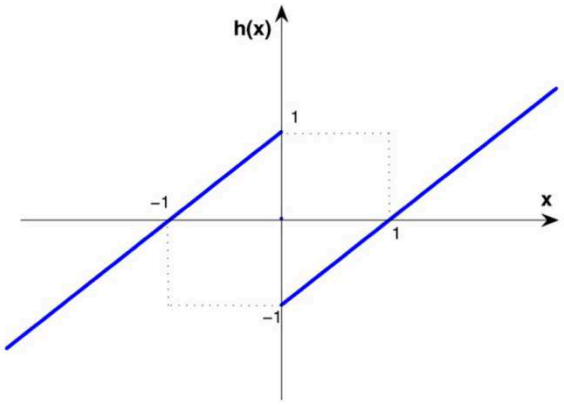

Fig. 2.3. Piece-wise linear function h(x).

A second block implements the nonlinearity of the circuit. In the example described below a PWL nonlinearity is used. PWL nonlinearities are typically found in many chaotic circuits, like in the Chua's circuit [21], and therefore design strategies for their implementation are widely studied [21], [22]. In particular, for the design of this block, the approach described in [21] has been followed. This approach exploits the saturation working region of operational amplifiers to obtain a PWL input-output characteristics with tracts with different slopes. Concerning the third block, the time-delay is implemented by using a cascade of low-pass second-order Bessel filters. Each filter is characterized by the Sallen-Key topology [30] as shown in Fig. 2.2 and by the following transfer function:

$$H(s) = \frac{1}{1 + C_1(R_1 + R_2)s + C_1 C_2 R_1 R_2 s^2} \tag{2.9}$$

The values of the filter components (listed in Appendix) have been chosen in order to realize a Bessel filter with 3 dB frequency equal to $f_c = 1kHz$ and taking into account off-theshelf component values. The time-delay introduced by this filter in the band up to f_c can be calculated as $\tau_i = -(d\phi(w))/(dw)$. In the 3 dB band, $\tau_i \approx C_1(R_1 + R_2)$.

For the values of the components in Section 2.5. Larger delays are realized by taking into account a cascade of n filters.

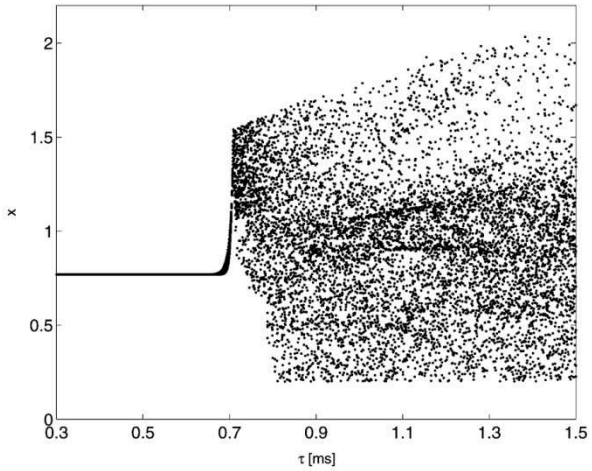

Fig. 2.4. Numerical bifurcation diagram of system (1) with nonlinearity (10) with respect to time-delay τ . Other parameters are a=1, b=3.

An example of a time-delay chaotic circuit designed by following Procedure 1 is now described. The circuit is characterized by the following PWL function h(x):

$$h(x) = \begin{cases} x+1 & if \quad x<0 \\ 0 & if \quad x=0 \\ x-1 & if \quad x>0 \end{cases} \tag{2.10}$$

The nonlinearity in (2.10) is also shown in Fig. 2.3. It can be approximated by the following describing function [28]:

$$N_0(A,B) = -\frac{2}{\pi B}\sin^{-1}(\frac{B}{A}) + m$$
$$N_1(A,B) = -\frac{4}{\pi A}\sqrt{1-(\frac{B}{A})^2} + m \tag{2.11}$$

where m is the slope of h(x), i.e., m=1.

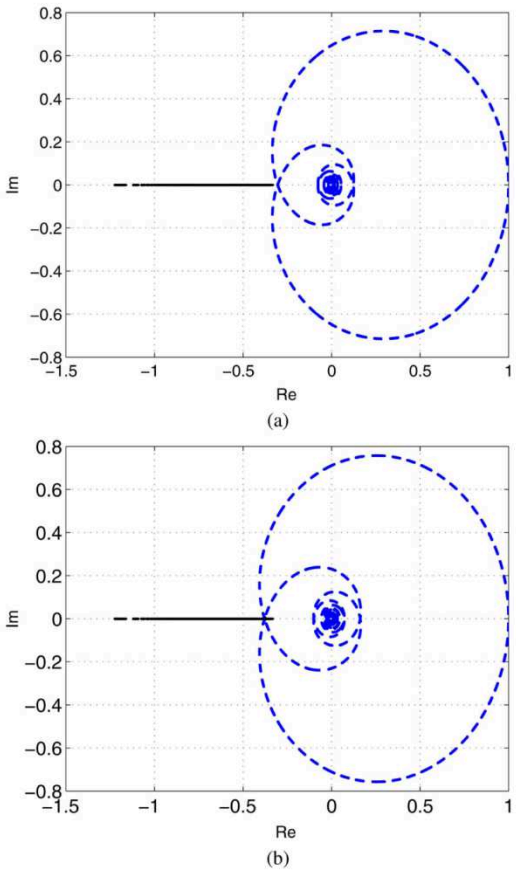

Fig. 2.5. Graphical solution of (2) for different values of τ . The continuous line refers to the function $-1/N_1(A(B),B)$, while the dotted line is the Nyquist plot of $L(jw)$ for (a) r=0.6ms, (b) r=0.8ms.

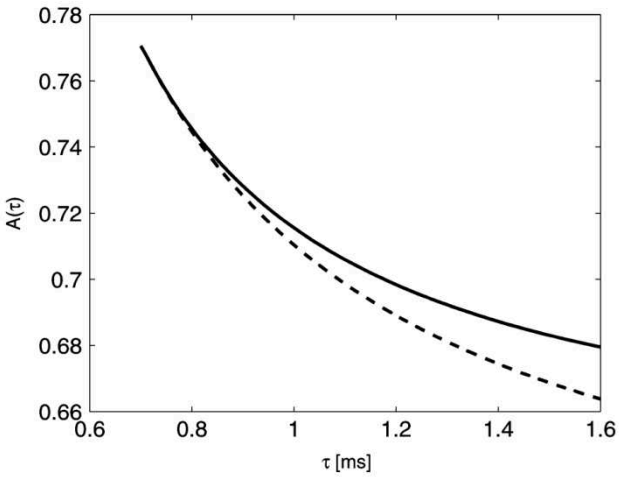

Fig. 2.6. Amplitude of the predicted limit cycle as a function of τ. The dotted curve indicates the right hand term of (2.5).

The description of system (2.1) with nonlinearity (2.10) in terms of Lur'e form is completed by including the linear part $L(s) = (ke^{-s\tau})/(s + ka)$. The conditions for the existence of chaos can be satisfied for a=1, b=3 and different values of τ. For b=3 and a=1, the system (1) with nonlinearity (10) has three equilibrium points that can be found solving the equation $x + 3h(x) = 0$, yielding to: $E_1 = -E_2 = (3/4)$, and $E_0 = 0$. We study the stability properties of these equilibrium points by considering a=1, b=3 and let τ vary. E_1 and E_2 according to criterion 2.4 are stable for $\tau \le \tau^* = 0.68ms$ and unstable otherwise. The PWL function (10) is not continuous in E_0. However, the stability of the equilibrium point E_0 can be studied by assuming a PWL tract with a large negative slope (indeed, this is the real case, since in the circuit implementation the ideal PWL function of Fig. 2.3 is realized by a comparator with a finite large negative slope). With this assumption, i.e., $b' << 0$, according to criteria 2.3 and 2.4, E_0 is neither delay-dependent stable nor delay-independent stable, and thus is unstable for all τ.

The bifurcation diagram with respect to τ is shown in Fig. 2.4. For $\tau \leq 0.68ms$, the equilibrium points E_1 and E_2 are stable, and, depending on initial conditions, the trajectory of system (2.1) with nonlinearity (10) converges either to E_1 or E_2. Indeed, for $\tau \leq 0.68ms$, (2.2) do not have a solution, and the harmonic balance method predicts that no limit cycles arise in this case. This is also evident in the Nyquist plot of $L(jw)$ for $\tau = 0.6ms$, shown in Fig. 2.5(a), that does not intersect the curve $-1/N1(A(B),B)$.

For $\tau = 0.8ms$, (2.2) predict a limit cycle (as shown in Fig. 2.5(b)) with amplitude A=0.735 and B=0.733 bias. Furthermore, this limit cycle satisfies the interaction condition (2.5), and so chaos emerges.

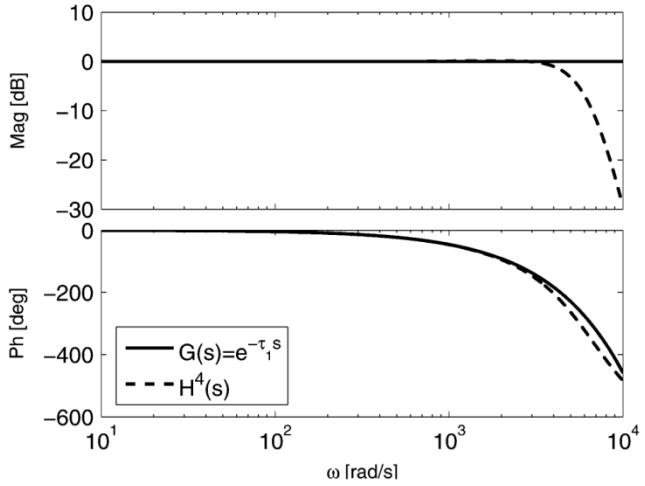

Fig. 2.7. Magnitude and phase Bode diagrams of $G_1(s)$ and $H^4(s)$.

Numerical simulations for this set of parameters confirm that the system behaves chaotically, as furtherly confirmed by the maximum Lyapunov exponent $\lambda_{\max} \cong 0.14$, calculated with the procedure discussed in [6]. It is interesting to note, that in this system when (2.2) admit a solution (for instance, for $\tau = 0.8ms$), also (2.5) is satisfied, so that chaos emerges. In Fig. 2.6 the curve $A(\tau)$ for different values of τ hand term of (2.5).

For $\tau < 0.68ms$ there is no predicted limit cycle.
For $\tau \geq 0.68ms$ a limit cycle is predicted, according to (2.2) and simultaneously the interaction condition (2.5) is satisfied (as shown by the curve $A(\tau)$ which is always above the dotted line).
Following Procedure 1, in order to implement a given timedelay $\tau 1 = 0.8ms > 0.68ms$, n=4 blocks can be used. The accuracy of the approximation is now evaluated by using two different approaches. We first evaluate the accuracy of the approximation of the delay by comparing $H^4(s)$ with the transfer function of the ideal time-delay

$$G_1(s) = e^{-s\tau_1} \tag{2.12}$$

and then we evaluate the accuracy of the approximation of the whole system in terms of the synchronization error $\delta(n)$. The Bode diagram of the ideal delay, reported in Fig. 2.7, is characterized by a unitary magnitude for any frequency, and an exponentially decaying phase. In Fig. 2.7 the Bode diagram of the transfer function $H^4(s)$ is also reported. Comparing the two frequency responses of the ideal delay $G_1(s)$ and of $H^4(s)$, both magnitude and phase show a good match in the frequency range of the circuit dynamics.
The accuracy of the approximation of the ideal model (2.1) with a system making use of a cascade of n uncertain Bessel filters is evaluated by measuring the synchronization error between the two models coupled according to (2.7). Fig. 2.8 shows that the synchronization error $\delta(n)$ as a function of n takes its minimum value for n=4 . In the inset of Fig. 2.8 $x_n(t)$ versus $x(t)$ for n=4 is shown. The analysis of Fig. 2.8 indicates that n=4 is a suitable value for the number of Bessel filters to be used. It is worth noticing that this analysis is not only based on the correspondence of the ideal time-delay value with the real one, but on the accuracy of the whole circuit in implementing the designed chaotic dynamics. The analysis was carried out assuming that the only free parameter is the number of n cascaded filters and taking into account, in the calculation of the synchronization error, the source of non-ideality deriving from the use of standard off-the-shelf components. However, the procedure can be used to tune any other parameter for which the sys-

tem is particularly sensitive, taking also into account other sources of non-ideality.

2.5. Experimental results

The circuit described in Section III has been implemented with off-the shelf discrete components. The time-delay block of the circuit has been implemented by taking into account a maximum number n=8 of filters in cascade, so that the effective time-delay introduced can be tuned and it was possible to carry out an analysis with respect to different values of waveforms have been acquired by using a NI USB6255 data acquisition board, with sampling frequency $f_s = 300kHz$.

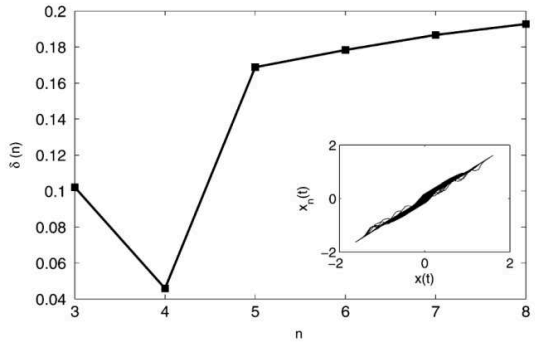

Fig. 2.8. Synchronization error $\delta(n)$ as function of n for k=1. Inset: $x_n(t)$ versus x(t) for n=4.

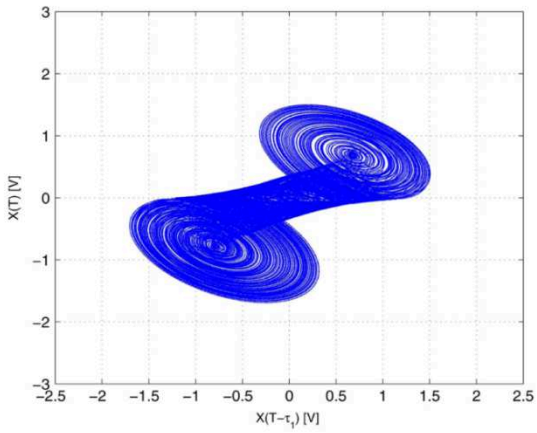

Fig. 2.9. Experimental results. Behaviour of the circuit for n=4 cascaded filters. Attractor in the phase plane X(T − τ_1)–X(T).

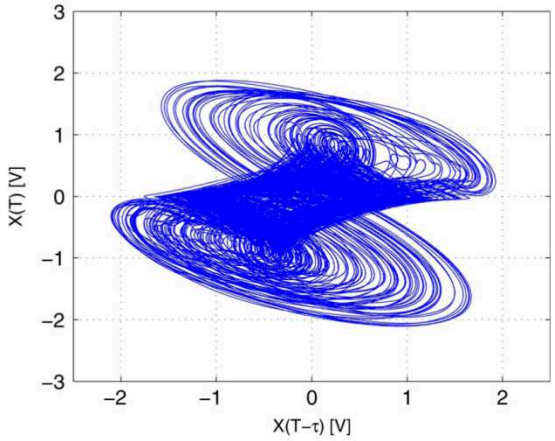

Fig. 2.10. Experimental results. Behaviour of the circuit for n=4 cascaded filters. Attractor in the phase plane X(T − τ_1)–X(T) for the following values of the parameters: a=1, b=3 and n=8.

The experimental results allow to conclude that the observed nonlinear characteristic corresponds to (2.10) in the limit of parametric tolerances of components. As concerns the time-delay block, the measured time-delay introduced by each of the filters is 0.219 ms. The difference with the theoretical prediction is also due to parametric tolerances. For the nominal values of the parameters (in particular, with n=4 Sallen-Key blocks) the circuit exhibits the expected chaotic behavior. Fig. 2.9 shows the chaotic attractor in the phase-plane $X(T-\tau_1)-X(T)$. The experimental results are in good agreement with numerical simulations. By varying the number of Sallen-Key blocks, the results of the numerical analysis discussed in Section have been confirmed by the experimental results. For n<4 a stable equilibrium point is observed. For $n \geq 4$ a chaotic behavior is obtained; an example for n=8 is shown in Fig. 2.10. The chaotic dynamics persists for the whole range of investigated, i.e., for $4 \leq n \leq 8$.

The suitability of the approach leading to a class of time-delayed chaotic circuits has been experimentally confirmed by a second case study, in which the nonlinearity is given by

$$h(x)=\begin{cases}\dfrac{2}{\pi}x & if \quad |x|<\dfrac{\pi}{2}\\ -\dfrac{2}{\pi}x-2 & if \quad x<-\dfrac{\pi}{2}\\ -\dfrac{2}{\pi}x+2 & if \quad x>\dfrac{\pi}{2}\end{cases} \tag{2.13}$$

and the other parameters are fixed as: a=1, b=5 and $\tau=1.65ms$ and ms (which corresponds to n=8 Bessel filters).

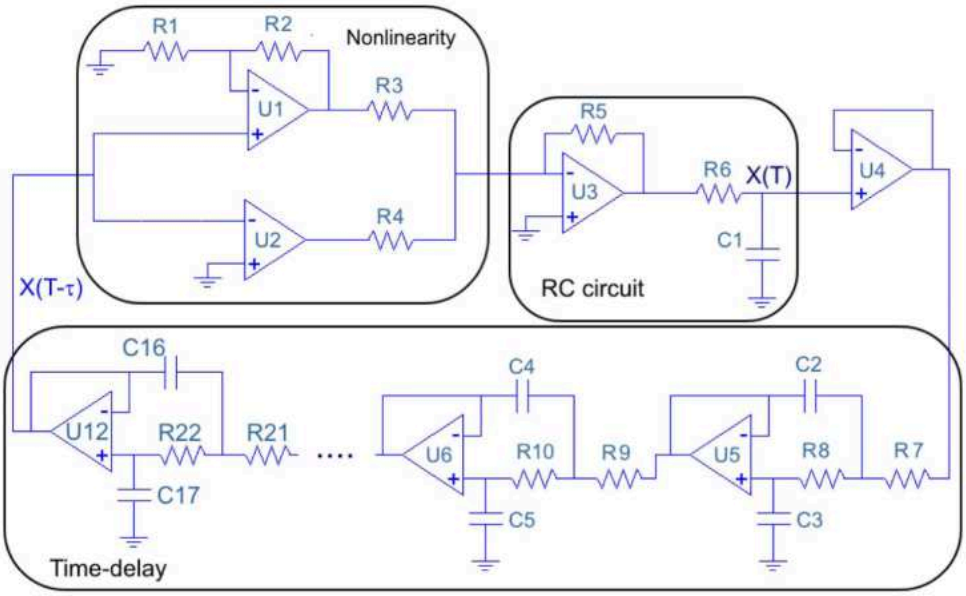

Fig. 2.11. Circuit implementing system (1) with nonlinearity (10). The following component are used: $R_1=R_6=1k\Omega$, $R_3=1.8k\Omega$, $R_4=7.85k\Omega$, $R_5=3.4k\Omega$, $R_7=R_8=...=R_{22}=10k\Omega$, $C_1=1\mu F$, $C_2=C_4=...=C_{2i}=...=C_{16}=22\mu F$, and $C_3=C_5=...=C_{2i+1}=...=C_{17}=10\mu F$, the voltage supply is $V_{sup}=\pm 9V$.

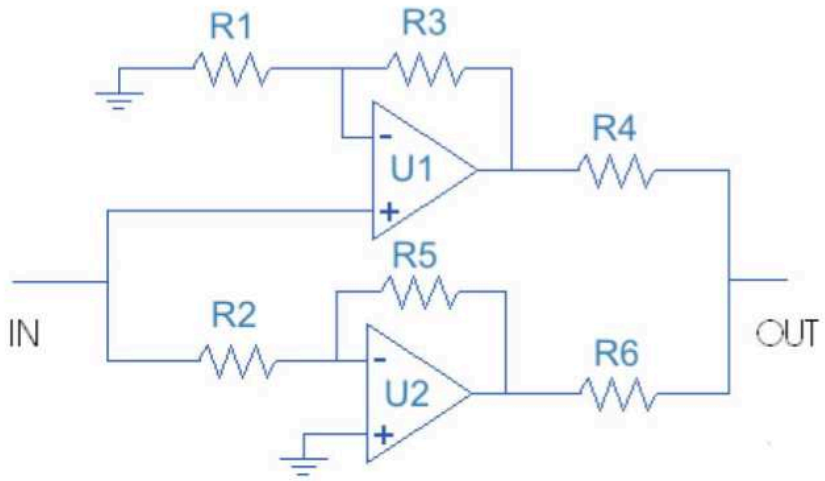

Fig. 2.12. Circuit implementing nonlinearity (13). The following component are used: $R_1 = R_2 = 1k\Omega,\ R_3 = 4.32k\Omega,\ R_4 = 4.12k\Omega,\ R_5 = 1.74k\Omega,\ R_6 = 2.74k\Omega,$ $C_1 = 1\mu F$, the voltage supply is $V_{sup}=\pm 9V$.

The implementation of this second example follows the same procedure and guidelines used for the first example discussed in section 2.6. It is worth to notice that the scenario is different in the two cases, although in both examples chaos has been experimentally observed. In both cases, the time-delay constitutes an interesting bifurcation parameter, but, while, in the first case, the behavior changes from fixed point to chaos when the number of Bessel filters is increased, in the second example small delays induce periodic oscillations, while chaotic behavior occurs for larger delays. The model described has been implemented with off-the-shelf discrete components. The time–delay block of the circuit has been implemented by taking into account a maximum number n = 12 of filters in cascade, so that the effective time–delay introduced can be tuned and it was possible to carry out an analysis with respect to different values of n.

The behavior of the circuit for the nominal values of the parameters (in particular, for n = 8) is shown in Fig. 2.13(b). For these values the circuit exhibits a chaotic dynamics as predicted by the theoretical and numerical analysis discussed above. The behavior with respect to different time–delays, obtained by varying the number of Sallen-Key cas-

caded filters has been then characterized. Different behaviors have been observed, as reported in Fig. 2.13. In particular, increasing n bifurcations from limit cycles to chaotic attractors can be observed. Other examples of the behavior with respect to different values of n are reported in Fig. 2.13.

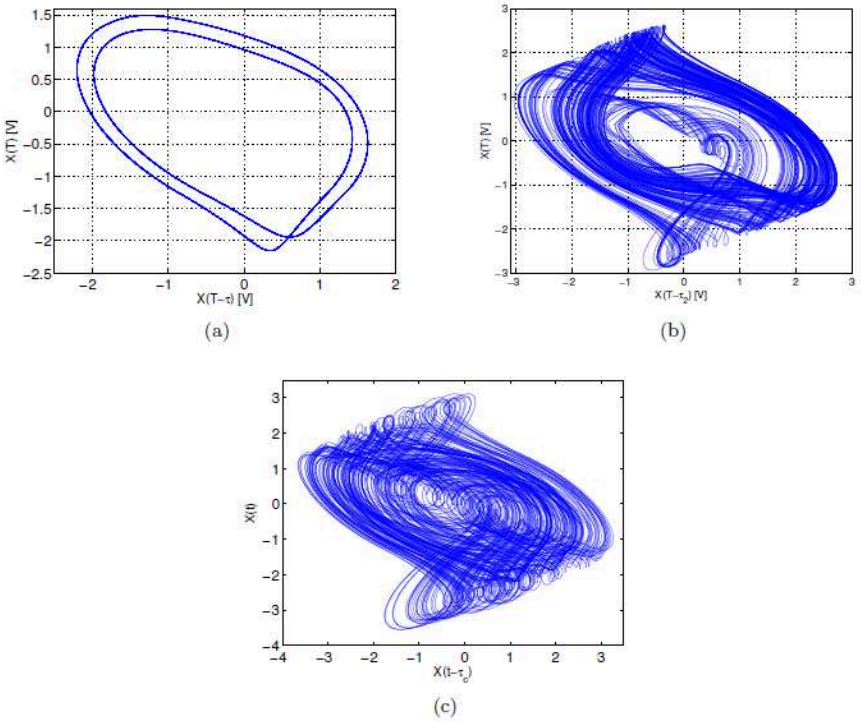

Fig. 2.13. Experimental results. Behavior of the circuit in the phase plane X(T − 1)–X(T) for the following values of the parameters: a = 1, b = 5, and (a) n = 5, (b) n = 8, (c) n = 10.

2.6. Equation and complete scheme of the time-delay chaotic circuit

The equations of the circuit implemented and the scheme are here given. The circuit implementing system (1) with nonlinearity (2.10) is shown in Fig. 2.11. The block performing the integration of the state variable is realized through OP-AMP (algebraic adder) and a RC circuit acting as an integrator. The nonlinear stage is constituted by the two OP-AMPs and . is connected in the non-inverting configuration, while is an open loop comparator. The PWL nonlinearity of (10) is obtained by

summing the output of these two operational amplifiers directly at the integrator stage. The circuit is governed by the following equation:

$$X(T) = \frac{1}{R_6 C_1}(-x(T) + \frac{R_5}{R_4} g_1 - \frac{R_5}{R_3} X(T-\tau_1)) \tag{2.14}$$

where is the output of the comparator, i.e., $g_1 = (X(T-\tau_1))/(|X(T-\tau_1)|)V_{sat}$ (V_{sat} is the saturation voltage of the operational amplifier), and τ is the time-delay realized in the circuit with n=4 Bessel filters in cascade. Equation (2.14) with choice of the components values reported in Fig. 2.11 match (1) with nonlinearity (2.10) and parameters $k = 10^3, a = 1$ and $b = 3$. Finally, in Fig. 2.12 the circuit implementing the nonlinearity (2.13) to realize the second example discussed in the text is shown.

In summary, we ca conclude that the definition of design methods for chaotic circuits is not trivial and constitutes a fundamental aspect of nonlinear circuits. In this chapter, a general scheme of time-delay continuous-time chaotic circuits and a methodology to design them have been introduced. The implementation of the time-delay block has been based on the use of a cascade of Bessel filters and a methodology for the design of the nonlinearity, of the system parameters and of has been proposed. The methodology has been then applied to two examples, which have been first theoretically and numerically analysed, and, then, implemented and experimentally investigated, confirming the suitability of the approach. Although the procedure introduced is general, the use of PWL nonlinearities simplifies the implementation stage and makes possible the implementation of the whole circuits by only using simple off-the-shelf circuital components like resistors, capacitors and operational amplifiers. A key issue of the implementation is the design of the circuitry providing the suitable timedelay needed to observe a chaotic behavior. The proposed delay circuit is a modular circuit, composed by Bessel filters in cascade, approximating an ideal delay.

A criterion to evaluate the accuracy of the approximation has been given. This criterion is based on the synchronization properties of chaotic systems: in fact, complete synchronization cannot be obtained if the circuits have different parameters, and the synchronization error can be assumed as a measure of the differences between the two circuits.

Chapter 3
SYNCHRONIZATION OF COUPLED CIRCUITS

3.1 Synchronization of Chua's circuits with diffusive coupling

Synchronization is the process through which two or more coupled circuits adjust a given property towards a common feature, thanks to a form of coupling or common external forcing.
In this chapter, the synchronization of two diffusively coupled Chua's circuit is studied from the analytical and experimental points of view. The conditions under which complete synchronization is ensured are derived by applying a strategy based on the Master Stability Function. The experimental realization, that makes use of the State-Controlled Cellular Nonlinear Network based implementation of Chua's circuit, shows the synchronized behavior of two circuits coupled with a passive resistor as diffusion coefficient. The results obtained indicates diffusive coupling as a mutually reduced order state observer, in the sense that one circuit observes the other and vice versa. Moreover, the concept of synchronization by using passive elements can be extended to spatially extended reaction–diffusion systems.
This experimental application is devoted to the synchronization of two Chua's circuits achieved by using the easier coupling possible, i.e. a simple resistor implementing a diffusion term between two corresponding statevariables. In nonlinear dynamical systems, and in particolar in chaotic systems, the case in which systems assume a common behavior is referred to as complete synchronization. Several approaches allow the emergence of synchronous behavior: negative feedback [37], sporadic driving [31], active–passive decomposition [38,41], diffusive coupling

and some other hybrid methods [36]. Moreover, synchronization can be achieved with either unidirectional or bidirectional coupling. For the sake of simplicity, let us consider the case of two coupled dynamical units: if the coupling is unidirectional, one chaotic system remains unaltered while forcing the other to follow its dynamics; if the coupling is bidirectional, both systems are influenced by the coupling itself.
This latter case can be implemented in an electronic circuit simply through a resistor connecting two corresponding state variables of the chaotic circuits. The use of diffusive coupling in Chua's circuit has been considered in [38] where it is shown that a diffusive coupling can produce the instability of fixed points, causing the emergence of chaos. Moreover, the synchronization of two Chua's circuits coupled in a bidirectional diffusive scheme has been considered in [34] where a sufficient condition for the onset of synchronization, based on the evaluation of the stability of the linearized error system, is given. Furthermore, for the case of diffusive coupling between the first state variables, synchronization is proved using this condition and confirmed by means of numerical simulations and experimental setups. However, if the diffusion operates along the other two state variables, an analytical condition for the onset of synchronization is not given. In this section, a strategy based on the Master Stability Function (MSF) is used in order to derive the analytical conditions for the occurrence of synchronization in all possible cases (i.e. scalar coupling with each of the state variables).
Experiments have been performed on a State-Controlled Cellular Nonlinear Network (SC-CNN) based implementation of two Chua's circuits. From the observation of real circuits it is possible to see that, even if in the real case the two circuits are not exactly identical, diffusive coupling does work properly and synchronization occurs. The reason to emphasize the synchronization of two Chua's circuits with a simple element like a resistor is given by a wider class of experiments that allows to prove how, in any case, one circuit is the reduced order observer of the other and therefore only one gain has to be designed. Furthermore, synchronization can be achieved without any active component in the coupling.

3.1.1. Master Stability Function based strategy

The MSF, introduced in [42], is an efficient tool that allows to evaluate the conditions under which N identical oscillators can be synchronized when coupled through a network configuration admitting an invariant synchronization manifold. The dynamics of each node can be modeled as

$$\dot{x}^i = F(x^i) - \sigma \sum_j G_{ij} H(x^j) \tag{3.1}$$

where i = 1, . . . ,N, $\dot{x}^i = F(x^i)$ represents the dynamics of each node, σ is the coupling coefficient, H : $R^N \rightarrow R^N$ the coupling function and G = $[G_{ij}]$ is a zero-row sum matrix modeling the coupling network.

Linearizing Eq. (3.1) around the synchronous state and performing a diagonalization of the resulting linear equation, a generic variational equation can be written as:

$$\dot{\varsigma} = [DF - (\sigma + i\beta)DH]\varsigma \tag{3.2}$$

where DF and DH represent the Jacobian of $F(x^i)$ and $H(x^j)$ computed around the synchronous state. Calculating the maximum conditional Lyapunov exponent Λ_{max} of Eq. (3.2) as a function of α and ß, the necessary condition for synchronization can be derived. The function $\Lambda_{max} = \Lambda_{max}(\alpha + i\beta)$ is independent of the specific network topology and is called the MSF. Hence, the stability of the synchronization manifold in a given network can be evaluated by computing the eigenvalues γh (with h = 2, . . . ,N) of the matrix G and checking if the sign of Λ_{max} at the points $\alpha + i\beta = \alpha\gamma_h$ is either negative (corresponding to a stable eigenmode) or positive (corresponding to an unstable eigenmode). If all associated eigenmodes with h = 2, . . . ,N are stable, then the synchronous state is stable at the given coupling strength σ.

When diffusion between two nodes is considered, the coupling matrix becomes $G = \begin{pmatrix} 1 & -1 \\ -1 & 1 \end{pmatrix}$, hence it has only real eigenvalues, i.e. $\gamma_1 = 0$ and $\gamma_2 = 0$. In this case, the MSF can be computed as function of α only.

The MSF approach allows to put the choice of the diffusive coupling in the framework of the design of a reduced order state observer. In fact, two diffusively coupled dynamical systems can be seen as two mutual observer systems, in which both the states are reconstructed from only one state variable from each system. Hence, the design of the observer consists in choosing one gain on the basis of the computed MSF.

The functional dependence of Λ_{max} on α can give rise to three different cases [33]. The first case (type I MSF) is the case in which Λ_{max} is posi-

tive ∀ α and, thus, the gain is able to ensure that the stability of the synchronous state does not exist. In the second case type II) above a threshold value, say σ_c, Λ_{max} assumes negative values and then this case always leads to a stable synchronous state for higher enough coupling strength, allowing the design of coupling by choosing a gain $\sigma > \sigma_c$. In the third case (type III), Λ_{max} is negative only in a closed interval of σ values: the coupling can be designed fixing a gain for which $\sigma\gamma_h$ with h = 2, . . . ,N lie in such interval.

3.1.2. Synchronization of two diffusively coupled Chua's circuits

The Chua circuit [40] is a paradigmatic circuit able to show chaotic behavior in a wide variety of different attractors, nonlinear behaviors and bifurcation scenarios, therefore the onset of synchronization in systems of coupled Chua's circuits has been often investigated.
In this paragraph, the synchronization of two diffusively coupled Chua's circuits is considered.
This task has been accounted for in [34], where a sufficient condition for the onset of synchronization is given, and numerical and experimental results are also shown. However, the derived condition is not able to prove analytically the onset of synchronization in all the considered cases.
The aim of this paper is to adopt an MSF based approach in order to assess analytically the conditions for the stability of the synchronous state, and consequently derive the diffusive gain, thus enabling to ensure the onset of synchronization. The dimensionless equations of Chua's circuit are represented by the following well-known state equations:

$$\begin{aligned} \dot{x} &= \alpha[y - h(x)] \\ \dot{y} &= x - y + z \\ \dot{z} &= \beta y \end{aligned} \tag{3.3}$$

where $h(x) = m_1 x + \frac{1}{2}(m_0 - m_1)(|x+1| - |x-1|)$.

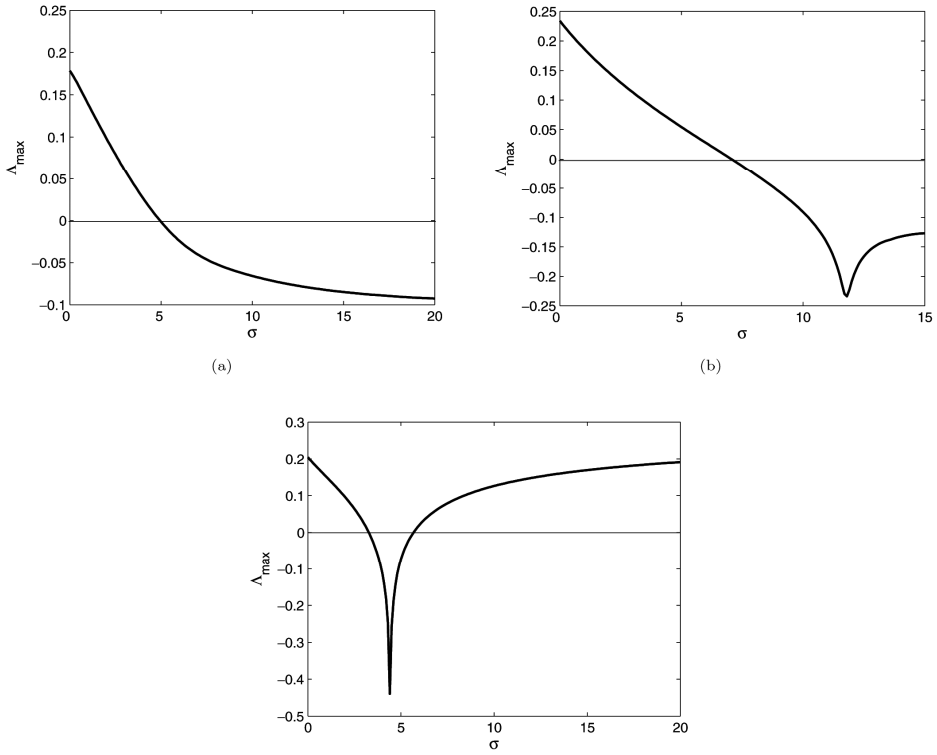

Fig. 3.1 Master Stability Function for the diffusively coupled Chua's circuits. Diffusion operates along (a) x_1 and x_2, (b) y_1 and y_2, (c) z_1 and z_2.

The two diffusively coupled Chua's circuit equation can be then written as:

$$\begin{aligned}
\dot{x}_1 &= \alpha[y_1 - h(x_1)] + \sigma\delta_x(x_2 - x_1) \\
\dot{y}_1 &= x_1 - y_1 + z_1 + \sigma\delta_y(y_2 - y_1) \\
\dot{z}_1 &= -\beta y_1 + \sigma\delta_z(z_2 - z_1) \\
\dot{x}_2 &= \alpha[y_2 - h(x_2)] + \sigma\delta_x(x_1 - x_2) \\
\dot{y}_2 &= x_2 - y_2 + z_2 + \sigma\delta_y(y_1 - y_2) \\
\dot{z}_2 &= -\beta y_2 + \sigma\delta_z(z_1 - z_2)
\end{aligned} \tag{3.4}$$

where δ_x, δ_y, and δ_z can be either one, if the two corresponding state variables are diffusively coupled, or zero otherwise. σ is the coupling coefficient, as indicated in the previous section. In Fig. 3.1, the three MSF corresponding to the cases in which only a scalar signal is used in the synchronization scheme are reported. In Fig. 3.1(a) and in Fig. 3.1(b), corresponding to the cases $\delta y = \delta z = 0$ and $\delta x = \delta z = 0$ respectively, it can be noticed that the computed MSF is type II, hence for values above a threshold, the MSF is negative and then the synchronous state is stable. Moreover, in Fig. 3.1(c), corresponding to the case $\delta x = \delta y = 0$, the MSF is type III, hence synchronization can be achieved only if the coupling strength is chosen in the negative values interval. However, being only local, the stability properties of the synchronous manifold evaluated by the MSF, in this case by means of numerical simulations only, the synchronization can actually be obtained and for specific sets of initial conditions, as describe in [34].

3.1.3. Experimental results

The circuital implementation based on the SC-CNN approach, introduced in [32], is used. Diffusive coupling is realized by the introduction of a single resistor Rc between two corresponding state variables, as reported in Fig. 3.2 The analysis performed through the MSF allows, in the first two cases, to define a lower bound for the coupling strength, and then an upper bound for the coupling resistor R_c, for the occurrence of synchronization. In particular, from Fig. 3.1(a) a value of $\sigma_c \approx 5$ can be derived for the case of diffusive coupling between x_1 and x_2. $\sigma_c x = \gamma_2$

(α R_6/R_c) > 5, hence $R_c < \gamma_2$ (α $R_6/5$) ≈ 1.25 kΩ. Moreover, starting from Fig. 3.1(b) the bound $R_c < \gamma_2$ ($R_{12}/7$) ≈ 285Ω can be obtained.

When dealing with the synchronization of nonlinear electronic circuits differences due to component tolerances should be taken into account.

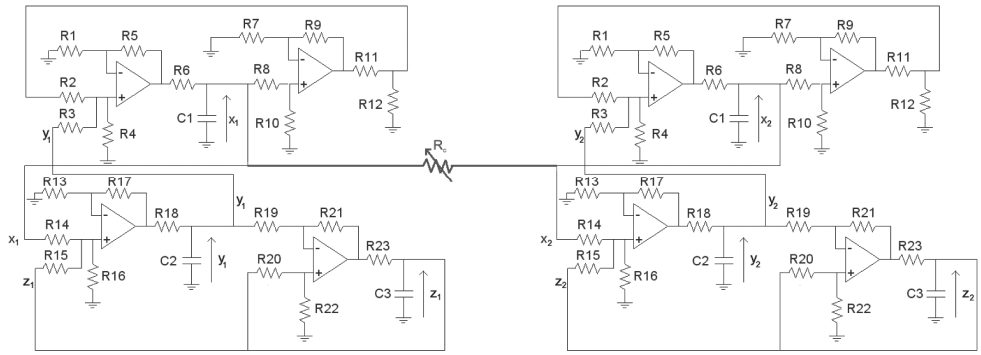

Fig. 3.2. Scheme of the diffusive coupling performed by the variable resistor Rc. The case in which diffusion is implemented between state variables x_1 and x_2 is reported.

However, diffusive coupling allows to obtain a synchronous motion as shown by oscilloscope pictures reported in Fig. 3.4.

For the case in which diffusion is performed between state variables x_1 and x_2, i.e. $\delta_y = \delta_z = 0$, the coupling is realized by resistor R_C = 330Ω corresponding to a diffusive constant $\sigma = \gamma_2 \alpha$ (R_6/R_C) = 18.98 at which the MSF has a negative value, as shown in Fig. 3.1(a). In Figs. 3.3(a) and 3.1.4(b) two pictures taken from the oscilloscope are reported showing the synchronized behavior of state variables z_1 and z_2.

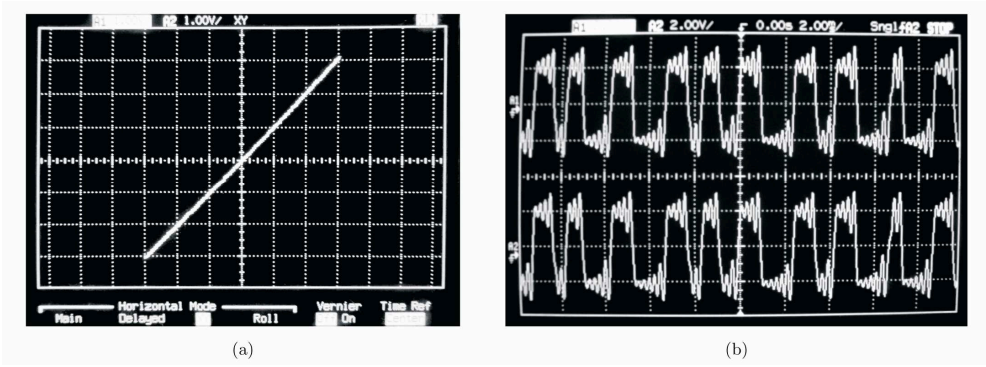

Fig. 3.3. Experimental results observed at the oscilloscope. Synchronization plot y_1 versus y_2 (a) and waveforms related to the state variables z_1 and z_2 (b) for the case in which $\delta_y = \delta_z = 0$.

Moreover, coupling the two Chua's circuits with a diffusion between the state variables y_1 and y_2, i.e. $\delta_x = \delta_z = 0$, synchronization can be obtained with a coupling resistor $R_C = 180\Omega$ implementing a diffusive constant $\sigma = \gamma_2$ (R_{12}/RC) = 11.10 which leads to a negative value of the MSF, as confirmed by the synchronized trends reported in Figs. 3.1.5(a) and 1.5(b).

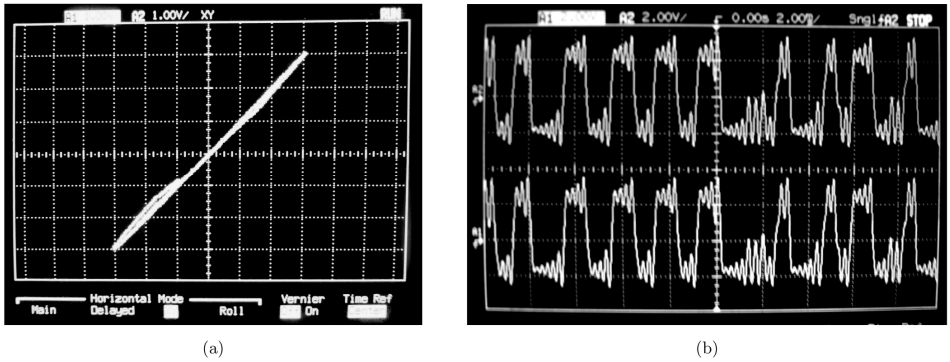

Fig. 3.4. Experimental results observed at the oscilloscope. Synchronization plot x_1 versus x_2 (a) and waveforms related to the state variables z_1 and z_2 (b) for the case in which $\delta_x = \delta_z = 0$.

In order to quantify the synchronization between the two Chua's circuits, an index based on a cross-correlation analysis has been introduced:

$$Xc = \langle x_1 * x_2, y_1 * y_2, z_1 * z_2 \rangle \tag{3.5}$$

where x_1, y_1, and z_1 are state variables of the first Chua's circuit, x_2, y_2, and z_2 are state variables of the second Chua's circuit, and the symbol * indicates the standard cross-correlation function.
In Fig. 3.5 the index Xc is reported as a function of resistor Rc that implements the coupling in the case of diffusive coupling along the state variables y_1 and y_2.
The vertical dotted line marks the upper bound identified in the previous section: as it can be noticed, below this threshold, the correlation between corresponding state variables is higher than 60%. For all the considered values of Rc the two circuits behave chaotically.

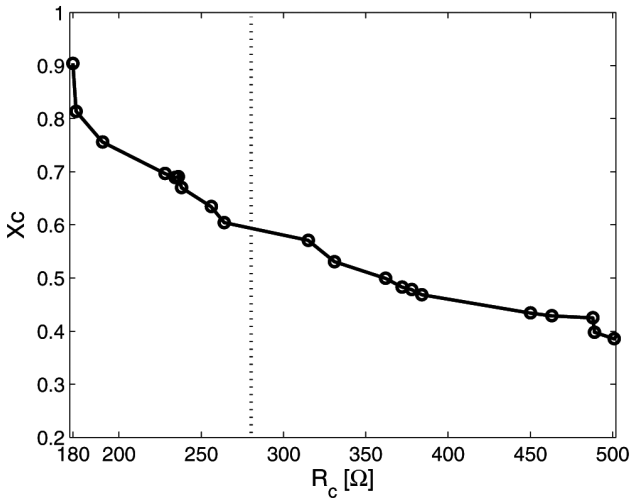

Fig. 3.5. Index X_c as a function of the coupling resistor R_c for the case of diffusion implemented between state variables y_1 and y_2. The dotted line represents the bound for the coupling resistor R_c as calculated through the MSF.

3.2 Experimental synchronization of non-identical chaotic circuits

In this paragraph, the experimental synchronization of chaotic circuits with different dynamical behavior is taken into account. Starting from both qualitative and quantitative considerations, a procedure, based on linear matrix inequalities, to assess the necessary condition for the synchronization of non-identical circuits is discussed. The results obtained

are then evaluated through an experimental approach showing the synchronization of chaotic circuits differing either in parameter values or in their dynamical equations.
Aim of this experimental application is to show experimental results on the synchronization of pairs of non-identical chaotic circuits, i.e. circuits affected by either structural or parametric differences.
The synchronization of chaotic systems affected by uncertainties has been addressed in a limited number of papers.
In particular, in [56, 51] the case of parametric mismatches between systems is considered, while in [58, 53, 59] the case of structurally different coupled circuits is investigated. More in details, in [56] the synchronization of two Lorenz systems in two different chaotic regions coupled through a master-slave negative feedback scheme [50] is achieved by using three different scalar signals to force the slave dynamics. The phase synchronized motion of a lattice of non-identical Rossler oscillators is considered in [51]. Moreover, dealing with synchronization between nonidentical dynamical systems, in [58] an active control strategy is introduced and synchronization of a Chen and a Liu system driven by a Lorenz oscillator is shown. The design procedure of a scalar controller for the synchronization of two non-identical systems is provided in [53] showing the synchronization between a Chua's circuit and a Rossler oscillator. Finally, in [59] a sliding mode controller based on Lyapunov stability theory is introduced. Furthermore, both cases of structural and parametric differences have been considered in [55] in which the analytical conditions to achieve synchronization are given considering a master-slave coupling configuration and sending three different scalar signals.
Here a strategy based on linear matrix inequalities (LMIs) for the synchronization of non-identical chaotic systems coupled through a unique scalar signal is introduced and experimental results supporting our considerations are also provided. The proposed strategy is based on the negative feedback scheme and allows the design of the slave system as an observer of the master. The basic idea arose from the evaluation of similar dynamics in two non-identical circuits: the dissipative nonautonomous oscillator introduced in [54], and the Duffing oscillator. Even if

the dynamics are different quantitative conditions can be derived to assess the possibility of achieving synchronization. In order to investigate also the case of non-identical circuits that differ only in a parameter value, the synchronization of two Chua's circuit in different chaotic regions (i.e. single-scroll and double-scroll attractors) is considered and experimental results given.

3.2.1. The LMI-based strategy for the synchronization of non-identical chaotic systems

The synchronization of chaotic systems can be achieved through a wide range of coupling schemes [44]. The attention is focused on the negative feedback scheme [50]. It consists of a master-slave coupling in which the slave is designed as an observer of the master and it is driven by a scalar error signal. The case of identical master and slave systems has been considered in several papers [52, 43, 46, 48], where different strategies for the design of the observer system are described. In particular, a strategy for the synchronization of two piece-wise linear (PWL) multiplexed systems is discussed in [43] giving the analytical conditions under which the slave system can be designed as an observer of the master. Such strategy is based on the simultaneous stabilization of the error system in each region of the PWL function in terms of a system of linear matrix inequalities (LMIs).
Let us assume that the observed system equations are:

$$\dot{X}_m = A_m X_m \tag{3.6}$$

Moreover, the observer is a dynamical system with the following equations:

$$\dot{X}_s = A_s X_s + Ke \tag{3.7}$$

where K is the vector of observer gains and $e = CX - CX_s$.

In linear systems theory the problem of the asymptotic observer can be solved by suitably choosing the vector K in order to ensure the stability of the error system:

$$\dot{e} = A_m X_m - A_s X_s - KC(X_m - X_s) \tag{3.8}$$

In the case of $A_m = A_s = A$, i.e. in the case of identical master and slave systems, the error dynamics is governed by the state matrix $A_o = A - KC$.

The stability problem of A_o can be formulated in terms of LMIs [45] by considering the well-known Lyapunov criterion in its LMI form:

$$\begin{cases} A_0{}^T P + P A_0 < 0 \\ P > 0 \end{cases} \tag{3.9}$$

where $P > 0$ ($P < 0$) indicates a positive (negative) definite matrix. Solving the LMI problem expressed by Eq.(3.9) leads to the definition of observer gains vector K.

The effectiveness of the LMI approach reveals itself when dealing with the simultaneous stability problem: a unique observer that ensures the stability of the error system for more than one observed system. At each observed system, in fact, corresponds a LMI in the system (3.9). If the resulting LMI problem is feasible, then there exists a unique gain vector K able to simultaneously stabilize all the possible error dynamics.

In this work, starting from the approach discussed in [43], an LMI-based procedure for the synchronization of non-identical chaotic systems is introduced.

The LMI approach for the simultaneous stability problem is used to obtain the synchronization conditions for chaotic PWL systems considering them as switching between different linear regions.

Furthermore, non-identical systems are considered, thus the error system has the form reported in Eq. (3.8), where A_m and A_s are the state matrices of all the possible linear regions of master and slave chaotic circuits.

Adding and subtracting the quantity $(A_s+KC)X_m$ to Eq.(3.2.3) it can be rewritten as:

$$\dot{e} = (A_s + KC)e + (A_m - A_s)X_m \tag{3.10}$$

The stability of the error system can be ensured by suitably choosing the gains vector K in order to fix negative eigenvalues for all the matrices A_{si} + KC, with A_{si} the state matrix of the i -th linear region of the PWL function in the slave system. Moreover, the error system described by Eq. (3.10) is a non-autonomous system driven by the bounded input X_m, hence the error will be also bounded.
This strategy can be applied also to systems with continuous nonlinearity since it is always possible [49] to approximate, with a given error, any continuous nonlinear function as the superposition of a finite number of PWL functions.
In the following sections, the proposed approach will be used to obtain synchronization between two non-identical systems, considering both cases of structural and parametric uncertainty.

3.2.2. Synchronization of two chaotic circuits with structural differences

This section deals with the problem of synchronizing two chaotic circuit affected by structural differences. A Duffing oscillator and a second-order nonlinear non-autonomous PWL oscillator, introduced in [54] and recently implemented and characterized in [46], have been considered. The similar fractal dimensions of their attractors (i.e. $d_{DUF} = 1.902$ and $d_{OSC} = 1.903$) calculated through the Grassberger-Procaccia algorithm [57], as well as their similar dynamical behavior reveal the closeness of the two systems and give us the idea of synchronize them.
The equations describing Duffing oscillator dynamics are the following:

$$\begin{cases} \dot{x}_m = y_m \\ \dot{y}_m = x_m - x^3{}_m - \delta y_m + \gamma \cos(wt) \end{cases} \tag{3.11}$$

while the equation of the considered nonlinear oscillator are:

$$\begin{cases} \dot{x}_s = y_s - a_1 x_s \\ \dot{y}_s = -b x_s - a_2 y_s + \sin(wt) + s(x_s) \end{cases} \tag{3.12}$$

where $s(x_s) = \frac{1}{2}(|5x_s + 1| - |5x_s - 1|)$ and $a_1 = 0.01$ and $a_2 = 0.01$ take into account the dissipative effects given by the circuital implementation.

The two systems are coupled in a negative feedback scheme, hence the equations of the coupled slave system will read as follows:

$$\begin{cases} \dot{x}_s = y_s - a_1 x_s + k_1 e \\ \dot{y}_s = -b x_s - a_2 y_s + \sin(wt) + s(x_s) + k_2 e \end{cases} \tag{3.13}$$

where $e = x_m + y_m - x_s - y_s$.

Parameter values are chosen in order to ensure that both dynamical systems show a chaotic motion, i.e. $\delta = 0.25, \gamma = 0.3, b = 1, w = 1$

The slave system in Eq. (3.13) has a PWL function s(x) that gives rise to two possible state matrices, i.e.

$$A_{s1} = \begin{bmatrix} -a_1 1 \\ -b \ -a_2 \end{bmatrix} \text{and } A_{s2} = \begin{bmatrix} -a11 \\ (-b+5) - a2 \end{bmatrix}$$

Hence, the corresponding LMI problem will be:

$$\begin{cases} {A_{s1}}^T P + P A_{s1} < 0 \\ {A_{s2}}^T P + P A_{s2} < 0 \\ P > 0 \end{cases} \tag{3.14}$$

The LMI problem in Eq. (3.14) is feasible and its solution allows to define the observer gains as $k_1 = 0.5$ and $k_2 = 20$. Two circuits implementing the dynamics reported in Eqs. (3.11) and (3.13) have been realized and waveforms generated by the circuits have been acquired by using a data acquisition board (National Instruments AT-MIO 1620E) with a sampling frequency $f_s = 200\text{kHz}$ for $T = 5\text{s}$ (i.e., 1000000 samples for each time series). Fixing the coupling gains as calculated through the LMI procedure, the onset of generalized synchronization is clearly visible in Fig. 3.6, where the trend of the state variables acquired from the two circuits are reported.

3.2.3. Synchronization of two chaotic circuits with parametric mismatches

In this section, two circuits governed by the same dinamica equations are considered. The two circuits, however, differ in a parameter value and then show different chaotic behavior.

Let us consider the well-known Chua's circuit represented by the following dynamical equations:

$$\begin{aligned} \dot{x} &= \alpha[y - h(x)] \\ \dot{y} &= x - y + z \\ \dot{z} &= -\beta y \end{aligned} \tag{3.15}$$

where $h(x) = m_1 x + \frac{1}{2}(m_0 - m_1)(|x+1| - |x-1|)$

Equations in (3.15) are able to show several dinamical behaviors, from periodic to quasi-periodic and chaotic motion depending on the selected values of parameters α and β. In particular, choosing $\alpha = 9$, $\beta = 14.286$, $m_1 = \frac{2}{7}, m_0 = -\frac{1}{7}$ the system shows the well known double-scroll attractor. Moreover, varying α Chua's circuit can evolve along different kind of chaotic attractors.
In particular, setting α = 8.6, the system dynamics evolves along a single-scroll chaotic attractor.

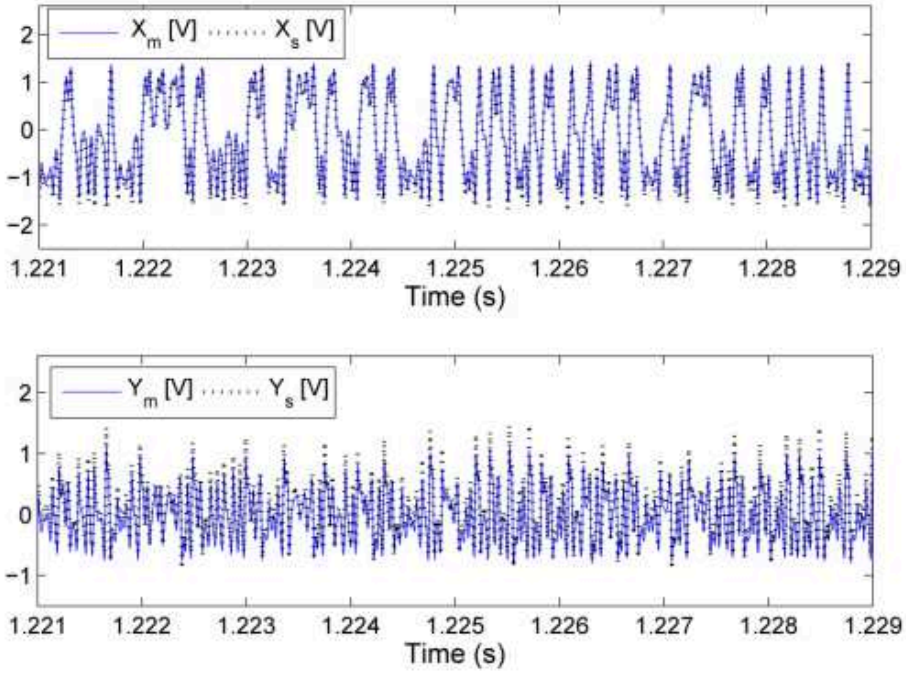

Fig. 3.6. Experimental results showing the onset of generalized synchronization between the non-autonomous PWL oscillator and the Duffing oscillator. Waveforms generated by the two coupled circuits: master system (continuous lines), slave system (dotted lines).

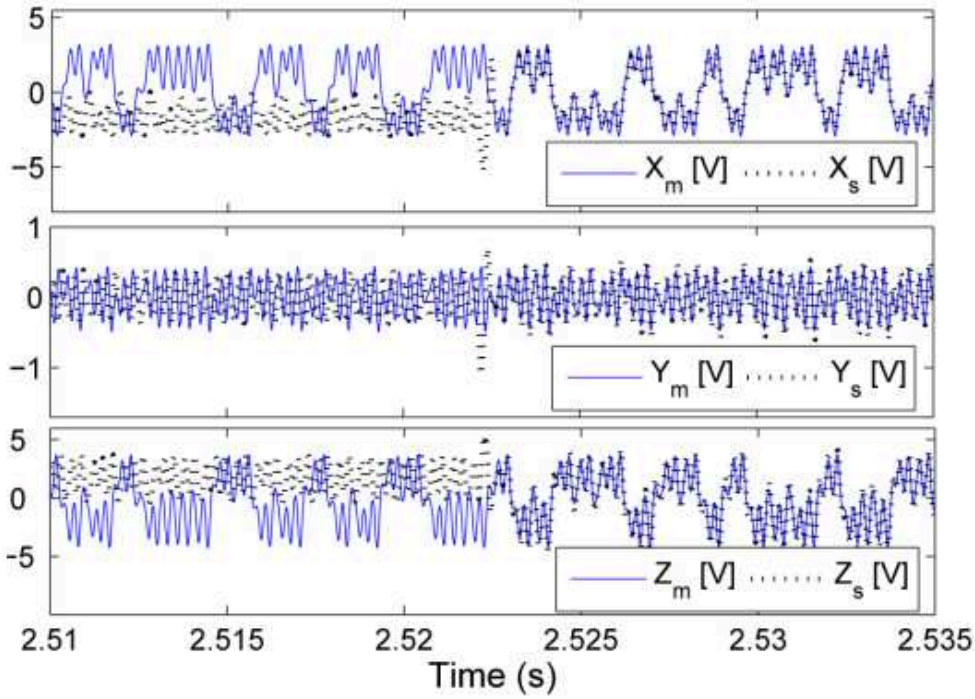

Fig. 3.7. Experimental results showing the onset of generalized synchronization between a Chua's circuit showing a single-scroll attractor and a Chua's circuit showing a double-scroll attractor. When the feedback loop is closed at T = 2.522s, the slave system state variables change their behavior. Waveforms generated by the two coupled circuits: master system (continuous lines), slave system (dotted lines).

In this section, two Chua's circuits characterized by different values of α are synchronized by coupling them through a negative feedback scheme in which master and slave equations read as follows:

$$\begin{aligned}
\dot{x}_m &= \alpha_m[y_m - h(x_m)] \\
\dot{y}_m &= x_m - y_m + z_m \\
\dot{z}_m &= -\beta y_m \\
\dot{x}_s &= \alpha_s[y_s - h(x_s)] + k_1 e \\
\dot{y}_s &= x_s - y_s + z_s + k_2 e \\
\dot{z}_s &= -\beta y_s + k_3 e
\end{aligned} \qquad 3.16$$

with $\alpha_m = 9$, $\alpha_s = 8.6$, $\beta = 14.286$, $m_1 = \frac{2}{7}, m_0 = -\frac{1}{7}$, and $e = x_m + y_m - x_s - y_s$

The values of coupling gains k_1, k_2, and k_3 are calculated applying the proposed approach. Also in this case, the three regions of the Chua's circuit PWL function corresponds to two possible linearizations, i.e.

$$A_{s1} = \begin{bmatrix} -m_1\alpha & \alpha & 0 \\ 1 & -1 & 1 \\ 0 & -\beta & 0 \end{bmatrix} \text{ and } A_{s2} = \begin{bmatrix} -m_0\alpha & \alpha & 0 \\ 1 & -1 & 1 \\ 0 & -\beta & 0 \end{bmatrix}$$

Solving the corresponding LMI problem, the observer gain can be fixed as $k_1 = -0.26$, $k_2 = 1.33$, and $k_3 = 4.51$.

In Fig. 3.9 the waveforms acquired from the two coupled circuits are reported. It can be noticed that the slave system evolves along the single-scroll attractor until the feedback loop is closed and then it is forced to follow the double-scroll dynamical behavior of the master system.

3.3 Minimum power absorbtion during synchronization

This paragraph focuses on a new aspect of the phenomenon of synchronization, emerged during a series of experiments performed in our laboratory.

In such experiments, a new qualitative finding that is of great interest for the case of two (or more) coupled circuits has been observed: the power absorbed by the system is minimum when synchronization is achieved.

The experiments refer to synchronization in electronic circuits, and, in particular, the following case studies have been taken into account: synchronization of two chaotic circuits with master-slave coupling (i.e., unidirectionally coupling); synchronization of two chaotic circuits with diffusive coupling (i.e., bidirectionally coupling); synchronization of two chaotic circuits with "qualitatively similar" dynamics; synchronization of two hyperchaotic circuits.

We refer here to the two most common types of synchronization, i.e., complete synchronization, where the systems have exactly equal state variables, and phase synchronization, where a locking of the phases is observed, while the amplitudes are highly uncorrelated.

Different coupling schemes and different dynamical circuits (Chua's circuit, Lorenz system, Rossler system, hyperchaotic circuits) have been experimentally investigated. In such experiments the power absorption of the circuits was monitored while the coupling parameters were varied. It has been observed that the minimum of the power absorbed by the system occurs exactly when the coupling parameters are such that a synchronous behavior of the circuit is obtained.

In other words the coupling parameters which guarantee synchronization are those for which the power absorption of the circuits is minimum. This observation opens the way to a new scenario on synchronization, since it highlights a relationship between the synchronous state and the minimum power absorbed by the system.

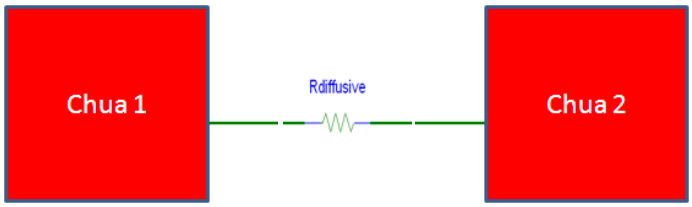

Fig.3.8 Scheme of the diffusive coupling performed by the variable resistor $R_{diffusive}$ (R_d) between state variables x_1 and x_2.

Let us first consider two Chua's circuits coupled through the first state variable in a diffusive way as in Fig.3.8. From the point of view of circuit implementation, this coupling corresponds to a resistor connecting the two capacitors associated with the two corresponding state variables. In terms of dimensionless equations, it can be described by:

$$\begin{aligned}
\dot{x}_1 &= \alpha[y_1 - h(x_1)] + k(x_2 - x_1) \\
\dot{y}_1 &= x_1 - y_1 + z_1 \\
\dot{z}_1 &= -\beta y_1 \\
\dot{x}_2 &= \alpha[y_2 - h(x_2)] + \mathrm{k}(x_1 - x_2) \\
\dot{y}_2 &= x_2 - y_2 + z_2 \\
\dot{z}_2 &= -\beta y_2
\end{aligned} \tag{3.17}$$

where $h(x) = .5(|x+1| - |x-1|)$ and x_1, y_1, z_1, x_2, y_2, z_2 represent the state variables of the first (second) circuit and k is the coupling factor which is proportional to the inverse of the coupling resistor.
This kind of diffusive coupling has been theoretically and experimentally demonstrated to guarantee synchronization if the coupling k is higher than a given threshold. System has been implemented in laboratory and the power absorption P has been measured by with respect to different values of the coupling factor.
In particular, the power absorption has been evaluated separately for each circuit, by measuring the current absorbed by each circuit and the voltage supply provided by the voltage supply generator.

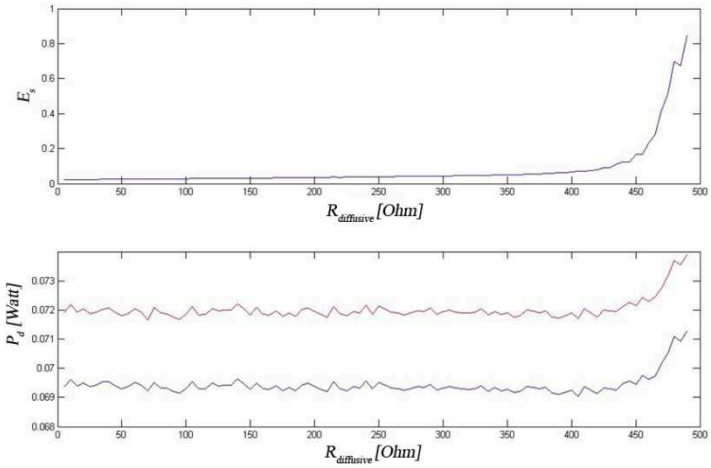

Fig. 3.9 Comparison between synchronization error Es and dissipated power in two diffusively coupled Chua's circuits with respect to different values of the coupling resistor R_d.

Fig.3.9 shows the power absorption P_d for both circuits with respect to the parameter R_d along with the synchronization error E_s, defined by

$$E_s = \sqrt{(x_1 - x_2)^2 + (y_1 - y_2)^2 + (z_1 - z_2)^2} \tag{3.18}$$

As it can be noticed, the power absorption P_d for both the two coupled systems decreases monotonically when the coupling resistor is decreased (which corresponds to increasing the coupling k in Eqs. (3.19). In correspondence, the synchronization error decreases when the coupling factor increases. The synchronization error is close to zero when the power absorption is minimum. The synchronization error is not exactly zero, because circuits are non-identical due to parametric tolerance, and for the same reason there is a slight difference in the power absorption of the two circuits.

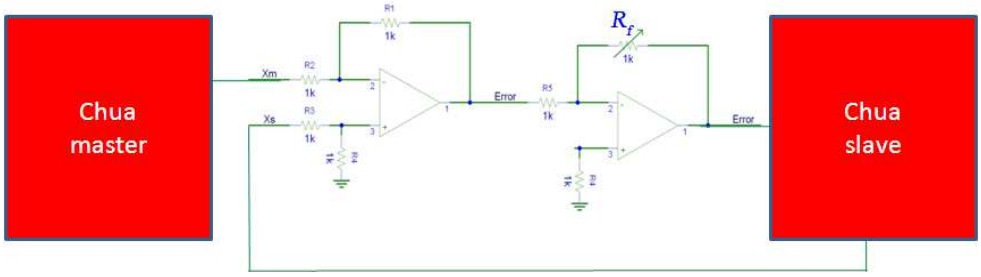

Fig.3.10 Unidirectionally coupled between two Chua's circuit.

As a second example, let us now consider unidirectional coupling between two Chua's circuit.

$$\begin{aligned}
\dot{x}_1 &= \alpha[y_1 - h(x_1)] \\
\dot{y}_1 &= x_1 - y_1 + z_1 \\
\dot{z}_1 &= -\beta y_1 \\
\dot{x}_2 &= \alpha[y_2 - h(x_2)] + \mathrm{k}(x_1 - x_2) \\
\dot{y}_2 &= x_2 - y_2 + z_2 \\
\dot{z}_2 &= -\beta y_2
\end{aligned} \tag{3.19}$$

In terms of dimensionless equations, this can be expressed as in (3.19), where circuit 1 acts as master and circuit 2 as slave.
In this case the coupling is implemented using an operational amplifier and two resistors (one of which R_f is assumed to be variable), so that the coupling factor is proportional to resistor R_f.

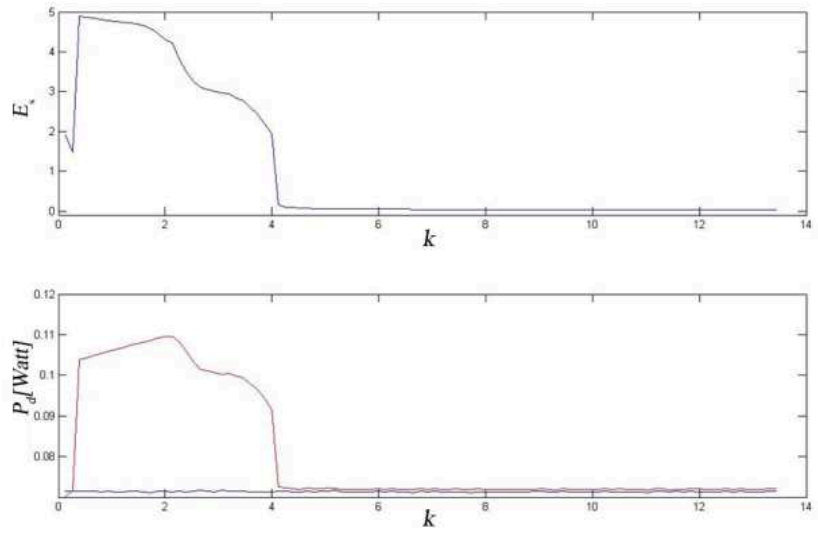

Fig.3.11 Comparison between synchronization error E_s and dissipated power in two unidirectionally coupled Chua's circuits with respect to different values of the coupling resistor R_f .

Fig.3.11 shows the dissipated power P_d for both circuits and the synchronization error E_s with respect to R_f. In this case, the two circuits do synchronize for $Rf > 1600\,\Omega$. It can be noticed that the dissipated power at the master circuit (blue line) remains constant, while the dissipated power at the slave circuit (red line) is high when the two circuits are not synchronized, until it reaches a value close to zero when the two circuits do synchronize. The same qualitative result discussed in these two examples has been observed in many other synchronization experiments and, in particular, in the following cases: two circuits implementing the Lorenz dynamics either diffusively coupled or unidirectionally coupled (negative feedback); two circuits implementing the Rössler dynamics either unidirectionally coupled (negative feedback) or coupled according to the scheme of Pecora and Carroll; two hyperchaotic circuits coupled through negative feedback; synchronization of two "qualitatively different" circuits (synchronization of a Chua's circuit in double scroll with a Chua's circuit in single scroll and synchronization of a Hartley circuit with a Colpitts circuit); synchronization of networks of dynamical circuits (a network of nodes implementing the Hopf normal form equations and a network of Chua's circuits).

Chapter 4

REMOTE SYNCHRONIZATION IN COMPLEX NETWORKS

4.1. Networks of oscillators

In thi chapter phase synchronization (PS) in a network motif with a star-like structure in which the frequency of the central node (the hub) is strongly detuned against the other peripheral nodes is investigated. We find numerically and experimentally a regime of remote synchronization (RS), where the peripheral nodes form a phase synchronized cluster, while the hub remains free with its own dynamics and serves just as a transmitter for the other nodes.

Networks of oscillatory units have been recently studied widely [60-63]. These kinds of systems serve as a modeling basis for a variety of systems from neuroscience [65], pattern recognition [65], chemistry [66], biology [67], climatology [68-70], ecology [71], social systems [72], or engineering as for instance in robot coordination [73], communication [74] and sensor networks [75], and as a general concept for understanding complex self-organizing systems. Gaining knowledge about networks of coupled dynamical systems helps understanding several phenomena, in particular synchronization, self-organization and information transfer in complex systems. Many networks found in nature have a scale-free

topology [60, 76], which is a structure where just a few nodes (the so called hubs) hold the major bulk of the links. In this work we study a typical network motif of such a hub Fig. 4.1. It is interesting to study synchronization in such a hub motif as it captures the essence of scale-free topologies.

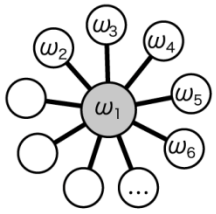

Fig.4.1 Graphic visualization of a hub network motif (star motif).

Many articles on oscillatory networks focus on a rather homogenous distribution of the nodes' parameters across the network, i.e. all nodes are either identical or just detuned within a small parameter range. This is very likely due to the possibility of an analytical treatment of the underlying equations, which becomes very complicated or even undoable if the network and thus the describing equations become too heterogenous. But the assumption of homogeneity is, in fact, not fulfilled in most realistic situations, that means it's quite unlikely to find a real system made up of several absolutely identical subsystems. Therefore, we study in this work an oscillatory network model and focus on a strong heterogeneity, precisely, the frequency of the hub is strongly detuned with respect to the peripheral nodes. We investigate phase synchronization (PS) in these motifs. Within this setup we focus on a phenomenon which we will call remote synchronization (RS), that is a situation in which two or more nodes, say n and m, which are not coupled directly, but through other nodes only, are phase synchronized, but, and this is important, the transmitter nodes, i.e. the nodes along the path from n to m are not phase synchronized with n and m, respectively.
We also investigate remote synchronization experimentally. To this aim, we designed a complex network made of coupled electronic nonlinear os-

cillators and study it with respect to different values of the coupling strength.
The experimental results obtained confirm the emergence of remote synchronization in real systems. In addition to numerical and experimental studied we give necessary conditions for the existence of RS and show that fixed amplitude systems, such as Kuramoto phase oscillators cannot generate the phenomenon.

4.2. Model and experimental setup

Since we want to focus on the mere phenomenon of synchronization, in particular PS, we chose a simple and paradigmatic model, namely the Stuart-Landau oscillator. This model is the most simple one having a harmonic limit cycle without any distortions, so we can exclude n:m synchronization in our analysis for now. We consider a network of diffusively coupled Stuart-Landau oscillators [66,77]. The equations are given by

$$u_n = (\alpha + iw_n - |u_n|2)u_n + \frac{\chi}{d_n^{in}} \sum_{m=1}^{N} g_{nm} \ (u_m - u_n) \tag{4.1}$$

where $u \in C$, α is the (Hopf) bifurcation parameter which controls how fast the trajectory will decay onto the attractor, w_n is the eigen frequency of the individual uncoupled oscillator w_n, is the overall or global coupling strength, d_n^{in} is the in-degree of node n and is used to normalize the input into node n, and (g_{nm}) is the adjacency matrix, which is symmetric, since we consider bidirectional couplings.
Now we give the values of the parameters used for the simulations in this paper. The number of nodes has been set to N = 5 in correspondence with our experimental setup, but we also verified numerically the existence of the phenomenon for higher values of N. The decay parameter is $\alpha = 1$. As mentioned in the introduction we are analyzing a hub motif (star-like network, Fig. 4.1), due to its importance as building block for scalefree networks. Node 1 is chosen to be the hub and thus n = 2…N subscripts the peripheral nodes. The adjacency matrix is given by:

$$(g_{nm}) = \begin{pmatrix} 0 & 1 & 1 & 1 & 1 \\ 1 & 0 & 0 & 0 & 0 \\ 1 & 0 & 0 & 0 & 0 \\ 1 & 0 & 0 & 0 & 0 \\ 1 & 0 & 0 & 0 & 0 \end{pmatrix}$$

The in-degrees are $\{d_n^{in}\} = \{4,1,1,1,1\}$. We chose the frequency of the hub to be $w_1 = 2.5$ in the beginning, but we will discuss the inuence of a continuous change of this value later, as well. The peripheral nodes have a similar frequency but not identical, since some repelling force is needed in order to see the transition to PS. The frequencies used in numerical simulations are $\{w_n\}_{n=2}^{5} = \{0.975,0.992,1.008,1.025\}$

For the experimental realization Eq. (4.1) must be transformed into its equivalent real form which is given by

$$\begin{aligned} \frac{d}{dt}\begin{pmatrix} x_n \\ y_n \end{pmatrix} &= \left[\begin{pmatrix} \alpha & -\omega_n \\ \omega_n & \alpha \end{pmatrix} - (x_n^2 + y_n^2)\mathbb{1}\right]\begin{pmatrix} x_n \\ y_n \end{pmatrix} \\ &\quad + \frac{\varkappa}{d_n^{\text{in}}} \sum_{m=1}^{N} g_{nm}\left[\begin{pmatrix} x_m \\ y_m \end{pmatrix} - \begin{pmatrix} x_n \\ y_n \end{pmatrix}\right]. \end{aligned} \tag{4.2}$$

The experimental setup is based on an electronic circuit mimicking the behavior of the Stuart-Landau oscillator. The circuit made of discrete components (operational amplifiers, multipliers realizing the nonlinearities of the oscillator, and a number of passive components such as resistors and capacitors) has been designed in order to obey to the same equations [Eq. (4.2)] of the Stuart- Landau oscillator, after appropriate scaling in frequency. We designed the circuit by following the guidelines reported in [94] and used for instance in [79, 96]. The values of some components of the hub and peripheral circuits are chosen in a different way so that to realize the different simulation parameters used for hub and peripheral nodes. The circuits have been then coupled in such a way that a single resistor for each node controls the value of the coupl-

ing strength in Eq. (4.2). The circuit schematic, the governing equations and the used component values are reported in Fig.4.10. An assembly of coupled electronic circuits was used to test remote synchronization in real physical systems. In this Appendix, the electronic oscillator used and the coupling circuitry between the oscillators are briey described. The circuit that was built is governed by a rescaled version of Eqs. (4.2), i.e. $\frac{d}{dt} \to \tau \frac{d}{dt}$ d, where τ is a time scaling factor $\tau = 10^{-5} s$ in our circuit). The other circuit parameters were set to the values discussed in Section II. Fig. 4.10 shows a schematic of the circuit. The values of the circuit components have been chosen in order to
match Eqs. (4.2). In particular, the relationships between the parameters α and w and the component values are given by:

$$\begin{aligned} \alpha &= \frac{R_6}{R_1} - 1 = \frac{R_{13}}{R_{10}} - 1 \\ \omega &= \frac{R_6}{R_4} = \frac{R_{13}}{R_{11}} \end{aligned} \tag{4.3}$$

Eqs. (4.3) have been used to set the component values for the hub circuit and for the peripheral nodes. The component values listed in the caption of Fig. 4.10 refer to a peripheral node. The hub components di_er from that of a peripheral node for the following resistors: $R_3 = 667\,\Omega$, $R_4 = 400\,\Omega$, $R_{11} = 1.6\mathrm{k}\,\Omega$, $R_{12} = 727\,\Omega$. Resistors with 1% tolerances and capacitors with 5% tolerances have been used.
The experimental coupled oscillator setup consisted of five circuits arranged in a star-like network. The coupling terms $\chi(x_j - x_i)$ and $\chi(y_j - y_i)$ are produced by adding the x (respectively y) signals and multiplying them for a tunable gain factor through an operation amplifier in algebraic adder configuration. The tuning of the coupling coeficient is realized by using as feedback resistor a potentiometer. The coupling terms are then added into the equations of the electronic oscillator through the operational amplifier adders U1 [term $\chi(x_j - x_i)$] and U2 [term $\chi(y_j - y_i)$].

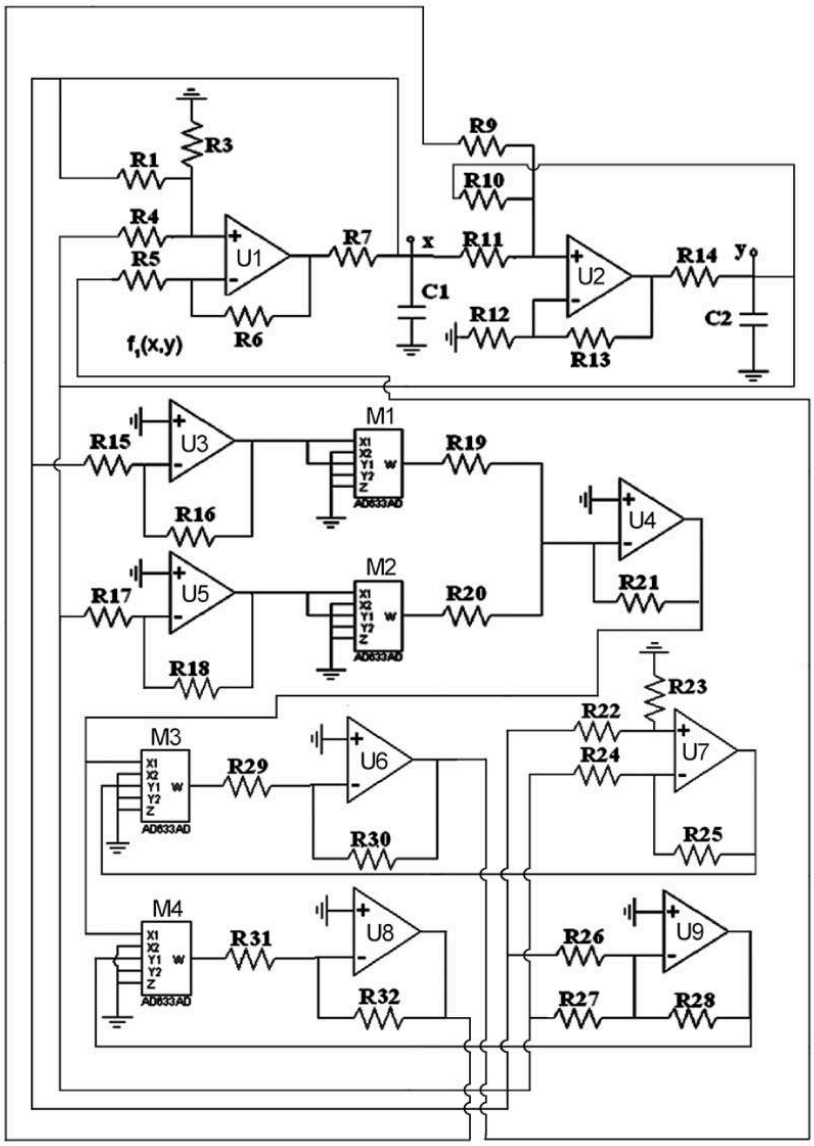

Fig 4.10. Schematic of the circuit described by Eqs. (2) (rescaled in time with τ). The component values are: R1 = 500 Ω , R3 = R4 = R5 = R6 = 1k Ω , R6 = 100 Ω , R8 = R9 = 4k, R10 = 2k Ω , R11 = 4k Ω , R12 = 1k Ω , R13 = 4k Ω , R14 = 100 Ω , R15 = 1k Ω , R16 = 7.2k Ω , R17 = 1k, R18 = 7:2k, R19 = R20 = R21 = R22 = 1k, R23 = R24 = 2k, R25 = 1k, R26 = 2k, R27 = R28 = R29 = R30 = R31 = R32 = 1k, C1 = C2 = 100nF. The operational amplifiers U1,...,U9 are all type TL084. The analog multipliers M1,...,M4 are all type AD633. Power supply is $\pm$ 9V .

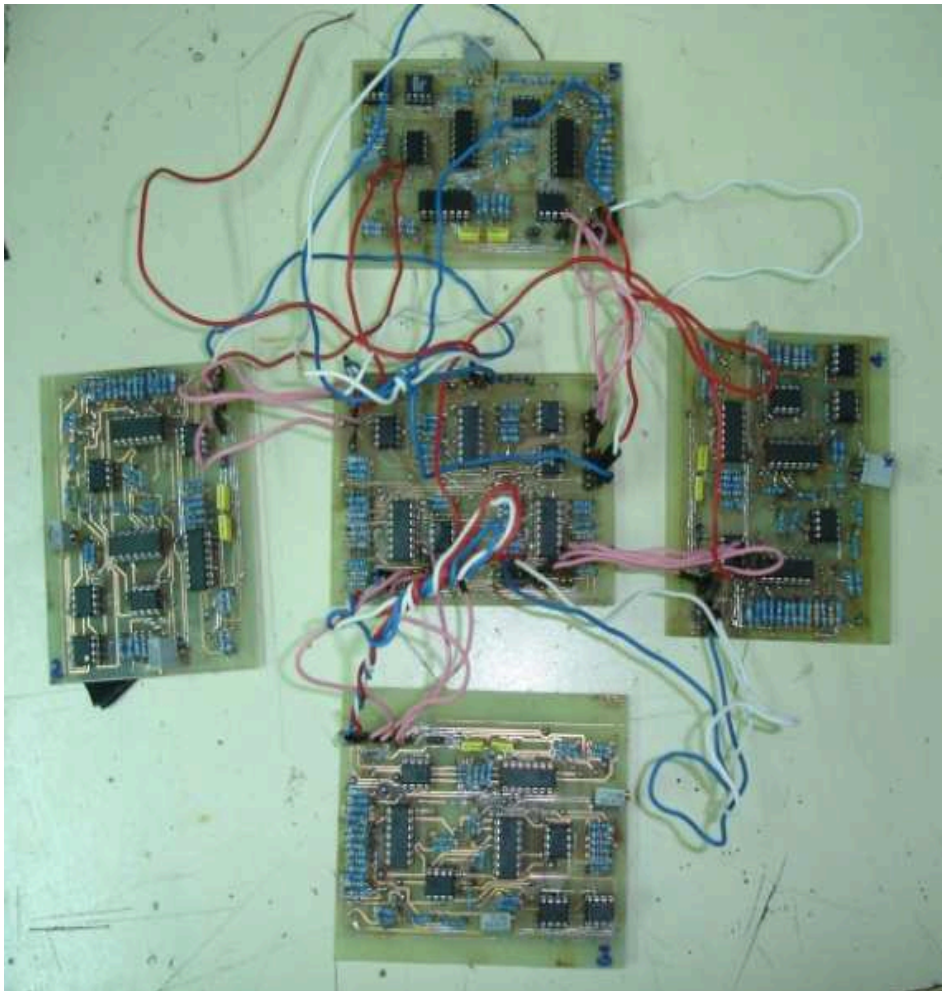

Fig 4.11. Hardware implementation of a star motif of Stuart-Landau oscillators.

Our findings shed some new light on the issue of functional versus structural topology in networks of interacting dynamical systems, which is of high importance especially in the field of neuroscience. We have shown that the measured topology via a "naïve" phase synchronization measure gives a wrong picture of the underlying network structure and explained this by a mechanism which we call remote synchronization (RS). Nodes can "speak" with each other through a transmitting nodes without synchronizing with this one, given that the transmitter has a suficiently different frequency. We verified that RS also occurs in real experiments, by designing a network of five coupled oscillators showing

the regime of RS for coupling strength values which are intermediate between the case of no synchronization and that of PS of the whole network. Therefore, not purely phase oscillators may reveal phenomena that can be experimentally observed and that purely phase models are not able to explain. We expect that the same phenomenon of RS occurs in more complex topologies as confirmed by some preliminary results including those obtained on scale-free networks as discussed above. RS can be also important with anharmonic or chaotic oscillators, where more complicated dynamics are possible. RS might also find applications in several fields, such as neuroscience, here in understanding information transmission inside the brain or help designing new more efficient artificial neural networks as described in [65]. Another application might be in climate research, in particular in understanding teleconnections (i.e long-range connections) such as between the Indian Monsoon and El Ninno/Southern Oscillation [69,70].

4.3. Emergence of remote synchronization

We start our analysis with a visual inspection of numerically integrated time series of system (4.1). Fig. 4.2 depicts the excerpts from the time series as well as the instantaneous frequencies and Lissajous-like patterns of the phases. For low coupling [Fig. 4.2(a)] we see that the nodes are interacting with each other and modulations of the phase appear, but no synchronization is visible. For a strong coupling [Fig. 4.2(c)] we find a regime of full phase synchronization with an identical amplitude of all nodes and without any modulations. The phenomenon of RS appears for intermediate values of the coupling strength [Fig. 4.2(b)]. Here we see, that all peripheral nodes become phase synchronized, while the hub remains with its own phase and frequency. In order to study this more precisely, we will introduce some measures for PS. The most common measure for PS is the Kuramoto order parameter, which is defined:

$$r_{nm} = \left| \langle e^{i[\varphi_n(t) - \varphi_m(t)]} \rangle_t \right| \tag{4.4}$$

where $\langle \cdot \rangle_t$ denotes the mean over time, and $\varphi_n(t)$ is the phase of oscillator n. For the Stuart-Landau oscillator the phase is simply given by $\varphi_n(t) = -i \log(u / |u|)$.

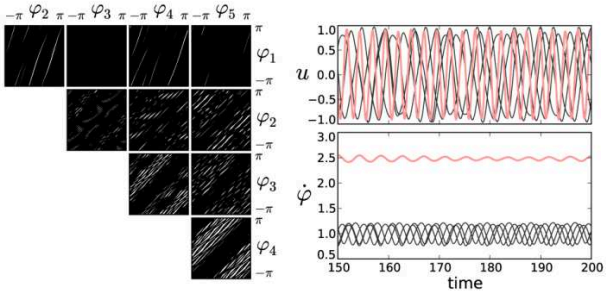

(a) Snapshots for $\varkappa = 0.2$. Here no synchronization between any nodes is visible.

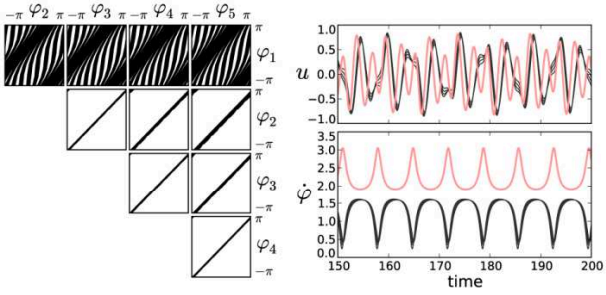

(b) Snapshots for $\varkappa = 0.6$. Here we find remote synchronization. The peripheral nodes are synchronized with each other while the hub (node 1) remains unsynchronized with the rest.

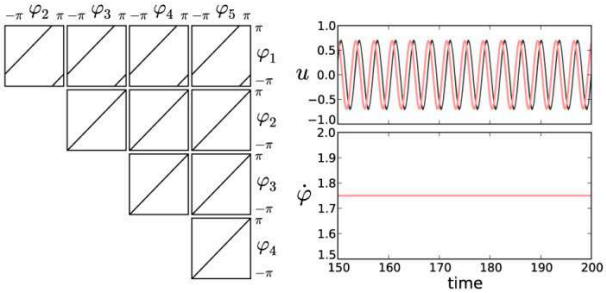

(c) Snapshots for $\varkappa = 0.8$. Regime of full phase synchronization. All nodes of the network are synchronized with each other.

Fig. 4.2 These plots illustrate the observed phenomenon of the remote synchronization. For three different values of the coupling strength χ snapshots are shown of: the time

series u(t), the instantaneous frequencies $\dot{\varphi}(t)$ and Lissajous-like figures made by plotting pairwise the phases φ_n of all oscillators against each other. The red line is the hub.

Since we are interested in the situation where the peripheral nodes form one synchronized cluster and the hub is separated from this, i.e. it forms another trivial cluster with itself, we introduce two measures accounting for that situation. For measuring the coherence of the hub with the rest of the network we define $r^{direct} = \frac{1}{N-1}\sum_{n=2}^{N} r_{1n}$. As a measure for the coherence of the peripheral cluster we define $r^{direct} = \frac{2}{(N-1)(N-2)} \sum_{n=2,m>n}^{N} r_{nm}$, i.e. the mean of the pairwise measured phase coherence among the peripheral nodes.

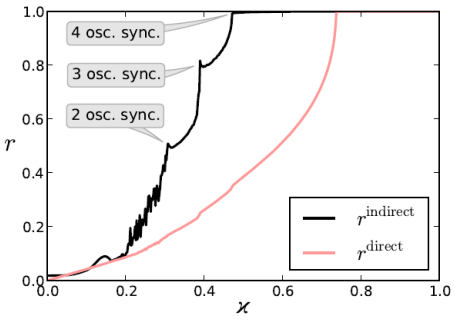

Fig. 4.3 Transition to phase synchronization for the hub motif [Fig. 4.1]. From the plot the onset of RS is clearly visible. The three annotations indicate synchronization between two, three and four peripheral oscillators,respectively.

Fig. 4.3 shows the transision to PS of both measures in dependence on the coupling strength χ. The measures have been computed from numerical integration of Eq.(4.1) with the parameter setup given in Sec. 4.2. Here it is clearly visible that the phase coherence of the peripheral nodes increases considerably faster than the synchronization of the hub with the rest. The peripheral nodes reach full PS at a value of the coupling strength χ of about 0.47, while the hub joins this cluster much later at $\chi \approx 0.74$, when it hits the global Arnold tongue of the network. In the figure we marked three steps in the curve of $r^{indirect}$. These steps cor-

respond to the onset of RS between two, three and all (four in our case) peripheral nodes of the network. These transitions are more clearly visible in Fig. 4.5(b) in which the number of synchronized clusters are shown.

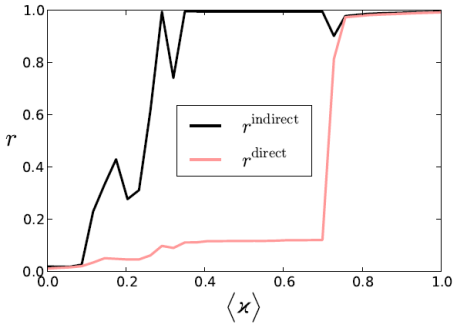

Fig.4.4 Transition to phase synchronization for the hub motif for experimentally obtained data. The regime of RS is clearly visible.

Fig. 4.4 shows the same plot for experimentally generated data. The data have been obtained by a set of experiments on the implemented network of Stuart-Landau oscillator circuits performed with respect to different values of the coupling χ, starting from χ = 1.0 and decreasing this parameter. The coupling strength is decreased by small steps and for each value of it, the state variable x_n for each circuit has been acquired with a National Instruments USB6255 acquisition board with the sampling frequency f_s = 300kHz. The phases of the oscillators have been then calculated by applying the Hilbert transform on the obtained time series and the two parameters rindirect and r^{direct} have been calculated. The result, shown in Fig. 4.4, confirms the existence of RS in real systems. It should be noted that the coupling strength is implemented in the circuit through five different components, which makes it quite difficult to obtain exactly the same value for it, taking also into account the tol erances in the whole network circuit. For this reason, in Fig. 4.4 the average value $\langle\chi\rangle$ of this parameter is reported. The scenario observed is qualitatively similar to that obtained with numerical data, and the two transitions occur at slightly different values of the parameter. It is clearly visible that there exists a quite large domain of the coupling parameter, where we have RS while the hub remains with its own dynamics. As a second analysis tool we are computing the Lyapunov spectrum (LS). Any non-trivial attractor (limit cycle, chaotic) of continuous dynamical systems has one Lyapunov exponent (LE) equal to zero, cor-

responding to the free phase of that system. Any perturbation in the direction of the system's flow will remain constant over time. In the case of an ensemble of uncoupled systems with a limit cycle or chaotic attractor, there will be as many zero LEs as there are systems included. As one couples those systems, PS will manifest itself by one or more (depending on the number of sub-systems forming the synchronized cluster) LEs becoming strictly negative due to the attractive force between the former free phases of the oscillators [97]. Hence, the number of LEs equal to zero can be used as an indirect measure for the number of phase synchronized clusters.

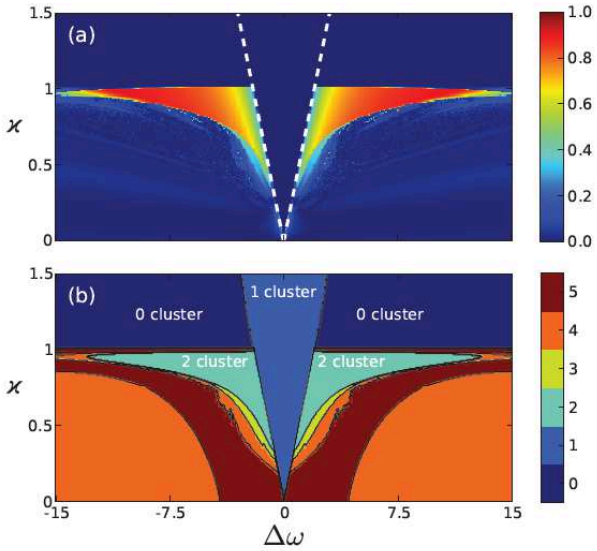

Fig.4.5 (a) shows Δr in dependence on Δw and χ, which can assume values between 0 and 1, whereby values close to 1 indicate RS (see text). The dotted line shows the analytically derived border of the Arnold tongue. The red areas to the left and right of the Arnold tongue are regimes in which RS occurs. (b) depicts the number of LEs equal to zero in dependence on Δw and χ. The 2-cluster state corresponds to the RS regime.

In order to examine this phenomenon in more detail, we also studied the clustering in dependence on the hub's frequency. In Fig. 4.5(a) we plot $\Delta r := \left| r^{direct} - r^{indirect} \right|$ in dependence on the global coupling strength χ and the frequency frequency mismatch Δw of the hub with respect to the mean frequency of the peripheral nodes: $\Delta w := w_1 - \langle w_n \rangle_{n=2}^{N}$.

In the case of RS $r^{indirect}$ will be close to 1, while r^{direct} will be rather low, say less than 0.5, so for will be large here. If we are either in a regime where we have no synchronization or full synchronization r^{direct} and $r^{indirect}$ will be about equal (either around 0 or around 1) and thus Δr will be low. Fig. 4.5(b) shows the number of LEs equal to zero for the same parameters Δw and χ. As already mentioned, this is an indirect measure for the number of synchronized clusters.
The red area in Fig. 4.5(a) corresponds to the regime where RS exists. We find the same shape in Fig. 4.5(b) with a value of 2, thus showing that we have two synchronized clusters here. Both measures are in very good agreement with each other. For coupling strengths $\chi > 1$ and outside the Arnold tongue we have oscillation death, which manifests in the Lyapunov spectrum by all LEs becoming negative, since the system has only one global stable fixpoint. In both figures we clearly see the classical V-shaped Arnold tongue of the globally synchronized state, i.e. a regime of one cluster PS.
For system (4.1), the Arnold tongue A can be computed analytically:

$$\mathcal{A} = \{(\varkappa, \{\omega_n\}_{n=1}^{N}) \mid \varkappa > \max_n |\Omega - \omega_n|\}$$

where Ω is the frequency inside the Arnold tongue, given by

$$\Omega = \frac{1}{2}\left(\omega_1 + \frac{1}{N-1}\sum_{n=2}^{N}\omega_n\right)$$

In Fig. 4.5(a) the analytically computed border of A is shown with dotted lines and agree very well with the border observed from the numerically integrated data. In the following we discuss the basic mechanism of RS and give an explanation for the necessary conditions for RS to occur robustly.

4.4. Mechanism underlying remote synchronization

Since we are interested in the mechanism of how two indirectly connected oscillators become synchronized, it is suficient to focus on three nodes only: two peripheral nodes, to which we will refer to as node 2 and node 3 (in correspondence with our initially made numbering), con-

nected indirectly via the hub (node 1). In order for node 2 and node 3 to mutually synchronize, actions of node 2 need to be transmitted to node 3 and vise versa. It means that the dynamics of node 1 have to be such that they leave the transmitted actions of node 2 and node 3 possibly unaltered. Thus, two conditions have to be fulfilled for RS to occur. Firstly, the average time scale of the attractor of node 1 should be sufficiently different from the ones of the attractors of node 2 and node 3 in order to not to synchronize with them. Furthermore, node 2 and node 3 must not be too different such that they are able to synchronize through a weak interaction. Secondly, perturbations of node 1 must not decay too fast in order to get transmitted via node 1. The decay of perturbations of the Stuart-Landau oscillator is controlled by the parameter α in Eq. (4.1). The larger α the faster a deviation from the limit cycle will "fall back" onto that. For $\alpha \to \infty$ any deviation of the amplitude will decay immediately. Thus, we expect the RS regime disappears for $\alpha \to \infty$. In this case, after a change into polar coordinates and omitting the amplitude, Eq. (4.1) can be transformed into a network of coupled Kuramoto phase oscillators [66,98]:

$$\dot{\varphi}_n = \omega_n + \frac{\varkappa}{d_n^{\text{in}}} \sum_{m=1}^{N} g_{nm} \sin(\varphi_m - \varphi_n) \tag{4.5}$$

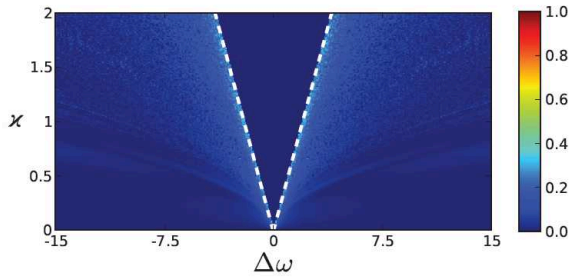

Fig 4.6. (Color online) $\Delta r(\Delta w, \chi)$ for the hub motif of Kuramoto phase oscillators [Eq.(4.5)] is shown. By comparing with Fig. 4.5(a) it can be observed that there is no RS regime, here.

We applied the analysis described in Sec. 4.3 to this network of phase oscillators using the same setup and parameters as in the Stuart-Landau case described in Sec. 4.2. Fig. 4.6 shows $\Delta r(\Delta w, \chi)$ for this system. By comparing Fig. 4.6 with Fig. 4.5(a) the absence of the RS regime for the phase oscillators is clearly visible (absence of the red areas to left

and right of the Arnold tongue which indicate RS). We have also checked that by computing Δr for different increasing values of α. In this case the disappearance of the RS can be tracked. Thus, our previously made assumption is correct, that the ability of indirectly coupled oscillators to synchronize remotely depends on a certain exibility or memory of the amplitude of the transmitting system.
Or even more crucial, it depends on the existence of a free amplitude at all. We show in fact that when amplitude perturbation is not possible, as for instance in coupled Kuramoto phase oscillators, for which a fixed not perturbable amplitude is assumed indirectly, remote synchronization does not appear!

4.5. Remote synchronization in complex networks

In this section we want to give a short outlook on RS in complex networks. We will not discuss the phenomenon in detail in this context, as it needs a lot more preparation and advanced statistical methods for a detailed analys, since far more complex synchronization scenario are possible. However, one is able to find RS in more complex and asymmetric networks as well. For our demonstration we generated a network consisting of 100 nodes using the Barabasi-Albert algorithm [92].
Fig.4.7 illustrates the scenario of remote synchronization in this exemplary complex network. The parameters used for this simulation have been: $\chi = 0.21$ and $\alpha = 0.2$. The frequencies of all nodes have been drawn randomly from a uniform distribution on small interval of size 0.1 centered at 3.5 for the hubs and 1.0 for the remaining nodes. The plot shows overlaid the actual (physical) network topology as it has been generated. The thick transparent lines depict synchronized nodes. Two nodes n and m have been declared phase synchronized if their PS index is $r_{nm} > 0.95$. The different coloring have been chosen to guide the readers eye. Gray coloring indicates synchronization between peripheral (non-hub) nodes while red color shows synchronization between two hub-nodes. In this chosen situation many remotely synchronized clusters can be spotted, visual by many gray lines spanning across the network. Some of those clusters even spread across long distances with several hub nodes lying in between which are not synchronized with the former. Further the hub nodes connecting the remotely synchronized clusters are synchronized itself into a cluster. This is especially interesting since the topology one would infer from analyzing the synchroniza-

tion state of the network does not reect even closely the physical connectivity of the nodes.

4.6. Hidden information transfer

Finally we want to stress another important point. From our study we conclude that in the analysis of complex heterogeneous systems the choice of an appropriate correlation or information measure becomes more important We demonstrate this with an example.

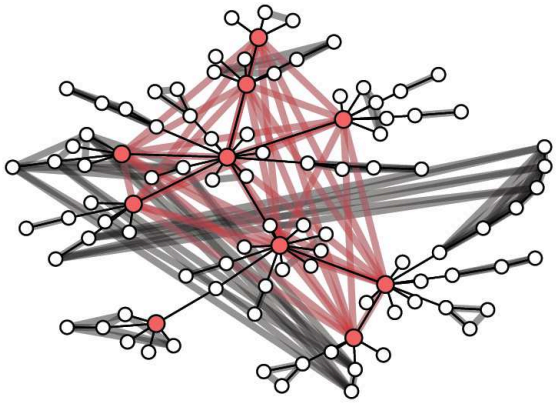

Fig 4.7. (Color online) Graphical representation of remote synchronization scenario in a scale-free network consisting of 100 nodes. Nodes with _ve or more links have been declared as hub and are colored red. The hubs have a mean frequency of 3 while the remaining nodes have a mean frequency of 1. For each pair of nodes n and m a thick transparent line has been drawn if $r_{nm} > 0.95$, i.e if both nodes can be assumed to be phase synchronized with respect to the PS order parameter r. Gray lines have been drawn between peripheral nodes and red lines between hubs. See text for more details.

Chapter 5
CONCLUSIONS

In this thesis the study of chaos has been dealt with from an experimental point of view. Different topics have been investigated, starting from the issues connected to the appearance of chaos in electronic nonlinear circuits to the dynamics emerging in coupled circuits. First of all, practical guidelines to implement a nonlinear electronic circuit with given governing equations have been discussed. The procedure allows to obtain low-cost, easy-to-realize circuits which behave in a way equivalent to that of the original mathematical model, but permit an experimental analysis. Following this procedure, a gallery of different chaotic circuits has been discussed with the aim of also providing a reference for the realization of experiments with chaos. Designing chaotic circuits is faced in literature with a variety of approaches. It is a topic of fundamental importance, which in our case has been dealt with by proposing a simple Lur'e feedback scheme with a time-delay element and deriving semi-analytical conditions for the emergence of chaos. In this way, a new class of chaotic circuits has been introduced with the unique feature of being based on a procedure which is strictly connected to the hardware steps needed to implement the circuit. Two different examples have been provided to demonstrate the suitability of the approach.
We have then examined the case of two or more coupled units. In particular, the experimental study of synchronization in two different dynamical circuits has revealed that the power absorption of the system varies as a function of the coupling parameter and a minimum is achieved when the synchronous state is reached. This phenomenon has been characterized in many coupled identical and non-identical circuits and is of fundamental theoretical and applicative importance. In fact,

from a theoretical point of view the same concept may be at the basis of many natural and social phenomena of synchronization observed in natural and social systems, while, from a practical point of view, this idea can be exploited to design systems which automatically self-organize towards the synchronized state or to implement simple measurement systems for phase synchronization. The last topic dealt with the thesis has been the study of networks of coupled oscillators. A new phenomenon referred to as remote synchronization has been observed both numerically and experimentally. According to this phenomenon, in networks with given topologies (such as the star-like one) regimes in which two not directly connected nodes do synchronize thanks to an intermediate node which guarantees the information exchange needed for synchronization, but remains not synchronized. This phenomenon can also have interesting implications in climatology, brain dynamics, communications, which need to be further explored.

A common perspective has guided the research activity carried out: the experimental approach. In fact, it has been provided a gallery of circuits to be realized and used in lab experiments on chaos. All of these circuits do not require high implementation costs, but on the contrary have been often realized by using low-cost components or even recycled components. In fact, in many cases, old disused electronic boards can be a source for all the components for implementing a chaotic circuit, so that "green" chaotic circuits can be realized. Moreover, only thanks to this experimental approach, specific studies such as the analysis of the power absorption and the investigation of real parameter mismatches between coupled circuits can be performed. The use of real circuits with real mismatches was fundamental to discover the property that synchronization is related to a condition of minimum power absorption.

References

[1] Y. Xia, M. Fu, and P. Shi, “Analysis and synthesis of dynamical systems with time-delays,” in Lecture Notes in Control and Information Sciences. New York: Springer, 2009.

[2] K. Ikeda and K. Matsumoto, “High-dimensional chaotic behavior in systems with time-delayed feedback,” Physica D, vol. 29, pp. 223–235, 1987.

[3] M. W. Lee, L. Larger, and J. P. Goedgebuer, “Transmission system using chaotic delays between light waves,” IEEE J. Quantum Electron., vol. 39, pp. 931–935, 2003.

[4] D. Ghosh, A. R. Chowdhury, and P. Saha, “Multiple delay Rössler system Bifurcation and chaos control,” Chaos, Solit. Fractals, vol. 35, pp. 472–485, 2008.

[5] W. Wischert, A. Wunderlin, and A. Pelster, “Delay-induced instabilities in nonlinear feedback systems,” Phys. Rev. E, vol. 49, pp. 203–219, 1994.

[6] J. C. Sprott, “A simple chaotic delay differential equation,” Phys. Lett.A, vol. 366, pp. 397–402, 2007.

[7] M. C. Mackey and L. Glass, “Oscillation and chaos in physiological control system,” Science, vol. 197, pp. 287–289, 1977.

[8] C. Sun, Y. Lin, and M. Han, “Stability and Hopf bifurcation for an epidemic disease model with delay,” Chaos, Solitons and Fractals, vol. 30, pp. 204–216, 2006.

[9] M. Dhamala, V. K. Jirsa, and M. Ding, “Enhancement of neural synchrony by time delay,” Phys. Rev. Lett., vol. 92, p. 074104, 2004.

[10] K. Pyragas, “Continuous control of chaos by self-controlling feedback,” Phys. Lett. A, vol. 170, pp. 421–428, 1992.

[11] E. Ott, C. Grebogi, and J. A. Yorke, “Controlling chaos,” Phys. Rev. Lett., vol. 64, pp. 1196–1199, 1990.

[12] K. Pyragas and A. Tamaˇseviˇcius, “Experimental control of chaos by delayed self-controlling feedback,” Phys. Lett. A, vol. 180, pp. 99–102, 1993.

[13] A. Namaj¯unas, K. Pyragas, and A. Tamaˇseviˇcius, “An electronic analog of the Mackey-Glass system,” Phys. Lett. A, vol. 201, pp. 42–46, 1995.

[14] X. Zhang, Z. Cui, and Y. Zhu, “Synchronization and circuit experiment simulation of chaotic time-delay systems,” in Proc. 2009 Pacific-Asia Conf. Circuits, Commun. Syst., 2009, pp. 781–784.

[15] K. Srinivasan, D. V. Senthilkumar, K. Murali, M. Lakshmanan, and J. Kurths, “Synchronization transitions in coupled time-delay electronic circuits with a threshold nonlinearity,” 2010, arXiv:1008.3300v1.

[16] K. Srinivasan, I. Raja Mohamed, K. Murali, M. Lakshmanan, and S. Sinha, “Design of time delayed chaotic circuit with threshold controller,” Int. J. Bifurcation Chaos, vol. 20, no. 7, pp. 2185–2191, 2010.

[17] W. D. Guo, G. H. Shiue, C. M. Lin, and R. B. Wu, “Comparisons between serpentine and flat spiral delay lines on transient reflection/transmission waveforms and eye diagrams,” IEEE Trans. Microw. Theory Tech., vol. 54, pp. 1379–1387, 2006.

[18] B. Andò and S. Graziani, Stochastic Resonance: Theory and Applications. Norwell, MA: Kluwer, 2000.

[19] L. Fortuna, M. Frasca, and A. Rizzo, “Chaotic pulse position modulation to improve the efficiency of sonar sensors,” IEEE Trans. Instr.Meas., vol. 52, no. 6, pp. 1809–1814, 2003.

[20] A. Buscarino, L. Fortuna, M. Frasca, and G. Muscato, “Chaos does help motion control,” Int. J. Bifurcation Chaos, vol. 17, no. 10, pp. 3577–3581, 2007.

[21] L. Fortuna, M. Frasca, and M. G. Xibilia, Chua’s Circuit Implementations: Yesterday, Today, Tomorrow. Singapore: World Scientific, 2009.

[22] M. Bucolo, L. Fortuna, M. Frasca, and M. G. Xibilia, “A generalized Chua cell for realizing any continuous n-segment piecewise-linear function,” Int. J. Bif. Chaos, vol. 11, pp. 2517–2527, 2001.

[23] R. Genesio and A. Tesi, “Harmonic balance methods for the analysis of chaotic dynamics in nonlinear systems,” Automatica, vol. 28, pp. 531–548, 1992.

[24] S.-I. Niculescu, E. I. Verriest, L. Dugard, and J.-M. Dion, “Stability and robust stability of time-delay systems: A guided tour,” in Stability and Control of Time-delay Systems, L. Dugard and E. I. Verriest, Eds. New York: Springer, 1998, pp. 1–71, Lecture Notes in Control and Information Sciences 228. [25] D. P. Atherton, Nonlinear Control Engineering. Wokingham, UK: Van Nostrand Reinhold Co. Ltd., 1982.

[26] J. J. E. Slotine and W. Li, Applied Nonlinear Control. London, U.K.: Prentice-Hall International Editions, 1991.

[27] G. Daryanani, Principles of Active Network Synthesis and Design. , Singapore: John Wiley & sons, 1976.

[28] A. Gelb and W. E. V. Velde, Multiple-Input Describing Functions and Nonlinear System Design. New York: McGraw-Hill, 1968.

[29] T. Kapitaniak, "Synchronization of chaos using continuous control," Phys. Rev. E, vol. 50, pp. 1642–1644, 1994.

[30] A. S. Sedra and K. C. Smith, Microelectronic Circuits. Oxford, U.K.: Oxford Univ. Press, 2003.

[31] Amritkar, R. E. & Gupte, N. [1993] "Synchronization of chaotic orbits: The effect of a finite time step," Phys. Rev. E 47, 3889–3895.

[32] Arena, P., Baglio, S., Fortuna, L. & Manganaro, G. [1995] "Chua's circuit can be generated by CNN cells," IEEE Trans. Circ.Sys.-I 42, 123–125.

[33] Boccaletti, S., Latora, V., Moreno, Y., Chavez, M. & Hwang, D. U. [2006] "Complex networks: Structure and dynamics," Phys. Rep. 424, 175.

[34] Chua, L., Itoh, M., Kocarev, L. & Eckert, K. [1993] "Chaos synchronization in Chua's circuit," in Chua's Circuit: A Paradigm for Chaos, ed. Madan, R. (World Scientific, Singapore), pp. 309–324.

[35] Fortuna, L., Frasca, M. & Xibilia, M. G. [2009] Chua's Circuit Implementations. Yesterday, Today and Tomorrow, World Scientific Series on Nonlinear Science, Series A, Vol. 65 (World Scientific, Singapore).

[36]Guemez, J. & Matias, M. A. [1995] "Modified method for synchronizing and cascading chaotic systems," Phys. Rev. E 52, R2145–R2148.

[37] Kapitaniak, T. [1994] "Synchronization of chaos using continuous control," Phys. Rev. E 50, 1642–1644.

[38]Kocarev, L. & Janji´c, P. A. [1995] "On Turing instability in two diffusively coupled systems," IEEE Trans. Circuits Syst.-I 42, 779–784.

[39] Kocarev, L. & Parlitz, U. 1995 "General approach for chaotic synchronization with applications to communication," Phys.Rev.Lett.74,5028–5031.

[40] Madan, R. [1993] Chua's Circuit: A Paradigm for Chaos, World Scientific Series on Nonlinear Science, Series B, Vol. 1 (Singapore).

[41] Parlitz, U., Kocarev, L., Stojanovski, T. & Preckel, H. [1996] "Encoding messages using chaotic synchronization," Phys. Rev. E 53, 4351–4361.

[42] Pecora, L. M. & Carroll, T. L. [1998] "Master stability functions for synchronized coupled systems," Phys. Rev. Lett. 80, 2109–2112.

[43] Arena, P., Buscarino, A., Fortuna, L., and Frasca, M. (2006). Separation and synchronization of piecewise linear chaotic systems. Phys. Rev. E, 74, 026212.

[44] Boccaletti, S., Kurths, J., G., G.O., Vallardes, D.L., and Zhou, C.S. (2002). The synchronization of chaotic systems. Phys. Rep., 366, 1–101.

[45] Boyd, S., Ghaoui, L.E., Feron, E., and Balakrishnan, V. (1994). Linear Matrix Inequalities in System and Control Theory. SIAM Books.

[46] Buscarino, A., Fortuna, L., and Frasca, M. (2007). Separation and synchronization of chaotic signals by optimization. Phys. Rev. E, 75, 016215.

[47] Buscarino, A., Fortuna, L., and Frasca, M. (in press). A new cnn-based chaotic circuit: experimental results. Int.J. Bif. Chaos.

[48] Fortuna, L. and Frasca, M. (2007). Experimental synchronization of single-transistor-based chaotic circuits. Chaos, 17, 043118.

[49] Fortuna, L., Rizzo, A., and Xibilia, M.G. (2003). Modeling complex dynamics via extended pwl-based cnns. Int. J. Bif. Chaos, 13, 3273–3286.

[50] Kapitaniak, T. (1994). Synchronization of chaos using continuous control. Phys. Rev. E, 50, 1642–1644.

[51] Osipov, G., Pikovsky, A., Rosenblum, M., and Kurths, J. (1997). Phase synchronization effects in a lattice of nonidentical rossler oscillators. Phys. Rev. E, 55, 2353– 2361.

[52] Pecora, L.M. and Carroll, T.L. (1990). Synchronization in chaotic systems. Phys. Rev. Lett., 61, 821–824.

[53] Ping, Z. and Yu-Xia, C. (2007). Realization of generalized synchronization between different chaotic systems via scalar controller. Chinese Phys, 16, 2903–2907.

[54] Pokrovskii, A., Rasskazov, O., and Visetti, D. (2007). Homoclinic trajectories and chaotic behaviour in a piecewise linear oscillator. Discrete Cont Dyn-B, 8, 943–970.

[55] Sarasola, C., Torrealda, F.J., D'Anjou, A., Moujahid, A., and na, M.G. (2003). Feedback synchronization of choatic systems. Int. J. Bif. Ch., 13, 177–191.

[56] Stefanski, A., Kapitaniak, T., and Brindley, J. (1996). Dynamics of coupled lorenz systems and its geophysical implications. Physica D, 98, 594–598.

[57]Strogatz, S.H. (1994). Nonlinear dynamics and chaos: with applications to physics, biology, chemistry and engineering. Perseus Books, Reading, Massachusetts.

[58]Yassen, M. (2005). Chaos synchronization between two different chaotic systems using active control. Chaos,Solitons and Fractals, 23, 131–140.

[59]Yau, H. and Yan, J. (2008). Chaos synchronization of different chaotic systems subjected to input nonlinearity. Applied Mathematics and Computation, 197, 775–788.

[60] S. Boccaletti, V. Latorab, Y. Morenod, M. Chavezf, D.- U. Hwanga, Complex networks: Structure and dynamics, Phys. Rep., 424, 175308, 2006.

[61] A. Arenas, A. Diaz-Guilera, J. Kurths, Y. Moreno, C. Zhou, Synchronization in complex networks, Phys. Rep., 469, 93, 2008

[62] G. V. Osipov, J. Kurths, C. Zhou, Synchronization in Oscillatory etworks, Springer-Verlag Berlin, 2007.

[63] S. Gil, A. S. Mikhailov, Networks on the edge of chaos: Global feedback control of turbulence in oscillator networks , Phys. Rev. E, 79, 026219, 2009.

[64] E. M. Izhikevich, Dynamical Systems in Neuroscience: The Geometry of Excitability and Bursting, MIT Press, 2006.

[65] F. C. Hoppensteadt, E. M. Izhikevich, Oscillatory Neurocomputers with Dynamic Connectivity, Phys. Rev. Lett.,
82, 14, 1999.

[66] Y. Kuramoto, Chemical Oscillations, Waves, and Turbulence , Springer-Verlag Berlin Heidelberg, 1984.

[67] E. Ullner, A. Koseska, J. Kurths, E. Volkov, H. Kantz, J. Garca-Ojalvo, Multistability of synthetic genetic networks with repressive cell-to-cell communication, Phys. Rev. E, 78, 031904, 2008.

[68] J.F. Donges, Y. Zou, N. Marwan, and J. Kurths, Complex networks in climate dynamics, Eur. Phys. J. Special Topics, 174, 157179, 2009.

[69] J. F. Donges, Y. Zou, N. Marwan and J. Kurths, The backbone of the climate network, EPL, 87, 48007, 2009.

[70] D. Maraun, J. Kurths, Epochs of phase coherence between El Ni~no/Southern Oscillation and Indian monsoon, Geophys. Res. Lett., 32, L15709, 2005.

[71] D. He, L. Stone, Spatio-temporal synchronization of recurrent epidemics, Proc. R. Soc. Lond. B 270, 15191526, 2003.

[72] S. Gil, D. H. Zanette, Coevolution of agents and networks: opinion spreading and community disconnection, Phys. Lett. A 356, 8995, 2006.

[73] A. Buscarino, C. Camerano, L. Fortuna, M. Frasca, Chaotic Mimic Robots, Phil. Trans. R. Soc. A, 368, 2179- 2187, 2010.

[74] A. Buscarino, L. Fortuna, M. Frasca, Sciuto G. Chua's circuit syncronization with diffusive coupling: new results. International Journal of Bifurcation and Chaos in applied sciences and engineering, ISSN: 0218-1274.

[75] A. Buscarino, L. Fortuna, M. Frasca, Sciuto G. Coupled inductors-based chaotic colpitts oscillator. International Journal of Bifurcation and Chaos.

[76] E.J. Ngamga, A. Buscarino, M. Frasca, G. Sciuto, J. Kurths, L. Fortuna. Recurrences-based detection of the hyperchaos-chaos transition in an electronic circuit, Chaos, vol. 20, no. 4, pp. 043115-1-11, 2010.

[77] A. Bergner, M. Frasca, G. Sciuto, A. Buscarino , E.J. Ngamga, L. Fortuna, J. Kurths. Remote Synchronization in Network Motifs, submitted to PRE April 11, 2011.

[78] A. Buscarino, L. Fortuna, M. Frasca, L.V. Gambuzza, G. Sciuto. Memristive Chaotic Circuits Based On Cellular Nonlinear Networks", International Journal of Bifurcation and Chaos – 2011.

[79] A. Buscarino, L. Fortuna, M. Frasca, Sciuto G. Design of time-delay chaotic electronic circuits IEEE Transactions on circuits and systems - vol. 58, no. 10, October 2011.

[80] A. Buscarino, L. Fortuna, M. Frasca, G. Sciuto, M. T. Rashid. Compensation of transmission channel effects in chaos synchronization Iraq J. Electrical and Electronic Engineering Vol.7 No.1, 2011.

[81] A. Buscarino, L. Fortuna, M. Frasca, Sciuto G. Experimental synchronization of non-identical chaotic circuits. Analysis and Control of Chaotic Systems, Volume # 2 | Part# 1. Location: Queen Mary University of London, United Kingdom, National Organizing Committee Chair: Huijberts, Henri, Just, W.International Program Committee Chair: Huijberts, Henri, Nijmeijer, Hendrik Conference Editor: Huijberts, Henri - June 22nd—24th 2009.

[82] A. Buscarino, L. Fortuna, M. Frasca, Sciuto G. Chaos control of the chaotic colpitts oscillator. 18th IEEE Workshop on Nonlinear Dynamics of Electronic Systems. 26 – 28 May 2010 Dresden, Germany.

[83] G. Di Pasquale, L. Fortuna, M. Frasca, S. Graziani, G. Sciuto and E. Umana. Alternative power supplies for IP2C conditioning circuit. XX Congresso Nazionale della Società Italiana di Biofisica Pura ed Applicata (SIBPA). 11-14 September 2010 – Grosseto.

[84] L. Fortuna, M. Frasca, G. Sciuto, E. Umana And Mofeed Turky. Wireless control of Artemia motion. XX Congresso Nazionale della Società Italiana di Biofisica Pura ed Applicata (SIBPA) 11-14 September 2010 – Grosseto.

[85] L. Fortuna, M. Frasca, G. Sciuto And Mofeed Turky Group motion control. XXX Dynamics days Europe 6-10 September 2010 Bristol - United Kingdom.

[86] A. Buscarino, L. Fortuna, M. Frasca, L. V. Gambuzza, G. Sciuto A New Cellular Nonlinear Network–Based Memristive Chaotic Circuit. International Symposium on Signals Circuits & Systems – Iasi - Romania - 30 June – 1 July 2011 – ISSCS.

[87] A. Buscarino, L. Fortuna, M. Frasca, G. Sciuto, M. T. Rashid. Compensation of transmission channel effects in chaos synchronization.

[88] A. Buscarino, L. Fortuna, M. Frasca, Sciuto G. Experimental synchronization of non-identical chaotic circuits. Chaos 09, London.

[89] Buscarino, A., Fortuna, L., Frasca, M., Sciuto, G.: Harmonic balance method for time-delay chaotic systems design. The 18th World Congress of the International Federation of Automatic Control, IFAC 2011, Milan, Aug. 28 Sept. 2 (2011).

[90] A. Buscarino, L. Fortuna, M. Frasca, Separation and Synchronization of Chaotic Signals by Optimization, Phys. Rev. E, 75, 016215, 2007.

[91] K. Konishi, H. Kokame, Synchronization of pulse-coupled oscillators with a refractory period and frequency distribution for a wireless sensor network, Chaos, 18 (3), 033132, 2008.

[92] R. Albert, A.-L. Barab_asi, Statistical mechanics of complex networks Rev. mod. Phy., 74, 2002.

[93] A. Pikovsky, M. Rosenblum, J. Kurths, Synchronization - A universal concept in nonlinear science, Cambridge University Press, 2001.

[94] L. Fortuna, M. Frasca, M.G. Xibilia, Chua's Circuit Implementations: Yesterday, Today and Tomorrow, World Scienti_c Series on Nonlinear Science, Series A - Vol. 65, 2009.

[95] E. J. Ngamga, A. Buscarino, M. Frasca, L. Fortuna, A. Prasad, J. Kurths, Recurrence analysis of strange nonchaotic dynamics in driven excitable systems, Chaos, 18 (1), 013128-1-8, 2008.

[96] A. Buscarino, L. Fortuna, M. Frasca, Robust synchronization of hyperchaotic circuits, Physica D, 238, 1917-1922, 2009.

[97] M. Rosenblum, A. Pikovsky, J. Kurths, Phase Synchronization of Chaotic Oscillators, Phys. Rev. Lett. E, 76 (11), 1804-1807, 1996.

[98] J. A. Acebr_on, L. L. Bonilla, C. J. Prez Vicente, F. Ritort, R. Spigler, The Kuramoto model: A simple paradigm for synchronization phenomena, Rev. Mod. Phys., 77, 137185, 2005.

[99] D.G. Aronson, G.B. Ermentrout, N. Kopell, Amplitude response of coupled oscillators, Physica D, 41, 403-449, 1990.

[100] T. Pereira, M. S. Baptista, J. Kurths, General framework for phase synchronization through localized sets, Phys. Rev. E 75, 026216, 2007.

[101] I. I. Mokhov, D. A. Smirnov, P. I. Nakonechny, S. S. Kozlenko, E. P. Seleznev, J. Kurths, Alternating mutual influence of El-Ninno/Southern Oscillation and Indian monsoon , Geophys. Res. Lett., 38, L00F04, 2011.

[102] E. N. Lorenz, Deterministic Nonperiodic Flow, Journal of the Atmospheric Sciences 20(2), 1963, pp. 130–141.

[103] R. N. Madan, Chua's Circuit: A Paradigm for Chaos, World Scientific Series on Nonlinear Sciences, Series B, vol. 1, 1993.

[104] L. Fortuna, M. Frasca, M.G. Xibilia, Chua's Circuit Implementations: Yesterday, Today, Tomorrow, World Scientific, 2009.

[105] O. E. Rössler, An equation for continuous chaos, Physics Letters A, 57 (5), 1976, pp. 397–398.

[106] Hindmarsh J. L., and Rose R. M. (1984) A model of neuronal bursting using three coupled first order differential equations. Proc. R. Soc. London, Ser. B 221:87–102.

[107] Chua, L. O. [1971] “Memristor-The missing circuit element,” IEEE Trans. Circuit Theory 18, pp. 507–519.

[108] Kennedy, M. P. [1994] Chaos in the Colpitts Oscillator," IEEE Trans. Circuits Syst. I Fundam. Theory Appl. 41, pp. 771{774.